SYNTHESIS OF IRON AND NICKEL BASED METAL OXIDE NANOPARTICLES AND INVESTIGATION OF THEIR POTENTIAL USE AS CATALYSTS IN WATER OXIDATION REACTION

A THESIS SUBMITTED TO
THE GRADUATE SCHOOL OF NATURAL AND APPLIED SCIENCES
OF
MIDDLE EAST TECHNICAL UNIVERSITY

BY

BÜŞRA ATAK

IN PARTIAL FULFILLMENT OF THE REQUIREMENTS
FOR
THE DEGREE OF MASTER OF SCIENCE
IN
CHEMISTRY

DECEMBER 2023

Approval of the thesis:

SYNTHESIS OF IRON AND NICKEL BASED METAL OXIDE NANOPARTICLES AND INVESTIGATION OF THEIR POTENTIAL USE AS CATALYSTS IN WATER OXIDATION REACTION

submitted by **BÜŞRA ATAK** in partial fulfillment of the requirements for the degree of **Master of Science** in **Chemistry, Middle East Technical University** by,

Prof. Dr. Halil Kalıpçılar
Dean, **Graduate School of Natural and Applied Sciences** ________________

Prof. Dr. Özdemir Doğan
Head of the Department, **Chemistry** ________________

Prof. Dr. Emren Nalbant
Supervisor, **Chemistry, METU** ________________

Examining Committee Members:

Prof. Dr. Ayşen Yılmaz
Chemistry, METU ________________

Prof. Dr. Emren Nalbant
Chemistry, METU ________________

Prof. Dr. Ali Çırpan
Chemistry, METU ________________

Prof. Dr. İrem Erel Göktepe
Chemistry, METU ________________

Assoc. Prof. Dr. Oktay Demircan
Chemistry, Boğaziçi University ________________

Date: 06.12.2023

I hereby declare that all information in this document has been obtained and presented in accordance with academic rules and ethical conduct. I also declare that, as required by these rules and conduct, I have fully cited and referenced all material and results that are not original to this work.

Name Last name : Büşra Atak

Signature :

ABSTRACT

SYNTHESIS OF IRON AND NICKEL BASED METAL OXIDE NANOPARTICLES AND INVESTIGATION OF THEIR POTENTIAL USE AS CATALYSTS IN WATER OXIDATION REACTION

Atak, Büşra
Master of Science, Chemistry
Supervisor: Prof. Dr. Emren Nalbant

December 2023, 85 pages

The urge to find energy sources alternative to fossil fuel made hydrogen a centre of interest. Splitting water is very promising and environmentally friendly way of obtaining hydrogen, yet the process embodies some difficulties. Half-reactions involved in this process, particularly the anode reaction (oxygen evolution reaction (OER)), proceed slowly and require high energy. These difficulties can be overcome with the use of proper catalyst. The most effective catalysts for OER are Ru and Ir - based. However, their low abundancy and high cost are the main drawbacks for their practical use. Metal oxide nanoparticles of abundant transition metals are considered as promising alternative catalysts. Therefore, our study aim is to synthesize ZnO-$NiFe_2O_4$ hybrid nanomaterials that have potential use as catalyst in photochemical water splitting. As ZnO component play a key role in enhancing photocatalytic activity of the hybrid material, $NiFe_2O_4$ component function as driving force for the electrochemical process.

Hydrothermal, solvothermal and sol-gel methods were used for the synthesis of $NiFe_2O_4$, ZnO and ZnO-$NiFe_2O_4$ hybrid material. Then, a variety of analytical methods, such as SEM, EDX, ICP-OES, XPS, BET, and XRD were used to characterize the synthesized nanomaterials.

The electrochemical behaviour of the hybrid material in OER was examined. The results showed that ZnO-$NiFe_2O_4$ hybrid nanomaterial with an onset potential of 1.63 V vs RHE and overpotential of 450 mV at 10 mA cm^{-2} has encouraging catalytic activity in OER. Overall water oxidation activity of the synthesized material was found to be comparable to the one of RuO_2.

Keywords: Metal oxides nanoparticles, Nickel, Ferrite, Water oxidation, Electrocatalysis

ÖZ

DEMİR VE NİKEL ESASLI METAL OKSİT NANOPARÇACIKLARIN SENTEZİ VE SU OKSİDASYON REAKSİYONUNDA KATALİZÖR OLARAK KULLANIM POTANSİYELİNİN ARAŞTIRILMASI

Atak, Büşra
Yüksek Lisans, Kimya
Tez Yöneticisi: Prof. Dr. Emren Nalbant

Aralık 2023, 85 sayfa

Fosil yakıtlarına alternatif enerji kaynakları bulma isteği, hidrojeni ilgi odağı haline getirmiştir. Suyun ayrıştırılması, hidrojen elde etmenin çok umut verici ve çevre dostu bir yoludur, ancak süreç bazı zorlukları da bünyesinde barındırmaktadır. Bu süreçte yer alan yarı reaksiyonlar, özellikle anot reaksiyonu (oksijen oluşum reaksiyonu (OER)) yavaş ilerlemekte ve yüksek enerji gerektirmektedir. Uygun katalizör kullanımıyla bu zorlukların üstesinden gelinebilir. OER için en etkili katalizörler Ru ve Ir temelli olanlardır. Ancak bunların nadir elementler ve yüksek maliyetli olmaları, onların pratik kullanım açısından en önemli dezavantajlarıdır. Doğada bol bulunan geçiş metallerinden elde edilen nanomalzemeler umut verici alternatif katalizörler olarak kabul edilmektedir. Bu nedenle çalışmamız, fotokimyasal su ayrıştırmasında katalizör olarak kullanım potansiyeli olan ZnO-$NiFe_2O_4$ hibrit malzemesinin sentezlenmesini amaçlamaktadır. ZnO bileşeni hibrit malzemenin fotokatalitik aktivitesinin arttırılmasında önemli bir rol oynarken, $NiFe_2O_4$ bileşeni elektrokimyasal süreç için itici güç olarak işlev görmektedir. $NiFe_2O_4$, ZnO ve ZnO-$NiFe_2O_4$ hibrit malzemenin sentezinde hidrotermal, solvotermal ve sol-jel yöntemleri kullanılmıştır. Daha sonra sentezlenen nanomalzemeleri karakterize etmek için SEM, EDX, ICP-OES, XPS, BET ve XRD gibi çeşitli analitik yöntemler kullanılmıştır.

Hibrit malzemenin OER' daki elektrokimyasal davranışı incelenmiştir. Sonuçlar, 1,63 V (RHE'ye karşı) başlangıç potansiyeline ve 450 mV (10 $mAcm^{-2}$' de) aşırı potansiyeline sahip ZnO-$NiFe_2O_4$ hibrid malzemenin OER' de katalitik aktiviteyi arttırdığını göstermiştir.Sentezlenen malzemenin su oksidasyon aktivitesinin RuO_2' inki ile kıyaslanabilir ölçüde olduğu bulunmuştur.

Anahtar Kelimeler: Metal oksit nanopartikülleri, Nikel, Ferrit, Su oksidasyonu, Elektrokataliz

To my beloved family,

ACKNOWLEDGMENTS

Firstly, I want to express my gratitude to Prof.Dr. Emren Nalbant for allowing me to join her research group and for her supportive, encouraging, patient, and educational advice during my graduate studies.

I would also like to thank Asude Çetin and Serra Karaman, who gave me useful information, and advice and sharing with me their studies.

I want to express my gratitude to every member of the NanoClusMate Research Group for their friendship and excellent attitude through my experimental studies.

I am grateful to Prof. Dr. Ayşen Yılmaz for giving me permission to use the XRD instrument. I express my gratitude to İpek Yıldırım and her team for their assistance and instruction in taking measurements.

I am grateful to the Central Laboratory at METU for their assistance in carrying out the characterization of my studies.

Finally, but no less, my deepest gratitude is extended to my parents and my sister. I sincerely appreciate their love, concern, and unwavering encouragement as I pursue my goals. But above all, I am grateful for their belief in me.

TABLE OF CONTENTS

LIST OF TABLES

TABLES

LIST OF FIGURES

FIGURES

LIST OF ABBREVIATIONS

TMO	Transition Metal Oxide
ccp	cubic close packing
CTAB	Cetyltrimethylammonium bromide
NTA	Nitrilotriacetic acid
XRD	X - Ray Diffraction
FWHM	Full width half maximum
SEM	Scanning Electron Microscopy
EDX	Energy Dispersive X-Ray
ECSA	Electrochemically Active Surface Area
XPS	X - Ray Photoelectron Spectroscopy
ICP-OES	Inductively Coupled Plasma - Optical Emission Spectroscopy
BET	Brunauer – Emmett – Teller
HER	Hydrogen evolution reaction
OER	Oxygen evolution reaction
LSV	Linear Sweep Voltammetry
CV	Cyclic Voltammetry
RF	Roughness Factor
ECSA	Electrochemically Active Surface Area
DMF	Dimethylformamide
GCE	Glassy carbon electrode
RHE	Reversible hydrogen electrode

CE	Counter electrode
WE	Working electrode
RE	Reference Electrode

CHAPTER 1

INTRODUCTION

Conventional fossil fuels have been extensively consumed due to the world's increasing energy needs, resulting in significant environmental harm and the depletion of non-renewable energy sources. Producing and utilizing profitable and safe energy is a key to address the current energy crisis. Hydrogen, with its high-energy content and eco-friendly nature, has emerged as a significant alternative to fossil fuels.[1] Obtaining hydrogen from water is a feasible option as water is a renewable and reliable source of energy.[2]

The use of electrochemical water splitting, particularly to generate hydrogen, has drawn increasing interest. The half-reactions of oxygen evolution and hydrogen evolution both contribute to the total reaction. The bottleneck of overall water splitting is thought to be the water oxidation step that occurs at the anode. This is due to bond breaking and the transfer of multiple electrons and protons during the reaction, which creates a large energy barrier. As a result, an overpotential is required to overcome this barrier.[3] Reducing the overpotential results in lower energy requirements. Therefore, it is important to decrease overpotential and increase reaction rates. The best solution to achieve this is to use catalysts that are stable and can be reused. Since hydrogen production is vital for energy, it is crucial to design and improve new catalyst systems. Studies have shown that metal-oxide nanoparticles are one of the most effective electrocatalysts for water oxidation.[3]

Noble metals such as Pt, Ru, and Ir, as well as their compounds, have presented strong catalytic activity.[4] Ruthenium oxide (RuO_2) and iridium oxide (IrO_2) are two of the most efficient electrocatalyst. Liu et al. reached highly effective results for RuO_2, 190 mV overpotential at 10 mA cm^{-2} current density (η_{10}) with 1.34 V (vs RHE) onset potential.[5] In addition, Devades et al. obtained onset potential for RuO_2

1.42 V (vs RHE).[6] In this study, the activity of RuO_2 nanoparticles was determined to be 1.49 V (vs RHE) onset potential and 365 mV overpotential at η10. At present, noble metals such as Pt, Ru, Ir, and their derivatives have significant catalytic activity; nevertheless, their high cost and scarcity severely limit their practical use in large-scale production.[4] As a result, finding low-cost, robust, and effective catalysts is critical and has been identified as an important issue.[5] Metal oxides nanoparticles are a popular choice for water oxidation electrocatalysis.

Because of their high activity as electrocatalysts, bimetallic nanoparticles have been gaining significant interest.[7] Perovskite and spinel, two types of metal materials, have received a lot of interest due to their complex chemistry resulting from the contributions of each metal in its structures, as well as their excellent stability and activity in alkaline media.[8–10]

Because of their low cost, high stability, high catalytic activity and environmental friendliness, mixed valence transition metal oxides with a spinel structure (AB_2O_4, A and B: transition metal, O: oxygen) were discovered as potential catalysts.[11] Especially, NiFe-based oxides have been identified as efficient catalyst materials.[12] Yuan et al. investigated and analysed the activity of tubular ferrite combinations of these elements in spinel form (MFe_2O_4, M: Fe, Ni, Co) for water oxidation. Overpotentials at 10 mA cm^{-2} current density (η_{10}) were used to compare the materials, and the results were 340, 392, and 432 mV for $NiFe_2O_4$, $CoFe_2O_4$ and Fe_3O_4 respectively, with $NiFe_2O_4$ being the most efficient combination for this research.[13] Furthermore, Liu et al. evaluated the oxygen evolution reaction electrocatalytic activity of $NiFe_2O_4$ nanorods and found an overpotential of 342 mV at a current density of 10 mA cm^{-2}.[14]

Typical soft ferromagnetic substance $NiFe_2O_4$ crystallizes in an entirely inverse spinel structure, with iron ions occupying tetrahedral and octahedral positions and all nickel ions in the octahedral sites.[15] It also shows that by lowering the particle size, $NiFe_2O_4$ spinel's carriers' concentration and electron conductivity both improved. According to these theories, it is worthwhile and trustworthy to create Ferich $NiFe_2O_4$ catalysts with unique nanostructures and improved electron conductivity for effective water oxidation.[16]

Because of their strong catalytic properties, large adsorption capacity, photo-chemical stability, and modest saturation magnetization, $NiFe_2O_4$ nanoparticles are among the most promising candidates for water oxidation reaction.[17]

Because of their ideal electrical structure, light absorption capabilities, and excited-state lifetimes, semiconductors are very effective as photocatalysts. Zinc oxide (ZnO) with a wide band gap (E_g = 3.37 eV) is a widely recognised superior photocatalyst among the many semiconductors used.[18] ZnO photocatalysts are often not suited because of their wide bandgap and fast recombination of photo-generated carriers, which lead to low quantum efficiency, significant photocorrosion.[17] Numerous attempts have been made to enhance ZnO's performance such as coupling with metals or metal oxides. Combination of ZnO with $NiFe_2O_4$ results in semiconductor photocatalysts with increased activity in visible light. Theoretically, ferrite materials connected to ZnO will generate a heterojunction and the photogenerated electrons and holes would be efficiently divided and increasing the photocatalytic activity.[18]

Based on this knowledge, the goal of this thesis is to create nickel ferrite nanoscale bimetallic oxide catalyst systems and hybrid structure with ZnO to investigate their potential use in water splitting reaction. Hydrothermal and sol-gel method were used to produce nanoparticles. Following characterization, nanoparticles were produced in a suitable form for coating on glassy carbon electrodes (GCE) to evaluate their electrocatalytic activity toward OER. Additionally, it was found that the catalysts' activity was comparable to those of catalysts for water oxidation with similar structures.

The next following sections give a brief overview of the synthesis, characterization, and application of transition metal oxides (TMOs) as a catalyst before discussing details of this thesis study.

1.1 Transition Metal Oxide

Transition metal oxides, particularly bimetallic ones, are considered as very intriguing material groups mostly due to their stability and ease of synthesis.[19,20] The major distinction between transition metal oxide (TMO) and other metals is that their valence electrons can be found in more than one shell. The capacity of transition metals to have different oxidation states results in a large variety of compounds with adjustable properties for specific applications such as thermal, electrical, magnetic, and optical qualities. The partly filled d-orbitals of the metal and the interactions between electrons in these orbitals cause variation in transition metal oxides (TMOs).[21]

TMOs are generated via charge exchange between highly electronegative oxygen atoms and less electronegative transition metal atoms. TMOs may be classified into several types based on oxidation states. Monoxides (such as ZnO), dioxides (such as RuO_2), trioxides (such as WO_3), and highly complex oxides (such as $NiFe_2O_4$) may all be created with distinct bonding and crystal structures.

Depending on their structures, TMO crystals take variety of names, including rock-salt, rutile, perovskite, spinels, etc.[22] Large oxide ions stacked in close-packed, cubic, or hexagonal arrays are a common feature of all these formations. It leads to the creation of tetrahedral and octahedral networks.

1.1.1 Monoxides

Except for chromium and scandium, all the first-row transition metals combine to create monoxides. Most of them crystallize in a rock salt structure where the transition metal ions fill every octahedral hole, and the oxide ions form a cubic close packing (ccp) array. Monoxides can form a wurtzite structure when there are deviations because of nonstoichiometry, rearranged atoms, or atom deficiency. Some of these monoxides take on a wurtzite structure, like ZnO.

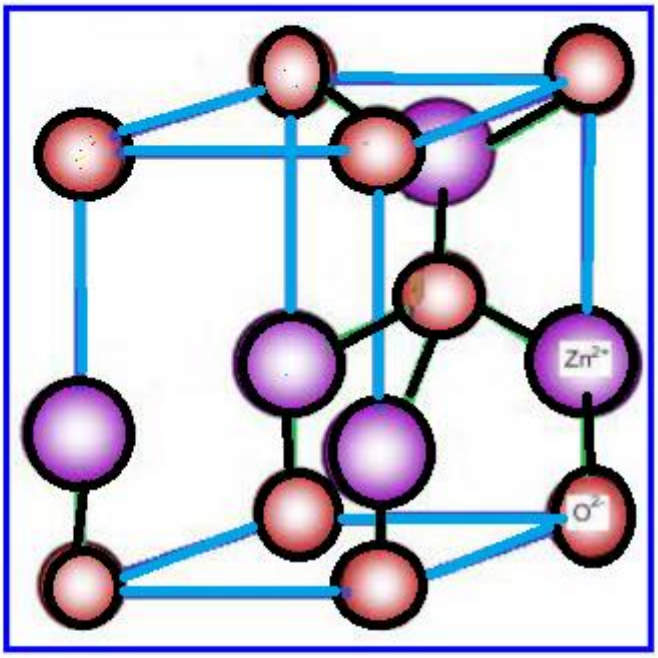

Figure 1. 1. Wurtzite crystal structure of ZnO. (modified from[23])

1.1.2 Spinels

The chemical structure of spinels is typically AB_2O_4, where A and B are metal ions (A, B = Zn, Ni, Fe, etc.).[23] In AB_2O_4, cations A and B were charged as 2^+ and 3^+, respectively, at tetrahedral and octahedral sites. One-eighth of the tetrahedral sites and one half of the octahedral sites in the spinel structure are filled by cations. The oxide ions are arranged in a cubic close-packed array. According to how cations occupy each octahedron or tetrahedron, spinel can be referred to as having an inverse spinel structure or a typical spinel structure. In a typical spinel structure, the cations A^{2+} and B^{3+} occupy tetrahedral and octahedral positions, respectively. Half of the B^{3+} ions shift to tetrahedral positions in the case of the inverse spinel structure.

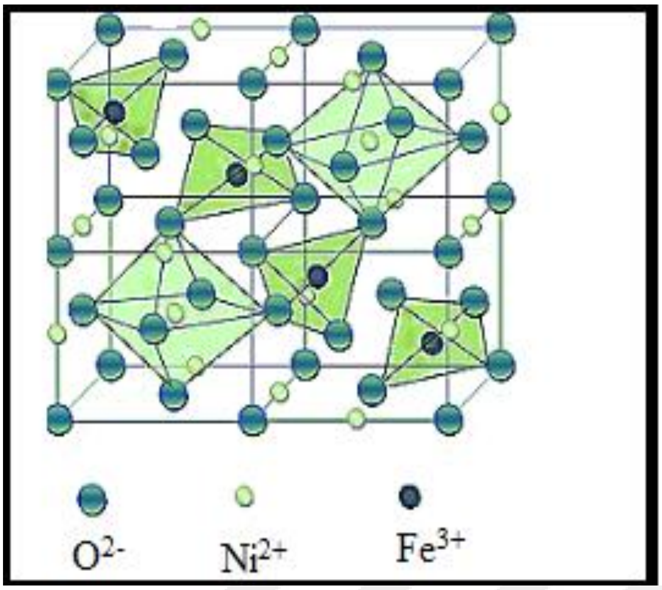

Figure 1. 2. Spinel structure of $NiFe_2O_4$. (prepared based on a figure in reference 24[24])

1.2 Preparation of Metal Oxide Nanoparticles

Due to their unique qualities and applications in a wide range of fields, nanomaterials have attracted increased attention in recent years. Researchers are investigating new chemical methods for producing these materials because of the fascinating features of nanomaterials, which may be modified to suit specific purposes.

There are two major ways to create nanomaterials: the top-down physical method and the bottom-up physical and chemical method. A subtractive process known as the "top-down approach" divides a bulk starting material into smaller, nanoscale components. The procedures are not appropriate for large-scale production and are quite costly. The approach is appropriate for use in lab research. The method relies on material grinding. Lithography and similar processes are examples of the top-down approach.

An additive process known as the "bottom-up approach" begins with precursor atoms or molecules, which then combine to build nanoscale structures. Atom by atom or molecule by molecule, nanostructures are constructed using a bottom-up method. Furthermore, this approach encompasses a broad range of techniques, including chemical vapour deposition, spray pyrolysis, coprecipitation, sol-gel, hydrothermal/solvothermal and flux growth.[25]

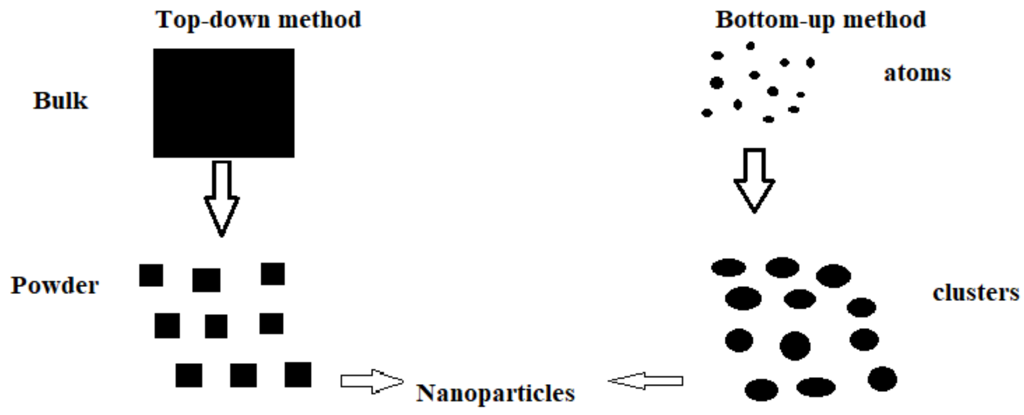

Figure 1. 3. Diagram illustrating the top-down and bottom-up methods to produce nanoparticles.

Solution-phase synthesis methods can provide control the reaction pathway and facilitate various nanomaterial crystal structures, maintain size uniformity, produce homogeneous compositions and distinct morphologies. Because of these reasons, it is mostly chosen over solid and gas-phase approaches.[26] In the solution-phase synthesis of TMO nanoparticles, two widely utilized techniques are called sol-gel and hydrothermal/solvothermal.

1.2.1 Sol-Gel Method

One of the most effective processes for creating metal oxide nanomaterials is sol-gel synthesis. Simple inorganic polymerization of metal precursors results in the production of inorganic solids.[9] The five steps of the sol-gel method are typically as follows:

***Creation of sol*:** Precursors and an appropriate reagent are dissolved in a solvent to form the sol. The most common precursors are metal alkoxides or salts. Typically, ethylene glycol, propionic acid, and citric acid are included as chelating agents. Following dissolution, hydrolysis of the precursors produces hydroxides and/or monomers, which are then condensed to produce oligomers.

Forming a gel: This stage produces gel, an inorganic linked polymeric substance, by causing further oligomer/monomer condensation. Hydrogen bonding between the solvent and the gel has resulted in the formation of a porous structure of oxide material.

Gel solidification by heating (aging): The gel continues to condense and solidify in this step. The produced gel can be heated to accelerate the rate of ageing.

Drying: There are two ways to carry out the drying process: thermal evaporation produces xerogel with a lower pore size than aerogel, or supercritical drying produces aerogel with a large porosity in the structure.

Dehydration (calcination): In the final step, organic moieties, and any -OH groups on the surface are eliminated by heat treatment at high temperatures.[27]

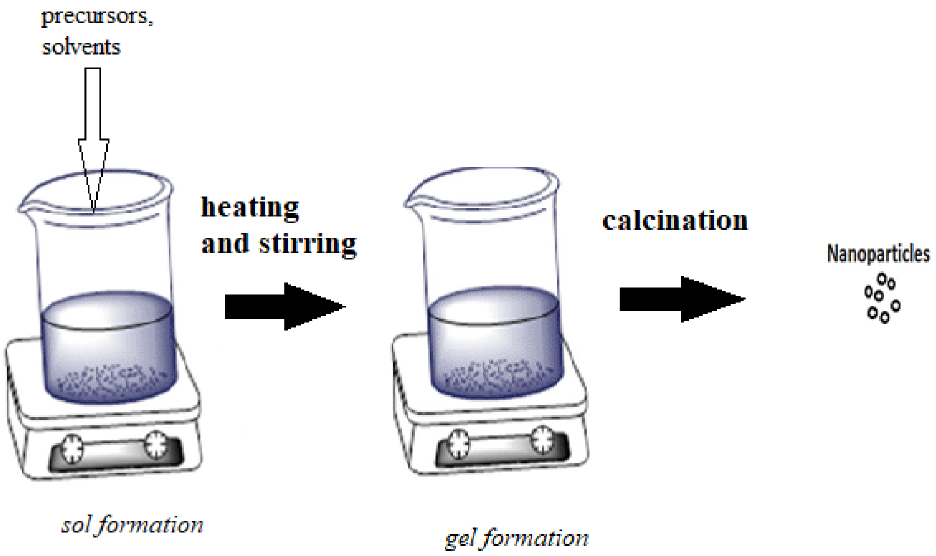

Figure 1. 4. Schematic illustration of the sol-gel process for nanoparticles synthesis

1.2.2 Hydrothermal/Solvothermal Method

The hydrothermal approach is a high-pressure, water-based solution-phase synthesis method. Solvothermal synthesis is a process that uses solvents other than water, such as ethanol, 2-propanol, or ethylene glycol.[9] The reaction vessels in this approach are autoclaves, which endure high pressure and temperature. It is simple to produce nanomaterials with controlled size and composition by altering the reaction temperature and/or solvent employed. Furthermore, homogeneously dispersed nanomaterials with wide range of morphologies can be produced by using several types of surfactants, such as cetyltrimethylammonium bromide (CTAB), cetyl alcohol, urea, or nitrilotriacetic acid (NTA).[9]

These are the most widely used processes for creating TMO nanomaterials with a various morphology. The idea behind how the autoclave working principle is the formation of two distinct temperature zone as the mixture heats up. The hotter area, which is in the vessel's lower section, dissolves the precursors. The cooler part of the solution sinks down as the solution then rises to the top section. Crystals develop when the solution gets supersaturated and the upper part's temperature drops.[28]

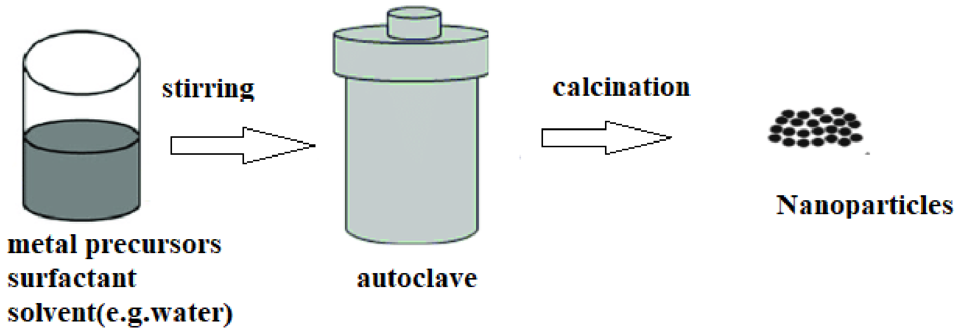

Figure 1. 5. Illustration of hydrothermal method to synthesize nanomaterials

1.3 Characterization of the Nanomaterials

Analytical methods are mostly used to characterize the as-synthesized nanoparticles to determine whether they have the desired properties. Analysing the composition, structure, and morphology of the nanomaterials is necessary to obtain important insights into how they behave in certain applications.

A common method for determining the size, shape, morphology, and surface topography of nanoparticles is electron microscopy. Although surface topography analysis can be achieved with Scanning electron microscopy (SEM), it lacks the resolution necessary to offer information at the atomic scale. To analyse the sample's primary elements, energy dispersive X-ray spectroscopy (EDX) can be used in combination with SEM.

To learn more about the crystal structure and chemical composition of the nanoparticles, X-Ray diffraction (XRD) technique is also used. Furthermore, the material can be identified using the typical set of lattice spacings derived from the

X-ray pattern. Furthermore, by using the Debye-Scherrer equation (1.1.), XRD can be used to predict crystallite size.[29]

$$\tau = K\lambda / \beta\cos\theta \tag{1.1}$$

where τ is the crystallite size in nanometers, K is the shape factor that is equal to 0.9, λ is the X-ray radiation wavelength, β is the line broadening (radian) at full width half maximum (FWHM) and θ is the Bragg angle.

The surface characteristics of the nanoparticles are examined using X-Ray photoelectron spectroscopy (XPS). The distinct energy levels that photoelectrons emanate from the surface show the chemical and electronic states of the constituent components, as well as their concentration and distribution throughout the material. As a result, XPS is an extremely helpful technique for assessing the surface structure of nanoparticles in both qualitative and quantitative ways.[30]

Using adsorption-desorption techniques like the Brunauer-Emmett-Teller (BET) isotherm, one may determine the surface area, pore volume, size, and porosity of the material characteristics.

It is possible to determine the atomic composition of a given material using an analytical method called inductively coupled plasma-optical emission spectroscopy (ICP-OES). To accurately identify the kind and relative abundance of each element within the complexity of a compound, the method utilizes the distinct photophysical signals of each element.[31]

1.4 Water Splitting

As energy consumption and environmental harm increase, fossil fuels are being exhausted and being replaced by hydrogen that is a renewable energy source with a high energy density. Due to the significant energy contained in its bonds, hydrogen has drawn increasing interest as a source of energy. In addition, it is likely to be obtained using easily available and renewable energy sources such as water. The process of hydrogen and oxygen formation known as water splitting, from which protons and electrons are extracted, can be summed up by the following reactions:[32]

Oxidation half reaction: $2H_2O \longrightarrow O_2 + 4H^+ + 4e^-$ (1.2)

Reduction half reaction: $2H^+ + 2e^- \longrightarrow H_2$ (1.3)

Overall water splitting: $2H_2O \longrightarrow O_2 + 2H_2$ (1.4)

Water splitting, especially water oxidation, is a difficult process (non-spontaneous, $\Delta G°= 475$ kJ/mol) that requires a lot of energy to take place. This problem can be addressed by using the proper catalyst. Target locations for effective oxygen adsorption and desorption may be found in transition metal oxides with spinel structures. Additionally, out of all the many types of spinel catalysts, Ni and Fe-based catalysts have attracted the great deal of attention for electrocatalytic water splitting. Research has eventually focused on the production of novel, stable, and active catalysts.[33]

Three techniques are available for studying water oxidation: photoelectrochemical photochemical and electrochemical oxidation. The sections that follow provide an explanation of these strategies' details.

1.4.1 Photoelectrochemical Water Oxidation

In this process, light activates catalysts, which later oxidize water. Pt/TiO_2 is an example of a metal-semiconductor hybrid that may be employed as a catalyst where one metal acts as a co-catalyst and the other as a photocatalyst.[34] When light is exposed, electrons migrate from the photocatalyst's valence band to its conduction band, forming an electron-hole pair. As protons are reduced by electrons transported to the co-catalyst, the adsorbed water in the positively charged holes is oxidized.

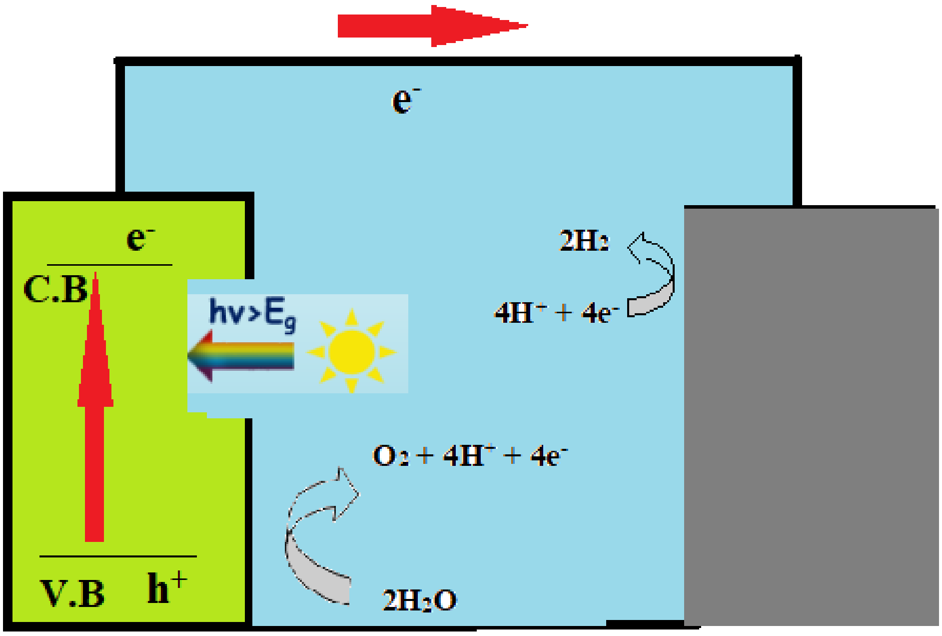

Figure 1. 6. Diagram showing the process of photoelectrochemical water oxidation

1.4.2 Photochemical Water Oxidation

Due to its ability to transform light energy into chemical energy, photochemical water splitting is a very similar process to natural photosynthesis. In this case, without an electric circuit, electron (e^-) and positive-hole (h^+) pairs are produced when a photocatalyst absorbs sunlight with energy equal to or greater than its bandgap. Moreover, the photocatalyst's valence band is left with holes when these electrons become excited to go into the conduction band. The pair of e^+ and h^+ are successively transferred to the photocatalyst surface for corresponding chemical processes of reduction and oxidation, respectively. In here semiconductor is known as photocatalyst. To promote the oxidation of water, the valence band edge potential needs to be greater than the water's oxidation potential, which is 1.23 V against NHE. These numbers indicate that the water-splitting reaction needs to be driven by a theoretical semiconductor band-gap energy of 1.23 eV.[35]

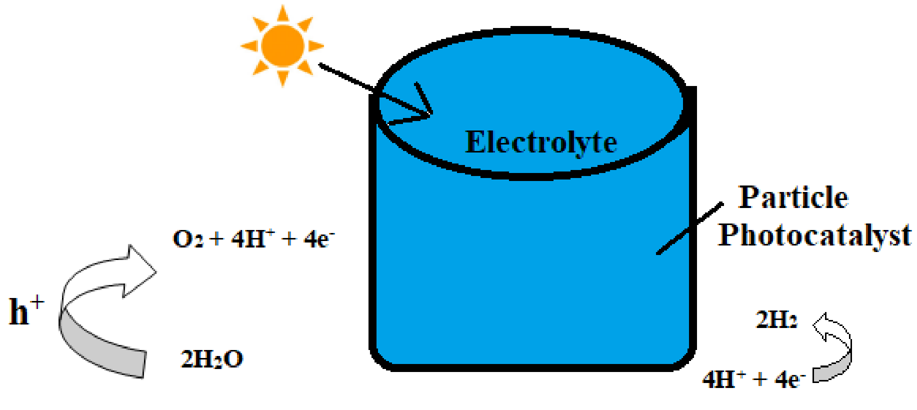

Figure 1. 7. Diagram showing the process of photochemical water oxidation

1.4.3 Electrochemical Water Oxidation

Usually, electrochemical water splitting is carried out in an electrolysis cell that has electrodes, an ionic conductor called the electrolyte, and an electronic conductor. This method uses the hydrogen evaluation reaction (HER) and the oxygen evolution reaction (OER) to divide water into hydrogen and oxygen at the cathode and anode compartments, respectively, in response to an external voltage provided. Catalysts are employed as the anode materials in this process. The applied potential causes catalysts to oxidize. Water molecules then oxidize because of the activated catalyst. The system under study has similarities to solar fuel generating cell settings, which is the main benefit of electrochemical oxidation. As a result, stable catalysts that have been shown to be effective through electrochemical oxidation are seen as crucial models for those that will be created for solar fuel production systems. Although in theory this water splitting process should be simple, it is challenging to perform due to non-spontaneity and a high energy need brought on by the cleavage of four O-H bonds and the production of O-O bond. The energy barrier must be broken down to speed up the process and maintain these effects. For the reaction to supply its net energy after the use of catalysts, there needs to be a significant overpotential. Thus, an effective catalyst needs to meet two essential requirements: low overpotential and good stability.[36]

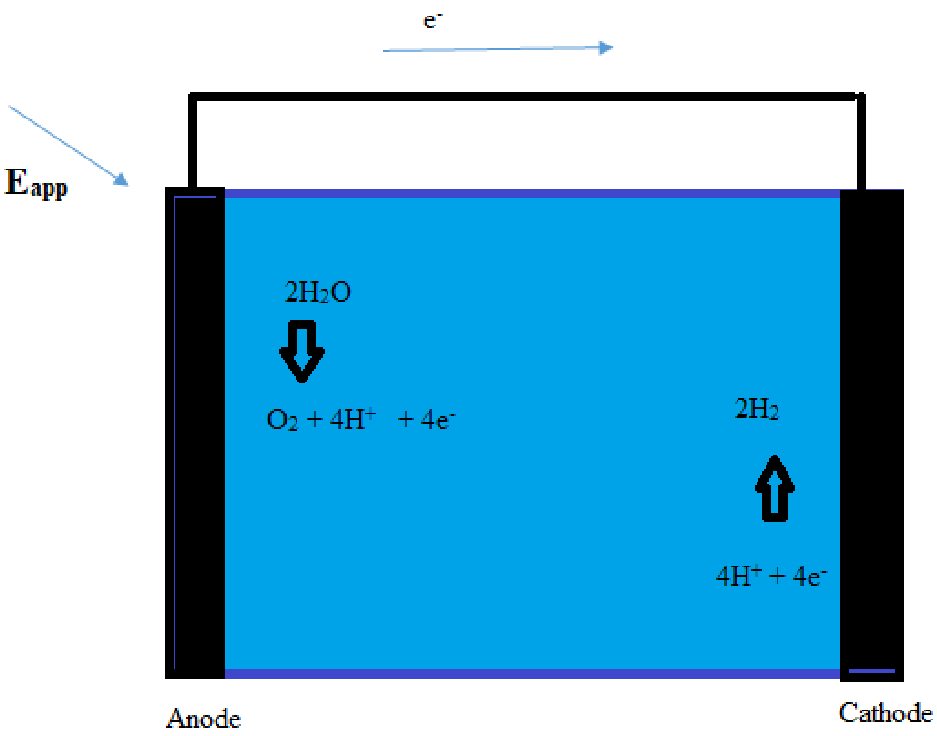

Figure 1. 8. Diagram showing the process of electrochemical water oxidation

Analysing electron transport is made possible by electrochemistry. Two-electrode or three-electrode systems can be used for it. Three-electrode electrochemical cells are commonly chosen. For electrochemical measurements, an alkaline electrolyte solution is used to hold the counter, reference, and working electrodes, which are then coupled to a potentiostat.

The most crucial factors considered while designing water oxidation catalysts are overpotential, stability, Tafel slope, onset potential, and capacitance. A variety of electrochemical methods, including controlled potential coulometry, cyclic voltammetry (CV), linear sweep voltammetry (LSV), and chronoamperometry, can be used to get these qualities.

By recording linear sweep voltammograms of an electrode that has been modified with catalyst, polarization curves can be generated. Three significant details regarding the activity of catalysts are shown by these curves. The onset potential is the first one. The term "onset potential" often refers to the potential at a current density of 10 μA cm^{-2} and marks the beginning of water oxidation. Drawing two tangent lines, one at the faradaic area where an increase in current density is noticed and the other at the non-faradaic region, can also be used to determine it. Onset potential is produced by the place where these two tangent lines connect.[37]

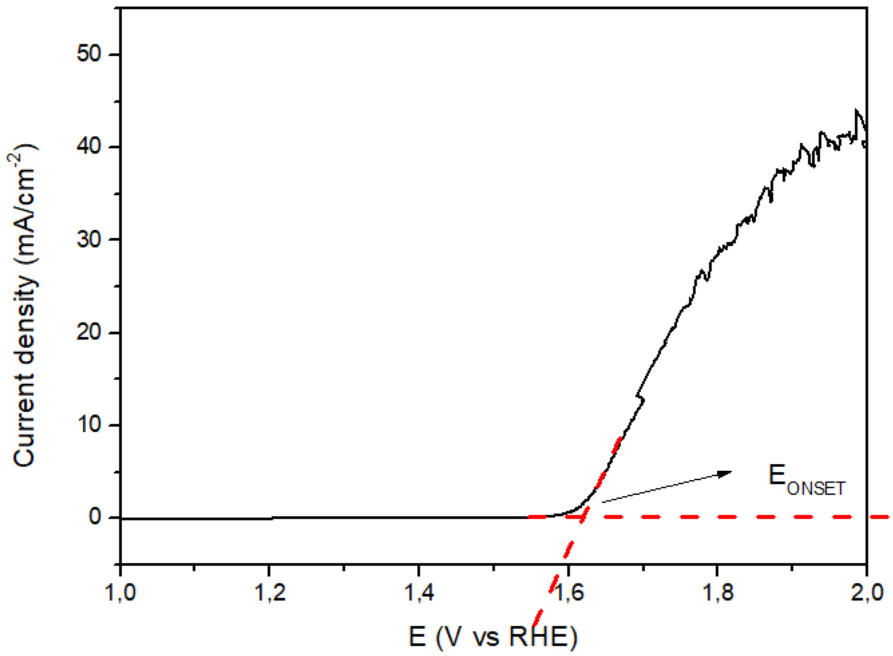

Figure 1. 9. Finding the onset potential using a polarization curve

Additionally, polarization curves can also be used to calculate overpotential values. For a reaction to take place, the applied potential must ideally match the reaction's equilibrium potential. To overcome the reaction's kinetic barrier, a greater potential than the equilibrium potential is used.[38] Overpotential is the term used to describe the difference between the applied potential and equilibrium potential. It is described by the following equation (1.5), where E is the applied potential and E_{eq} is the potential of equilibrium.

$$\eta = E - E_{eq} \tag{1.5}$$

Another characteristic that can be determined by polarization curves is the Tafel slope. The linear part of polarization curves can be fitted to the Tafel equation (1.6) to determine the Tafel slope where η is the overpotential, a is the intercept giving exchange current density j and b is Tafel slope.

$$\eta = a + b.\log(j) \tag{1.6}$$

Tafel slope provides details on the overall reaction's mechanism and rate-determining phase. The reaction rate increases with decreasing Tafel slope.

When a double layer forms between the electrolyte and catalyst film, catalysts on the electrode surface can function as capacitors by storing charge. An indicator of the quantity of atoms that can function as a catalyst is double-layer capacitance (C_{dl}), which is directly proportional to the modified electrode's active surface area. By recording CV at different scan rates (v) and in a non-faradaic potential window, it is possible to determine the value of C_{dl}. Equation (1.7) suggests that the measured current is most likely the result of double-layer charging current (i_{dl}).

$$C_{dl} = i_{dl} / v \tag{1.7}$$

Plotting i_{dl} against v produces a straight line whose slope indicates the catalysts' C_{dl} values. Since the active surface area of the catalyst is correlated with the double layer capacitance, many these values suggest a high number of active sites and, thus, appropriate catalytic activity. Equations (1.8) and (1.9), respectively, can be used to calculate the catalysts' electrochemically active surface area (ECSA) and roughness factor (RF), which are crucial parameters in the evaluation of catalytic activity. The term "RF" describes a measurement of an electrode's surface imperfections that is used as a catalyst in an electrochemical reaction.

$$ECSA = C_{dl} / Cs \tag{1.8}$$

where Cs is the specific capacitance of the material.

$$RF = ECSA / GSA \tag{1.9}$$

where the electrode's geometric surface area is represented by GSA.

Greater numbers of active sites indicate better catalytic performance, as seen by higher C_{dl}, ECSA, and RF values.

By providing an electrode with a steady voltage for an extended amount of time, the stability of an electrocatalyst can be evaluated. Over the course of the long-term electrolysis, the change in current density with time can be seen. Another method is to compare the onset potential, overpotential, or current densities by recording polarization curves before and after electrolysis. A small or absent variation in these parameters indicates a high level of electrocatalyst stability.

1.5 Motivation of Thesis

Research focuses on the world's enormous energy need and how to supply it via sustainable, green, and renewable sources. Hydrogen is receiving well-deserved attention since it is very promising energy storage material. Hydrogen can be obtained from water by splitting water. However, the process requires a lot of energy and is not spontaneous; therefore, it is challenging to study from both a kinetic and thermodynamic perspective. The best and simplest method to solve these issues is to use proper catalysts. Therefore, developing new, stable, and active catalyst systems for the water oxidation reaction has become very active research field.

Ru, Ir, and their oxides are the most efficient catalysts with the lowest overpotentials for splitting water. These metals are, nevertheless, extremely costly, scarce, and valuable. For this reason, producing a catalyst system that has low price and low overpotential is the focus of the many researchers all over the world. Because they can be used more economically and effectively for water splitting, earth-abundant metal oxides are preferred.

Earth-abundant metal oxides can be obtained in variety of morphologies such as spheres, rods, lines, and wires. Particularly, because of their huge surface area, materials in the nano domain are receiving a lot of attention as possible catalysts. TMOs can be synthesized in different structures (i.e. spinel, perovskite) allowing them to present in various coordination settings and oxidation states. This opens the prospect of preparing metal oxides in different combinations with improved stability and activity for catalytic applications.

In general, the process of water splitting using solar energy to produce H_2 and O_2 over a semiconductor photocatalyst is a promising way for the large-scale manufacture of clean, reusable H_2. Several attempts have been made to create photocatalysts that can effectively use solar energy when exposed to visible light. Adjusting the photocatalyst with an appropriate cocatalyst to produce an active redox site will result in total water splitting over a photocatalyst particle. Zinc oxide (ZnO) is a superior photocatalyst compared to other materials due to its higher quantum efficiency, chemical stability, non-toxicity, and reduced cost. However, ZnO's large band gap (~3.37 eV) makes it undesirable for solar visible light absorption. Numerous attempts have been made to dope or couple ZnO with metals, non-metals, and metal oxides to move its absorption band from ultraviolet to the visible light region and enhance its performance. By improving optical absorbance and inhibiting charge carrier recombination, visible light active narrow band oxide semiconductor material may be created, which will increase photocatalytic activity. Because of its outstanding structural and chemical stability, as well as its narrow band gap (1.6 eV), $NiFe_2O_4$ is a promising option to address this issue.

The goal of this thesis study is combining nickel iron-based spinel oxides with ZnO to develop a hybrid material which has enhanced catalytic properties. Based on this scope, ZnO-$NiFe_2O_4$ nanocatalyst was synthesized and its electrocatalytic performance for the water oxidation reaction was investigated. More specifically, this dissertation conducted the research listed below:

- Synthesis of $ZnO-NiFe_2O_4$ hybrid nanomaterials.
- Characterization of produced nanomaterials by using different analytical methods like XRD, EDX, SEM, XPS, ICP-OES and BET.
- Examination of nanoparticles' catalytic abilities in the electrochemical water oxidation process.

CHAPTER 2

EXPERIMENTAL

2.1 Materials

Without additional purification, the original forms of all reagents were utilized. Nickel (II) nitrate hexahydrate (Ni $(NO_3)_2.6H_2O$), Iron (III) nitrate nonahydrate (Fe $(NO_3)_2.9H_2O$), Iron (II) chloride tetrahydrate ($FeCI_2.4H_2O$), zinc acetate $Zn(CH_3CO_2)_2$, Zinc nitrate hexahydrate ($Zn(NO_3)_2{\cdot}6H_2O$), sodium hydroxide (NaOH), urea, ethanol, nafion® perfluorinated resin solution (5% wt. in lower aliphatic alcohols and water) and DMF (dimethyl formamide) were bought from Sigma Aldrich. The aqueous solutions were prepared using deionized ultra-pure water with resistivity more than 18 MΩ (PURELAB Option-Q, Elga).

2.2 Synthesis of $NiFe_2O_4$, ZnO and ZnO-$NiFe_2O_4$ Nanoparticles with Hydrothermal and Sol-gel method

2.2.1 Synthesis of $NiFe_2O_4$ Nanoparticles with Hydrothermal Method

$NiFe_2O_4$ nanomaterials were obtained using the hydrothermal approach based on a previously described method with certain changes.[39] Shortly, 2.0 mmol of Iron (II) chloride tetrahydrate ($FeCI_2.4H_2O$), 4.0 mmol of Nickel (II) nitrate hexahydrate (Ni $(NO_3)_2$. $6H_2O$) and 12.0 mmol of urea (CH_4N_2O) were mixed with 40.0 mL of deionized water and stirred to form a homogeneous mixture. Later, the mixture was put into a 100 mL Teflon lined autoclave and held for 6 h at 180 °C. After cooling, the product was centrifuged and repeated washings with deionized water and ethanol. Lastly, the product was dried at 90°C overnight before being calcinated for 2 hours at 550°C.

2.2.2 Synthesis of ZnO Nanoparticles with Sol-gel Method

In this study, zinc acetate was used as a precursor in the sol-gel process to create zinc oxide (ZnO) nanoparticles (Figure 2.1). ZnO was synthesized by sol-gel process by following procedure reported in the literature with some changes.[40] Firstly, 50 mL of ethanol was used to dissolve 4.4 g of zinc acetate then used a magnetic stirrer to mix for 1 hour. The solution's pH was determined to be close to 3. NaOH was added drop by drop, to get the solution's pH up to 8. To obtain a homogenous gel, the solution was stirred for 3 hours. The synthesis took place at 60 °C. The gel was then left to age until the next day. Then, the solution was centrifuged and washed with ethanol and distilled water. After drying in oven overnight, it was then annealed at 500°C for 4 hours.

Figure 2. 1. Illustration of the synthesis of ZnO nanoparticles

2.2.3 Synthesis of ZnO-$NiFe_2O_4$ Nanoparticles with Hydrothermal Method

At room temperature, 2.0 mmol of pre-synthesized ZnO nanoparticles with sol-gel method (described in section 2.2.2), 2.0 mmol of Iron (II) chloride tetrahydrate ($FeCl_2.4H_2O$), 4.0 mmol of Nickel (II) nitrate hexahydrate (Ni $(NO_3)_2.6H_2O$) and 12.0 mmol of urea (CH_4N_2O) were mixed with 40.0 mL of DI water (deionized water) and mixed to get a homogeneous mixture. The solution was then placed in the Teflon-lined autoclave and sustained at 180°C for 6 hours. The solution was then centrifuged, the precipitate was separated, and washed by ethanol and deionized water. It was initially dried at 90°C before being calcinated for 2h at 550°C.

2.3 Synthesis of $NiFe_2O_4$, ZnO and ZnO-$NiFe_2O_4$ Nanoparticles with Solvothermal and Hydrothermal Method

2.3.1 Synthesis of $NiFe_2O_4$ Nanoparticles with Hydrotherml Method

2 mmol Ni $(NO_3)_2$.$6H_2O$ and 4 mmol Fe $(NO_3)_3$.$9H_2O$ were dissolved in 40 mL DI water and mixed under magnetic stirring for 30 min. Then, NaOH (2 M) solutions were added dropwise into the mixture with continuous stirring to adjust the pH value to 12**.** The suspension formed was transferred into Teflon-lined stainless autoclave. The autoclave was sealed and maintained at 180°C for 3 h. Next day, the autoclave was cooled naturally to room temperature and the resulting products were collected, washed with DI water, and dried at 70°C for overnight in an oven.

2.3.2 Synthesis of ZnO Nanoparticles with Solvothermal Method

0.01 mole (10 mmol) Zn $(NO_3)_2$.$6H_2O$ were dissolved in 40 mL ethanol and then mixed under magnetic stirring for 30 min. Then, NaOH (2 M) solutions were added dropwise into the mixture with continuous stirring to adjust the pH value to 12. The suspension formed was transferred into Teflon-lined stainless autoclave. The autoclave was sealed and maintained at 180°C for 3 h. Next day, the autoclave was cooled naturally to room temperature and the resulting products were collected, washed with DI water (centrifugation), and dried at 70°C for 2 h in an oven. The synthesis of ZnO nanoparticles with solvothermal method was shown in Figure 2.2.

Figure 2. 2. Illustration for the formation of ZnO nanoparticles

2.3.3 Synthesis of ZnO-$NiFe_2O_4$ Nanoparticles with Solvothermal Method

10 mmol Zn $(NO_3)_2 .6H_2O$ and 1 mmol $NiFe_2O_4$ nanoparticles (from synthesized in section 2.3.1) were dissolved in 40 mL ethanol and mixed under magnetic stirring for 30 min. Then, NaOH (2 M) solutions were added dropwise into the mixture with continuous stirring to adjust the pH value of the solution 12. The suspension formed was transferred into Teflon-lined stainless autoclave. The autoclave was sealed and maintained at 180°C for 3 h. Next day, the autoclave was cooled naturally to room temperature and the resulting products were collected, washed with DI water, and dried at 70°C for 2h in an oven. Figure 2.3 shows the formation of ZnO- $NiFe_2O_4$ nanoparticles with modified simple solvothermal method.

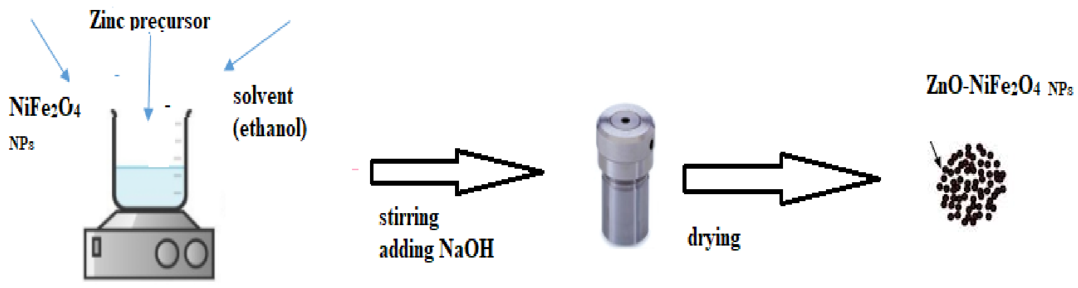

Figure 2. 3. Illustration for the formation of ZnO- $NiFe_2O_4$ nanoparticles

2.4 Materials Characterization

SEM images of nanomaterials and EDX (energy dispersive X-ray) elemental composition analyses were obtained using the FEI Nova Nano SEM 430. The phase of the nanomaterials was examined using a Rigaku Miniflex X-ray Diffractometer (XRD) with Cu Kα radiation (30 Kv, 15mA, λ = 1.54051 Å). The PHI-5000 Versa Probe [Physical Electronics (PHI) Chanhassen, Minneapolis, MN], fitted with an Al K source at 1486.92 eV, was used for X-ray photoelectron spectroscopy (XPS) investigations. All the data was adjusted for the study to the peak of hydrocarbon contamination at C1s (282.4 eV). Brunauer-Emmett-Teller (BET) analysis was performed using Autosorb-6 (Quantachrome Corporation) to ascertain the precise surface areas of the synthesized nanomaterials. All samples underwent a 5-hour dehydration process at 300 °C before analysis. Using a Perkin Elmer Optima 4300DV instrument, Inductively Coupled Plasma Optical Emission Spectroscopy (ICP-OES) was used to analyse the elemental composition of the nanomaterials and the mass proportion of each element in their structure.

2.5 Electrochemical Characterization

2.5.1 Electrode Preparation

In this work, the electrochemical properties of nanoparticles were investigated by using Glassy carbon electrodes (GCEs). GCEs with a 0.07 cm^2 surface area have been modified and used as working electrodes. The GCEs were prepared using a modified version of a technique that was previously published by Kuo et al.[41] In short, 2.0 mL of DMF and 11.2 mg of catalysts were mixed, and the resulting mixture was then sonicated. After 30 minutes, 19 L of Nafion® solution was added, and 2 hours of sonication produced a homogenous ink. The ink was poured over GCE in 5.0 µL, and it was allowed to dry overnight at 90 °C in the oven.

.

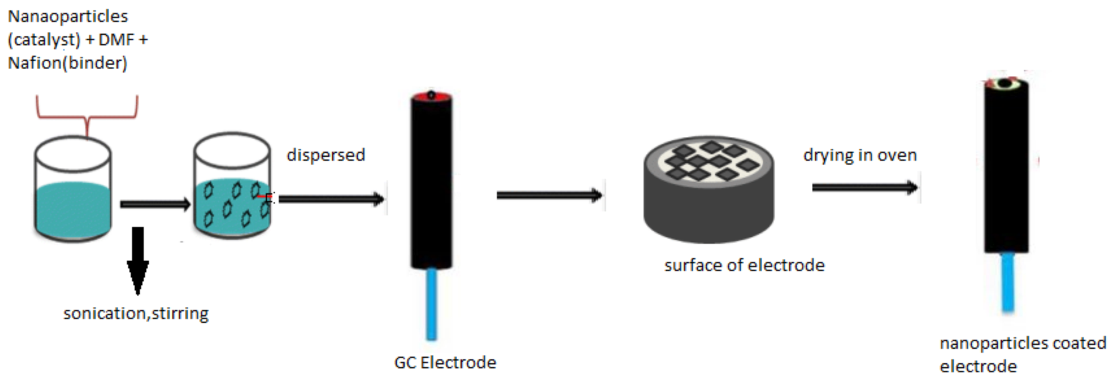

Figure 2. 4. Scheme illustrating the modification of GCE with catalyst

2.5.2 Electrochemical Measurement

Using a Gamry 1010B potentiostat-galvanostat and a conventional 3-electrode setup, electrochemical investigations were carried out (Figure 2.5). Pt wire was used for the counter electrode (CE) and Ag/AgCl (in 3.0 M KCl) was the reference electrode (RE) in this three-electrode setup. GCEs coated with nanoparticles were used as working electrode (WE).

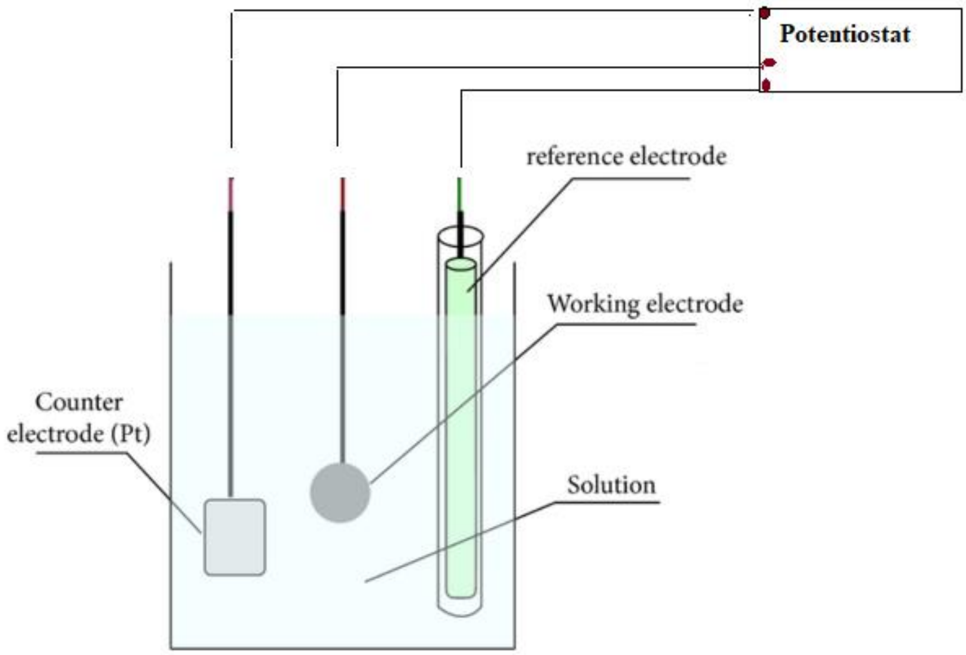

Figure 2. 5. Schematic representation of a standard three-electrode setup for electrochemical studies of electrodes treated with nanoparticles.

In the solution of 0.1 M KOH at room temperature, electrochemical characteristics of the modified electrodes were analysed. Polarization curves were taken at a 5 mV s^{-1} scan rate. In this study, whole potential measurements were made against RHE (reversible hydrogen electrode). The obtained potential was converted RHE (against Ag/AgCl) using Nernst's equation (2.1), and the overpotential (η) was determined by using equation (2.2).

$$E_{RHE} = E_{Ag/AgCl} + 0.059\ pH + E^{\circ}_{Ag/AgCl} \quad (2.1)$$

$$\eta = E_{RHE} - 1.23\ V \quad (2.2)$$

Tafel equation ($\eta = a + b.\log(j)$) was fitted to the linear portion of the polarization curves to explain the kinetics of nanoparticles in water oxidation where η is the overpotential, a is the intercept resulting in exchange current density j, and b is Tafel slope.

To determine the surface area that is electrochemically active (ECSA) of the catalysts, the C_{dl} (electrochemical double-layer capacitance) was calculated. Cyclic voltammograms (CVs) were performed on catalysts at 5-10-15-20-25 mV s^{-1} scan rates in non-Faradaic region of 1.165-1.265 V (vs RHE) to calculate C_{dl} values. Plotting the double-layer charging current (at 1.26 V vs RHE) vs scan rate resulted in a straight line with a slope that represents the C_{dl} values of the catalysts. Equation (1.8) was used to get the values of ECSA. The sample's specific capacitance is C_s, and for smooth metal oxide surfaces, C_s equals 0.06 mF cm^{-2}. ECSA of the catalyst divided by GSA of the electrode resulted in the calculation of the surface roughness factor (RF) (equation 1.9) where GSA is the geometric surface area of the electrode.

Equation (2.3) was utilised to determine the mass activity (A g^{-1}) values at a specific overpotential.

$$\text{Mass activity} = j / m \tag{2.3}$$

m: catalyst loading (mg/cm^2), j : current density

Equation (2.4) was utilized to assess the catalyst's specific activity.

$$\text{Specific activity} = i / ECSA \tag{2.4}$$

i: current obtained at a specific potential.

CHAPTER 3

RESULTS AND DISCUSSION

In this study, ZnO-$NiFe_2O_4$ hybrid nanomaterials were synthesized with two different methods. First method involves the synthesis of ZnO nanoparticles via sol gel method followed by the addition of these already prepared particles into the mixture of metal precursors (Nickel and Iron salts) and structure directing agent (urea). The mixture components were then allowed to react to form the desired hybrid material via hydrothermal method. In this method, urea used as a structure directing agent which coordinate to metal ions present in the solution, and thus initiate the formation of ZnO-$NiFe_2O_4$ hybrid nanomaterials.

In second method, synthesis of $NiFe_2O_4$ nanoparticles followed by their addition to a solution of zinc metal precursors for the formation of ZnO-$NiFe_2O_4$ hybrid nanomaterial by solvothermal method. In this method, $NiFe_2O_4$ nanoparticles were expected to be nucleation sites for the formation of ZnO component of the hybrid material.

These nanomaterials were characterized by some various analytical techniques like SEM, XRD, ICP-OES, BET and XPS. The following sections discuss the results of these analyses in detail.

3.1 NANOPARTICLE CHARACTERIZATION: SURFACE AND STRUCTURAL

3.1.1 Structural and Surface Characterization of $NiFe_2O_4$, ZnO and ZnO- $NiFe_2O_4$ Nanoparticles

3.1.1.1 Characterization of $NiFe_2O_4$ Nanoparticles Synthesized with Hydrothermal Method

$NiFe_2O_4$ nanoparticles were synthesized based on previously reported procedure.[18] NaOH serves as a precipitating agent. Figure 3.1 shows the formation of $NiFe_2O_4$ nanoparticles, and the reaction mechanism can be described in equation (3.1). Figure 3.2. (a-d) shows SEM images of the nanoparticles. Finding out the sample surfaces' shape and microstructure is the aim of this analysis. Particles are aggregate crystals with irregular shapes. EDX analysis shows that the synthesized nanomaterial consists of Ni, Fe and O elements (Figure 3.3).

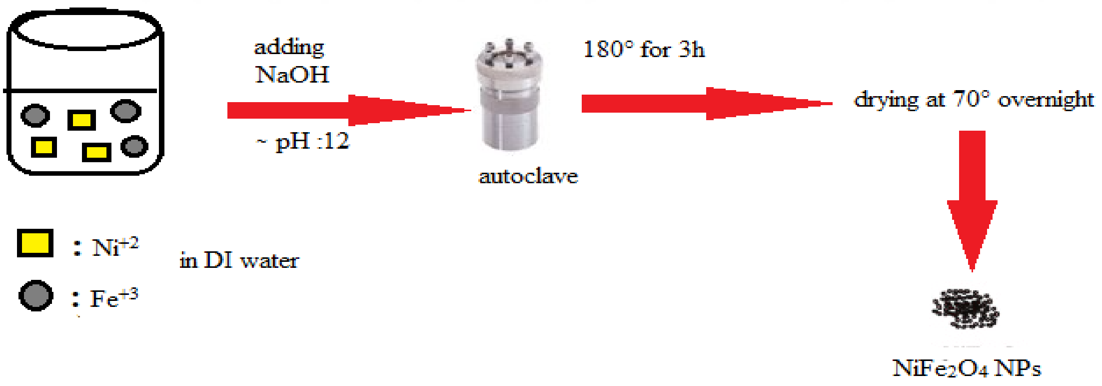

Figure 3. 1. Illustration for the formation of $NiFe_2O_4$ nanoparticles

$$Ni(NO_3)_2 + 2\,Fe(NO_3)_3 + 8\,NaOH \longrightarrow NiFe_2O_4 + 8\,NaNO_3 + 4\,H_2O \qquad (3.1)$$

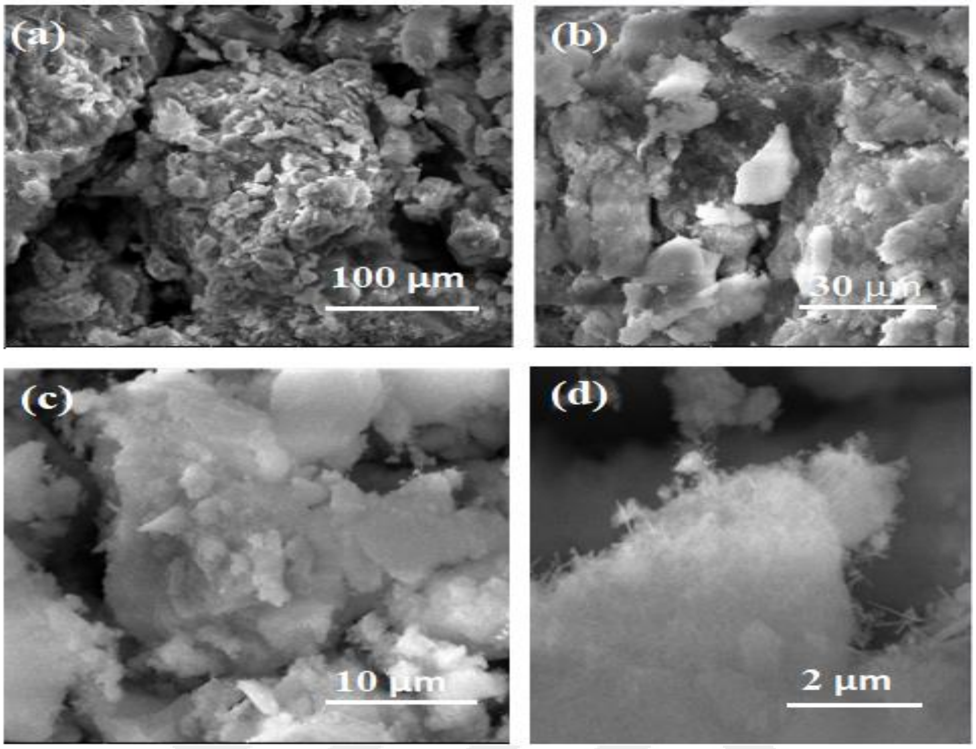

Figure 3. 2. (a-d) SEM pictures of $NiFe_2O_4$ nanoparticles

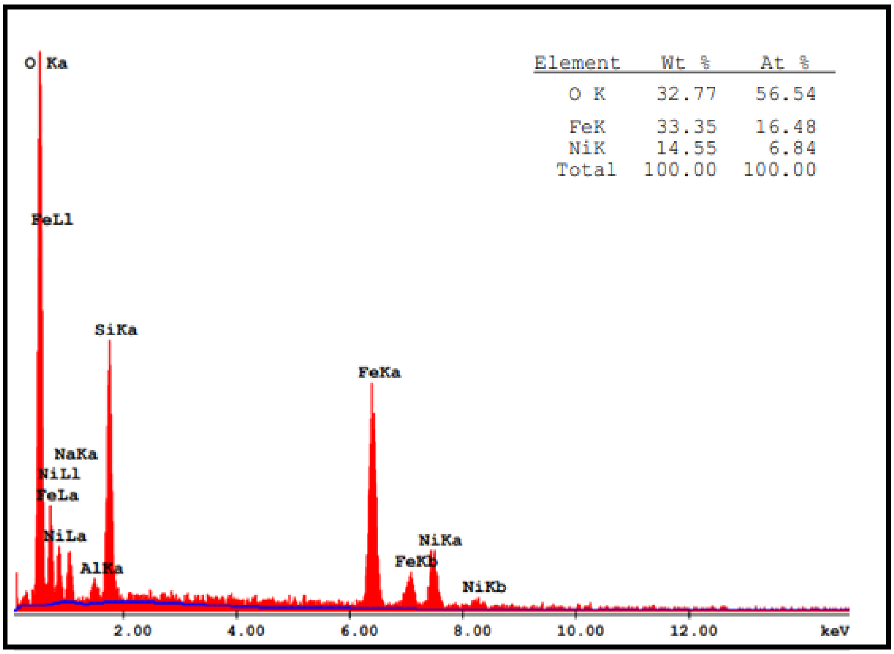

Figure 3. 3. EDX spectrum of $NiFe_2O_4$ nanoparticles

Figure 3.4. shows the XRD pattern of the $NiFe_2O_4$ nanoparticles. The $NiFe_2O_4$ sample's diffraction peaks can be seen at 2θ: 21.57°, 30.87°, 34.88°, 36.89°, 43.59°, 47.45°, 53.59°, 57.68°, 63.29° ,71.91° and 74.65° corresponding to the (111) (220), (311), (222), (400), (331), (422), (511), (440), (620) and (533) crystal planes of the $NiFe_2O_4$ (JCPDS No.54-0964).[42] The absence of distinct diffraction peaks for the $NiFe_2O_4$ sample can be seen, indicating that the material can be still in the amorphous phase. Also shown at 2θ values of 33.51°, 41.29°, 59.31°, 61.58° and 64.01° are the peaks belonging to (104), (113), (018), (214) and (300) planes of α-Fe_2O_3 phase (JCPDS No.79-0007)[43] , demonstrating the production of α-Fe_2O_3 phase along with $NiFe_2O_4$. The Scherrer equation was used to determine the crystallite size of materials and it was found as 14.9 nm. This analysis was conducted for the diffraction peak at 36.89° (222), applying the Debye–Scherrer equation (1.1).

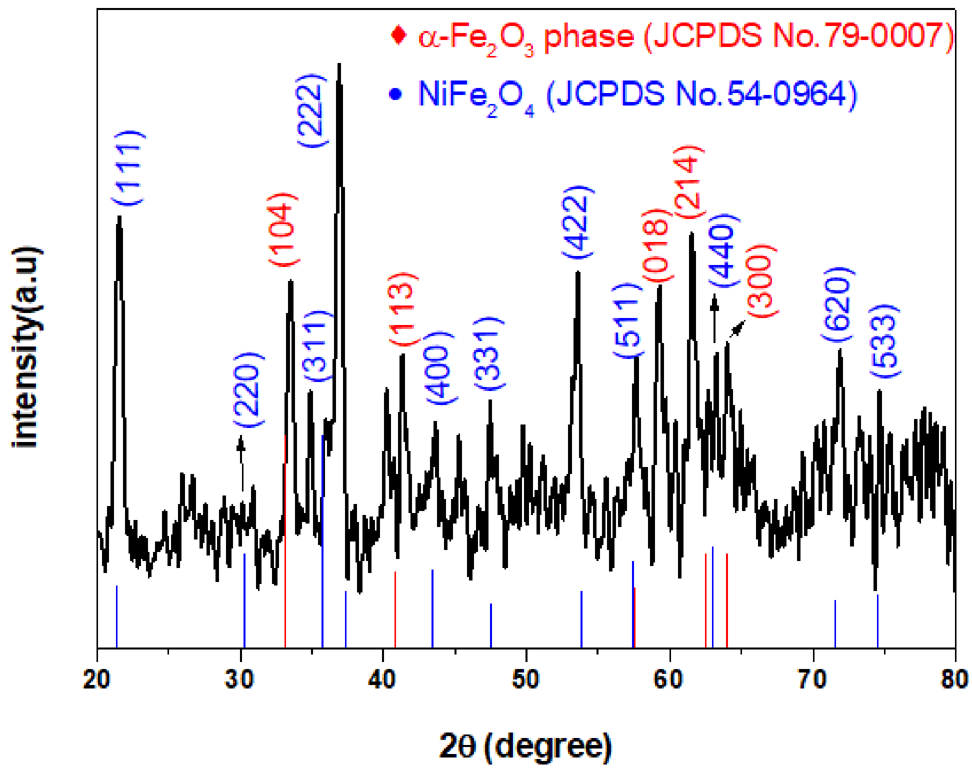

Figure 3. 4. XRD pattern of $NiFe_2O_4$ nanoparticles

3.1.1.2 ZnO Nanoparticles Synthesized with Solvothermal Method

Figure 3.5. (a-d) shows SEM images of the ZnO nanoparticles at different magnifications. SEM micrographs clearly show the roughly and irregular hexagonal forms of ZnO nanoparticles' and EDX analysis shows that the nanostructures are made up of both Zn and O elements (Figure 3.6).

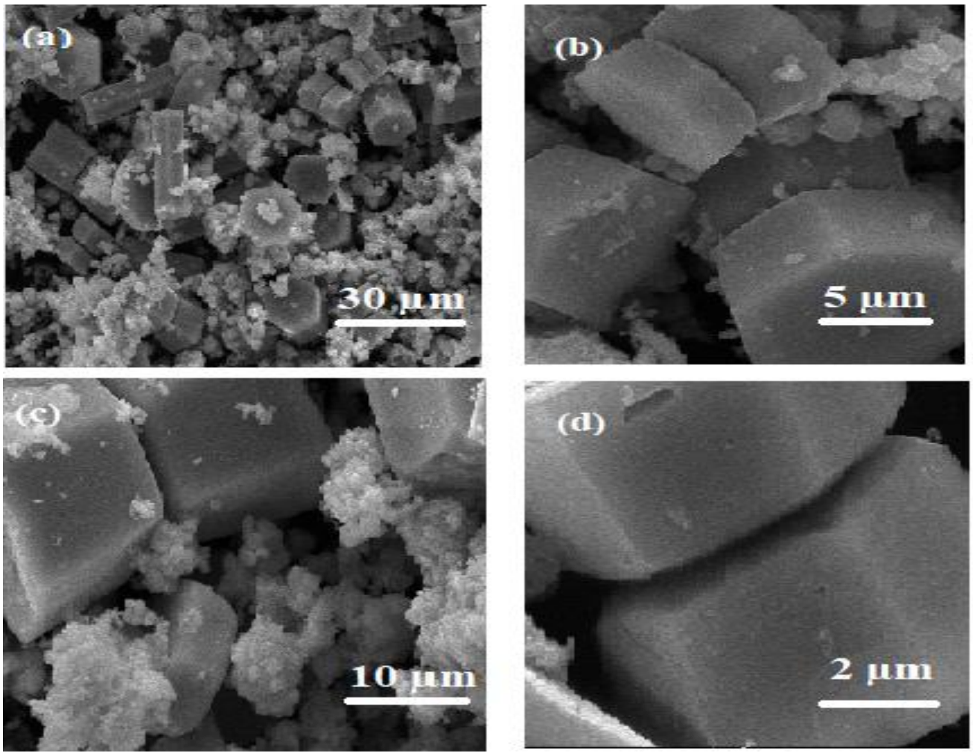

Figure 3. 5. (a-d) SEM images of ZnO Nanoparticles

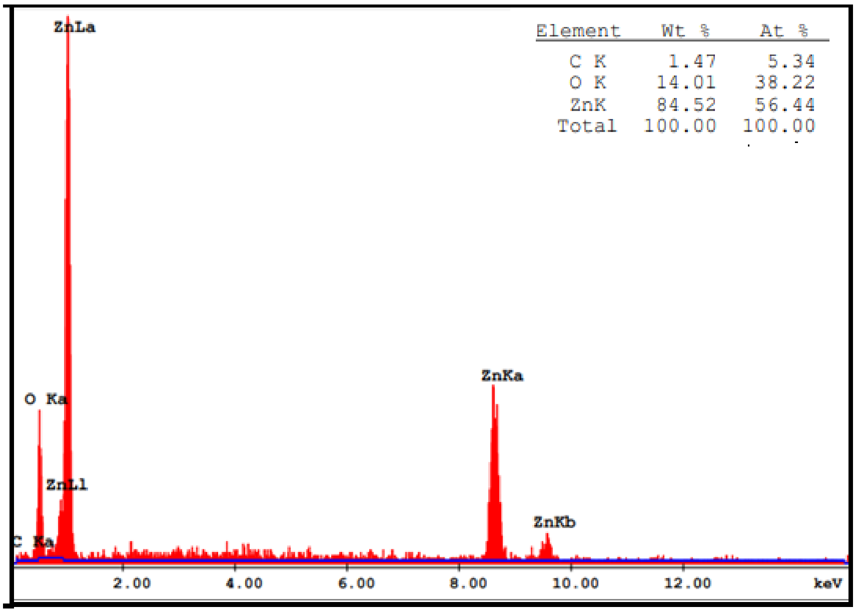

Figure 3. 6. EDX spectrum of ZnO nanoparticles

Figure 3.7. demonstrates the XRD pattern of the ZnO nanoparticles. The ZnO sample's diffraction peaks can be seen at 2 θ: 31.88°, 34.5°, 36.37°, 47.64°, 56.64°, 62.9°, 66.44°, 67.95°,69.13°,72.57° and 77.04° referred to (100), (002), (101), (102), (110), (103), (200), (112), (201), (004), (202).Confirmation of the desired material's synthesis and crystalline structure is provided by the peak's positions and intensities. The hexagonal wurtzite structure of zinc oxide is analogous to observed peaks (JCPDS No. 36-1451).[18]

The maximum intensity peak was observed for (101) face with 2θ value of 36.37°. For the 36.37° diffraction peak, the Debye-Scherrer equation (1.1)[29] was applied. ZnO crystallites were found to have a size of 34.1 nm after analysis.

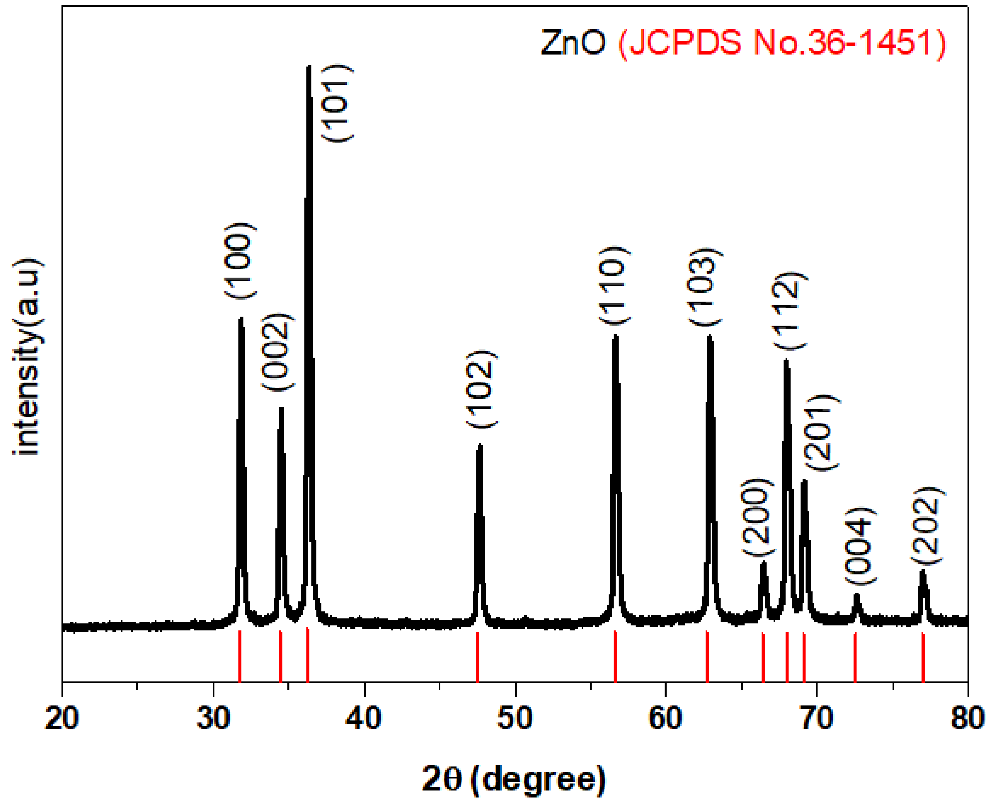

Figure 3. 7. XRD pattern of ZnO nanoparticles

3.1.1.3 ZnO-$NiFe_2O_4$ Nanoparticles Synthesized with Solvothermal Method

Figure 3.8. (a-d) shows SEM images of the ZnO- $NiFe_2O_4$ nanoparticles. According to the SEM images, the ZnO- $NiFe_2O_4$ nanomaterial has irregular morphology which quite similar to the one of ZnO nanoparticles. EDX analysis shows that the nanostructures are made up of Zn and O elements (Figure 3.9). This can be explained as follows: Either Ni and Fe percentages are too small, and they do not appear in the spectrum, or the followed procedure was unsuccessful.

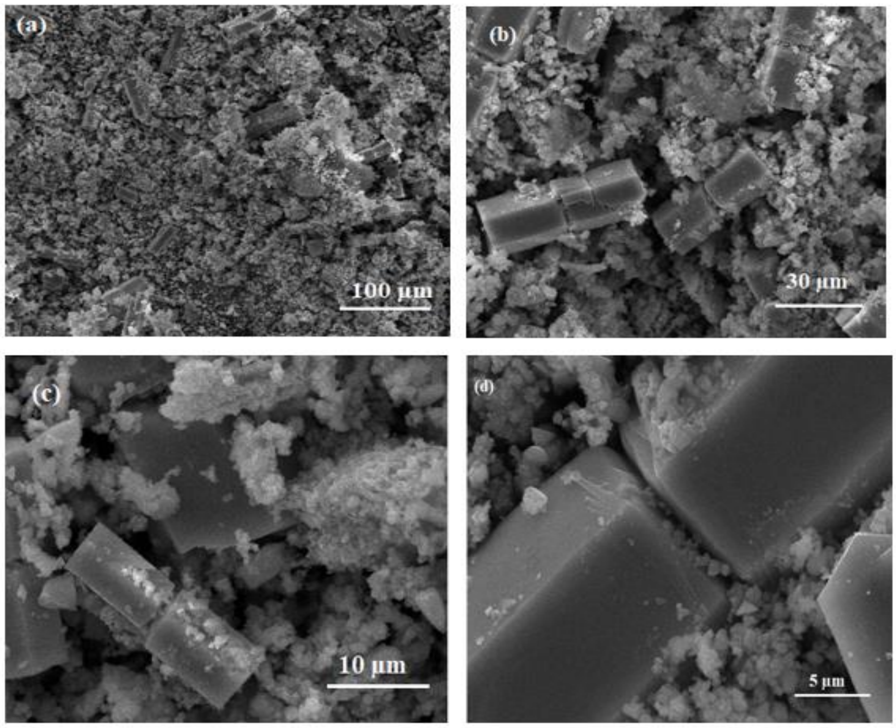

Figure 3. 8. (a-d) SEM images of the ZnO- $NiFe_2O_4$ nanoparticles

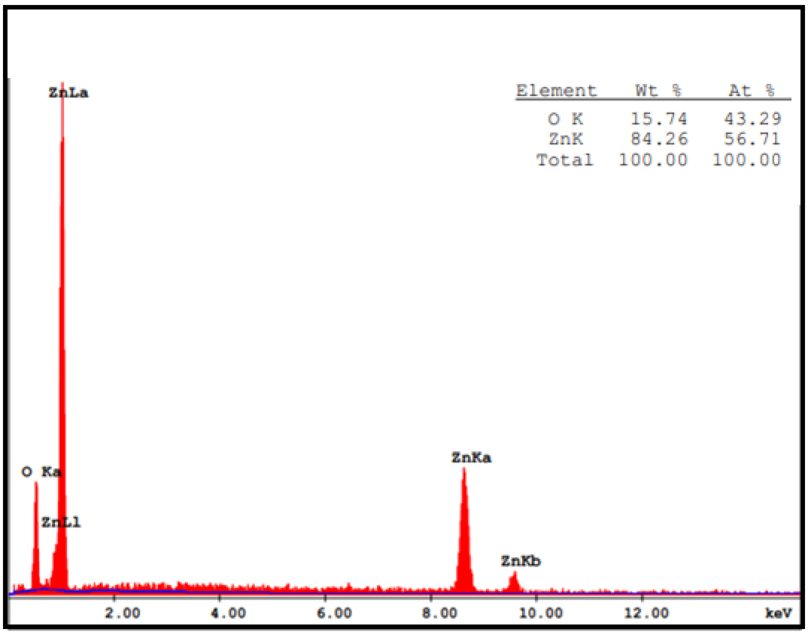

Figure 3. 9. EDX of the ZnO- $NiFe_2O_4$ nanoparticles

Figure 3.10. shows the XRD pattern of ZnO- $NiFe_2O_4$ nanoparticles. ZnO- $NiFe_2O_4$ nanoparticles ' XRD pattern is quite similar to the one of ZnO. There are possible reasons for this observation. First reason might be the significantly low amount of $NiFe_2O_4$ present in synthesized material. Another potential reason is the very small size of $NiFe_2O_4$ nanoparticles, which make their XRD peaks very broad and thus undetectable. The planes of (100), (002), (101), (102), (110), (103), (200), (112), (201), (004) and (202) correlate to the observed peaks that formed at the 31.79°, 34.44°, 36.29°, 47.53°, 56.57°, 62.84°, 66.33°, 67.91°,69.05°,72.53° and 76.9°, respectively. This suggests the presence ZnO (JCPDS No. 36-1451). The peak of $NiFe_2O_4$ only at 47.53° shows high intensity which correspond to (331) plane (JCPDS No.54-0964). Using XRD peak analysis, the crystallite sizes were determined, and the size of the ZnO-$NiFe_2O_4$ nanostructures was found to be 22.24 nm. The Debye–Scherrer equation (1.1) was used to do this study on the diffraction peak at 36.29° (101).

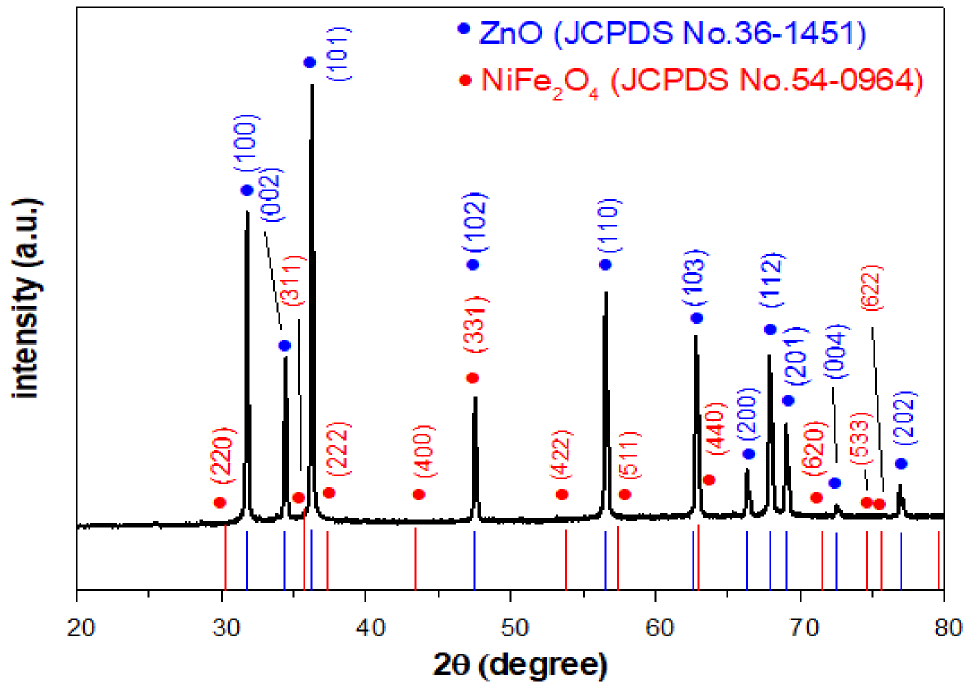

Figure 3. 10. XRD spectrum of ZnO- $NiFe_2O_4$ nanoparticles

3.1.1.4 $NiFe_2O_4$ -NiO Nanoparticles Synthesized with Hydrothermal Method

Urea was used as the surfactant in hydrothermal technique to produce $NiFe_2O_4$ nanoparticles. The urea molecules were able to interact with the ions Ni^{2+} and Fe^{2+} to create a precursor complex of Nickel-Ferrite-urea, which was then air-calcined to produce $NiFe_2O_4$-NiO nanoparticles (Figure 3.11). Figure 3.12. (a-d) shows SEM images of the materials. SEM pictures show that the nanoparticle, which is created by assembling tiny flakes, has a spherical-like shape. According to EDX analysis, the nanostructures are made up of both Ni and Fe components (Figure 3.13).

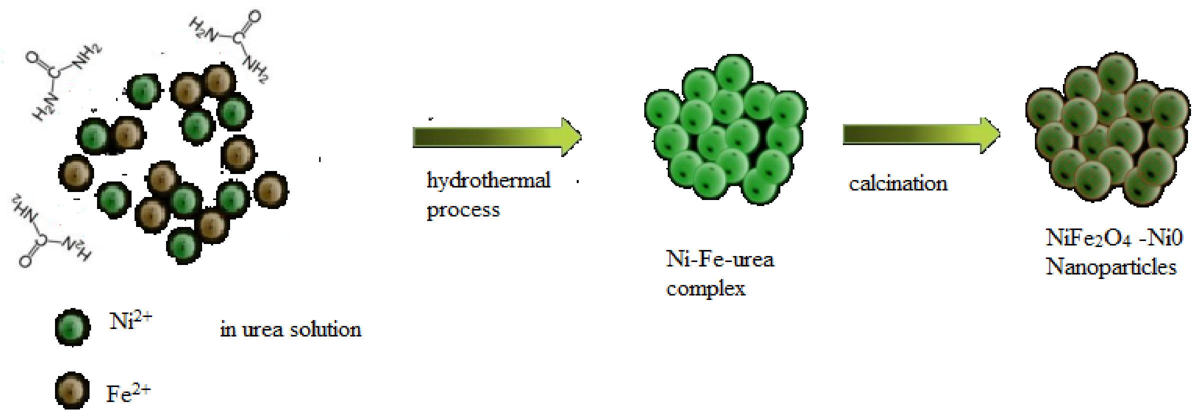

Figure 3. 11. Illustration for the synthesis of $NiFe_2O_4$-NiO nanoparticles

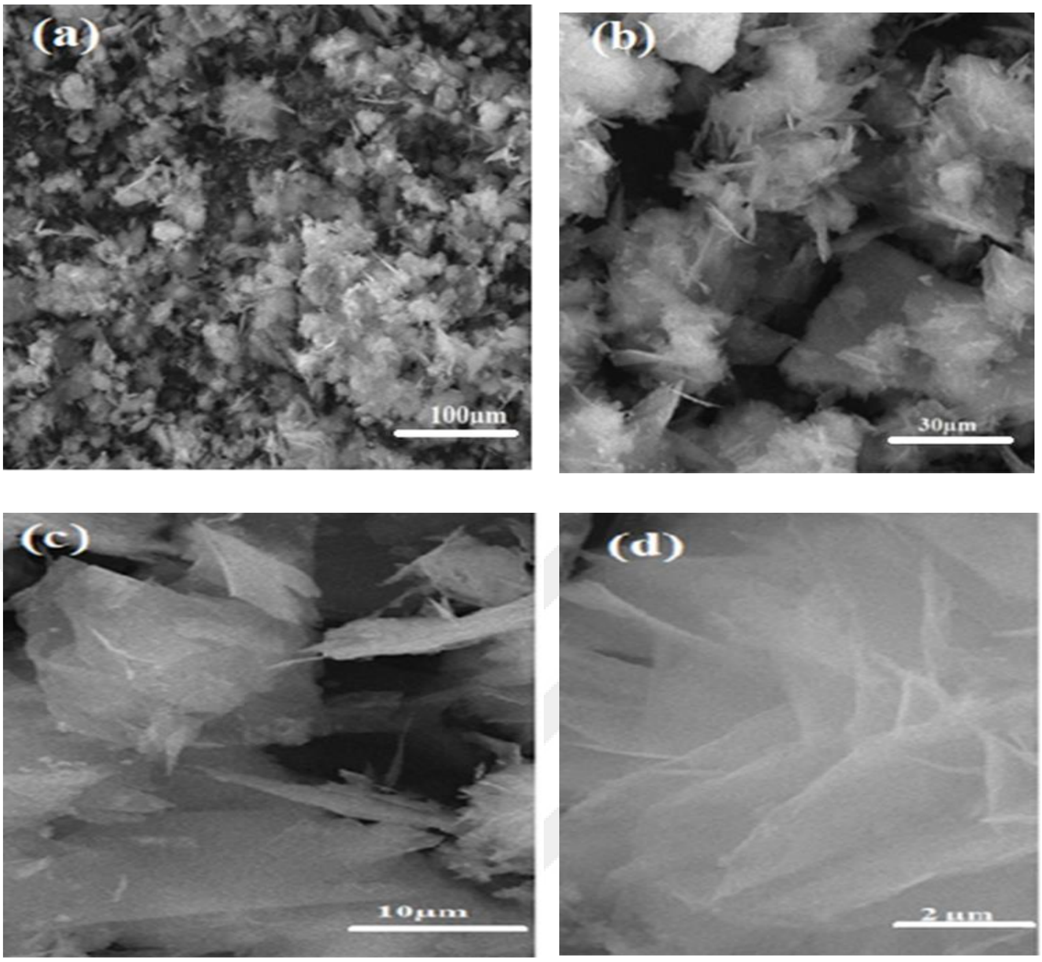

Figure 3. 12. (a-d) $NiFe_2O_4$ nanoparticles' SEM images at different magnifications.

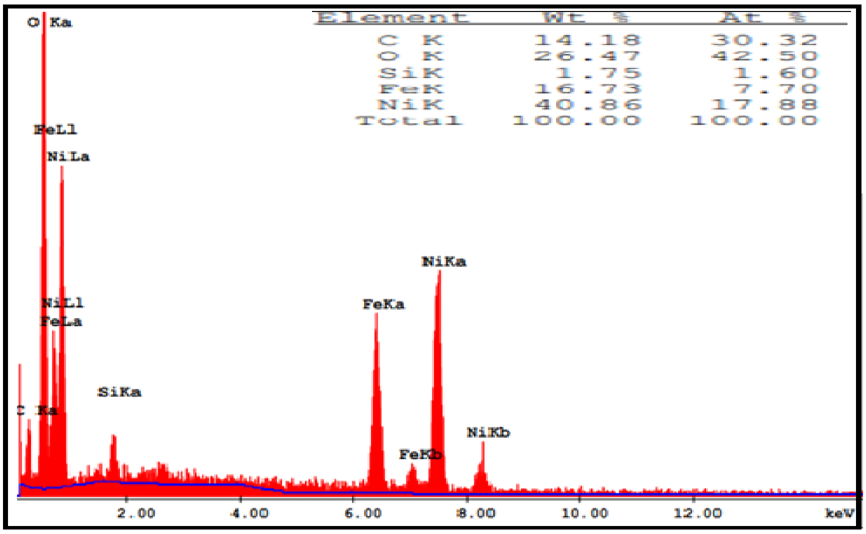

Figure 3. 13. $NiFe_2O_4$ nanomaterials' EDX spectrum

$NiFe_2O_4$-NiO nanoparticles' XRD pattern is given in Figure 3.14.The $NiFe_2O_4$ planes (111), (220), (311), (222), (400), (422), (511), (440), (620), and (533) are corresponding to the peaks with 2θ values of 18.31°, 30.47°, 35.77°, 37.36°, 43.44°, 54.02°, 57.56°, 63.16°, 71.57°, and 74.82°, respectively (JCPDS No.54-0964). Also shown at 2θ values of 37.36°, 43.44°, 63.16°, and 75.44° are the peaks belonging to (111), (200), (220), and (311) cubic planes of NiO (JCPDS No. 01-071-1179), demonstrating the production of NiO and $NiFe_2O_4$ together. $NiFe_2O_4$'s (222), (400), and (440) diffraction peaks overlap to the (111), (200), and (220) peaks of NiO, respectively. The result is mostly due to the similarities between the unit cell characteristics of $NiFe_2O_4$ and NiO. The size of the crystallite was estimated to be around 10.05 nm by using the diffraction peak at 43.44°.

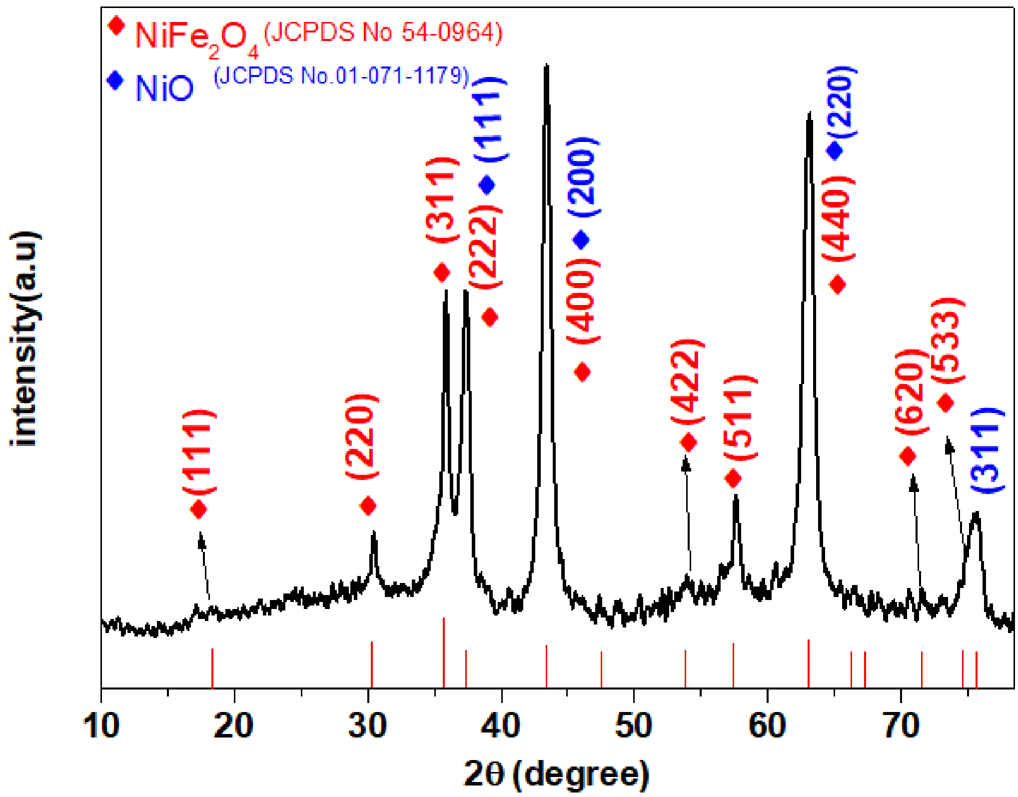

Figure 3. 14. XRD pattern of $NiFe_2O_4$-NiO nanoparticles

3.1.1.5 ZnO Nanoparticles Synthesized with Sol-Gel Method

Figure 3.15. (a-d) displays the SEM images of ZnO nanopowder produced via sol-gel synthesis at various magnifications. The outcome emphatically demonstrates that the produced ZnO has a flaky structure. According to the micrographs, these ZnO nanocrystalline flakes have an asymmetrical, spherical form. To evaluate the stoichiometry of the sample's constituents, energy dispersive X-ray spectroscopy was employed. In Figure 3.16, the EDX spectrum is displayed. The resulting spectrum verifies that the produced sample contains the Zn and O components.

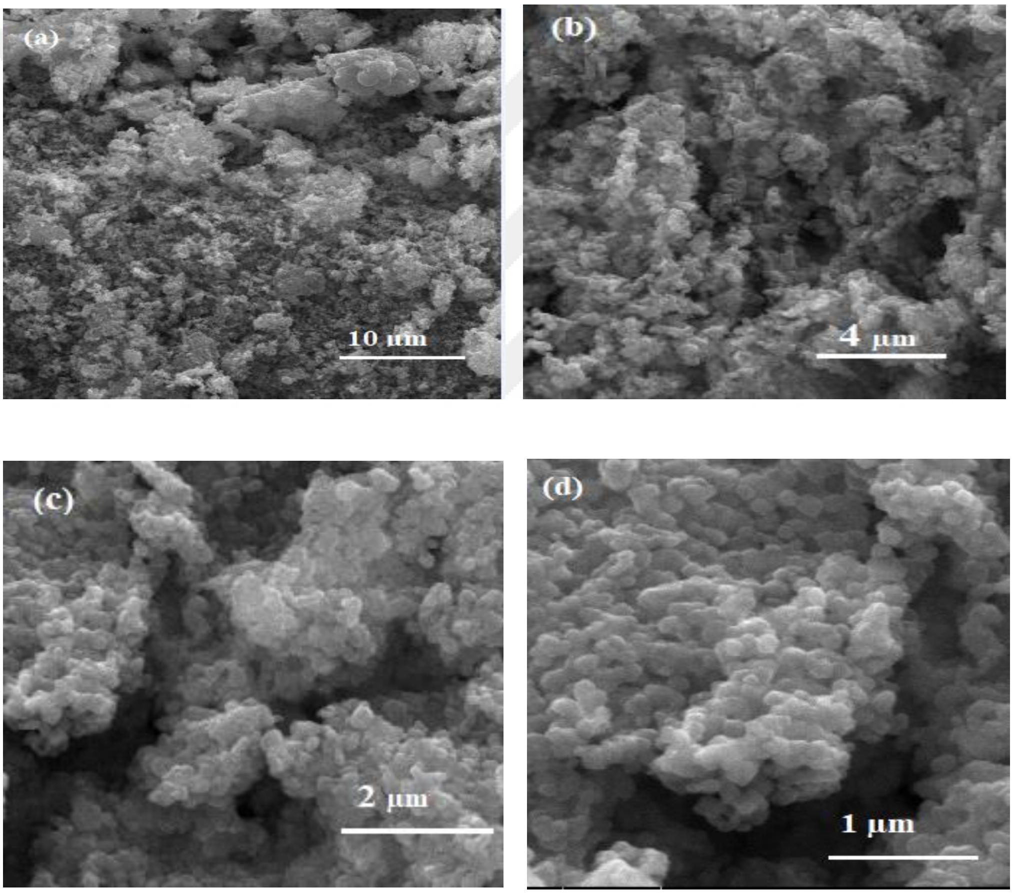

Figure 3. 15. (a-d) SEM images of ZnO nanoparticles

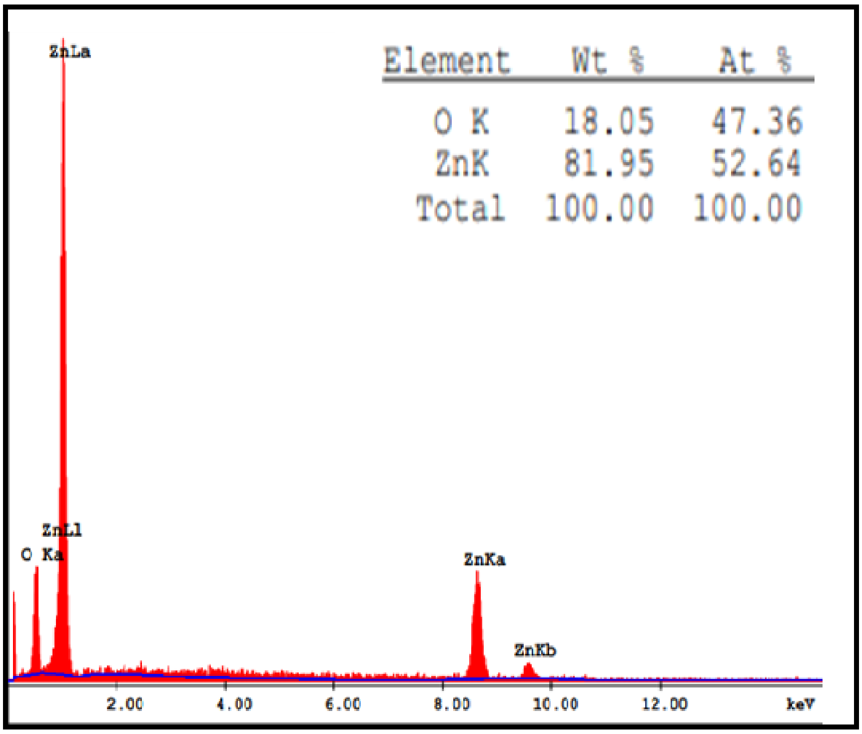

Figure 3. 16. EDX spectrum of ZnO nanomaterials

Figure 3.17. displays the X-ray diffraction peaks of ZnO nanoparticles. The peaks at 31.85° (100), 34.54° (002), 36.36° (101), 47.63° (102), 56.71° (110), 62.95° (103), 66.47° (200), 68.08° (112), 69.18° (201), 72.64° (004), and 76.91° (202) distinctly indicate the existence of a hexagonal wurtzite ZnO structure (JCPDS No.36-1451)[44]. The (101) face has the highest intensity peak at 2θ value of 36.36° and the obtained peak values match very closely. The peaks' sharpness confirms that the synthetic substance is crystalline. Based on the diffraction peak at 36.36°, the crystallite size was determined to be around 23.9 nm.

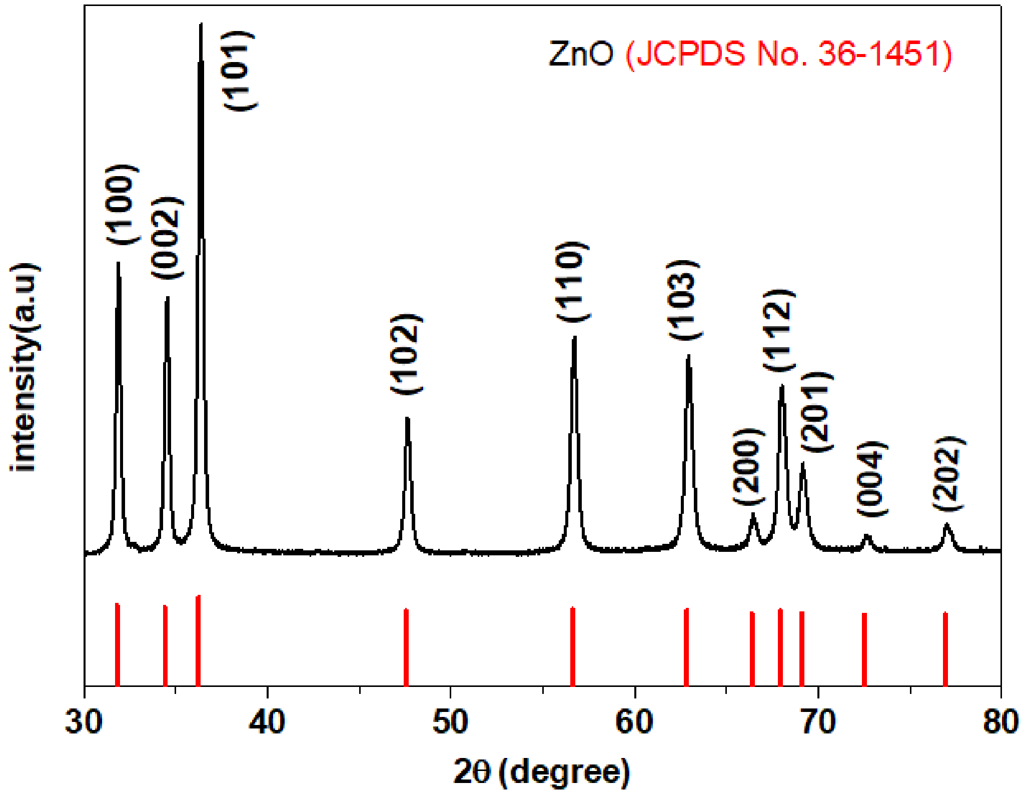

Figure 3. 17. XRD pattern of ZnO nanoparticles

3.1.1.6 ZnO- $NiFe_2O_4$ Nanoparticles Synthesized with Hydrothermal Method

ZnO-$NiFe_2O_4$ hybrid materials were synthesized with hydrothermal method in which urea was used as a surfactant (Figure 3.18). Figure 3.19. (a-d) displays the SEM images of synthesized nanoparticle. The results demonstrate that ZnO-$NiFe_2O_4$ hybrid material has a flaky structure which is most likely formed by the assembly of individual nanoparticles. According to the micrographs taken at lower magnification, these ZnO-$NiFe_2O_4$ nanocrystalline flakes assemble to form spherical-like micro-materials. The particles' EDX spectra confirm that Ni, Fe and Zn elements are present in the synthesized materials (Figure 3.20).

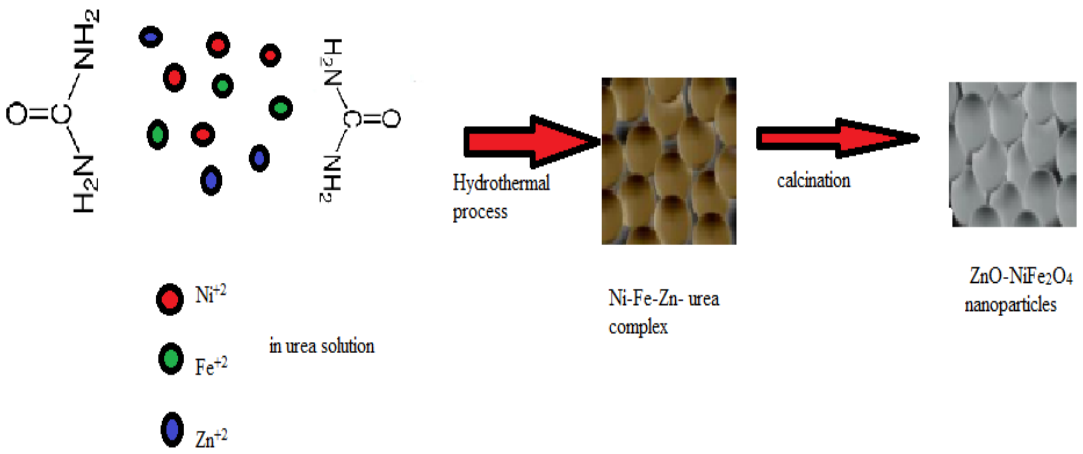

Figure 3. 18. Illustration of the synthesis of ZnO-$NiFe_2O_4$ nanomaterials

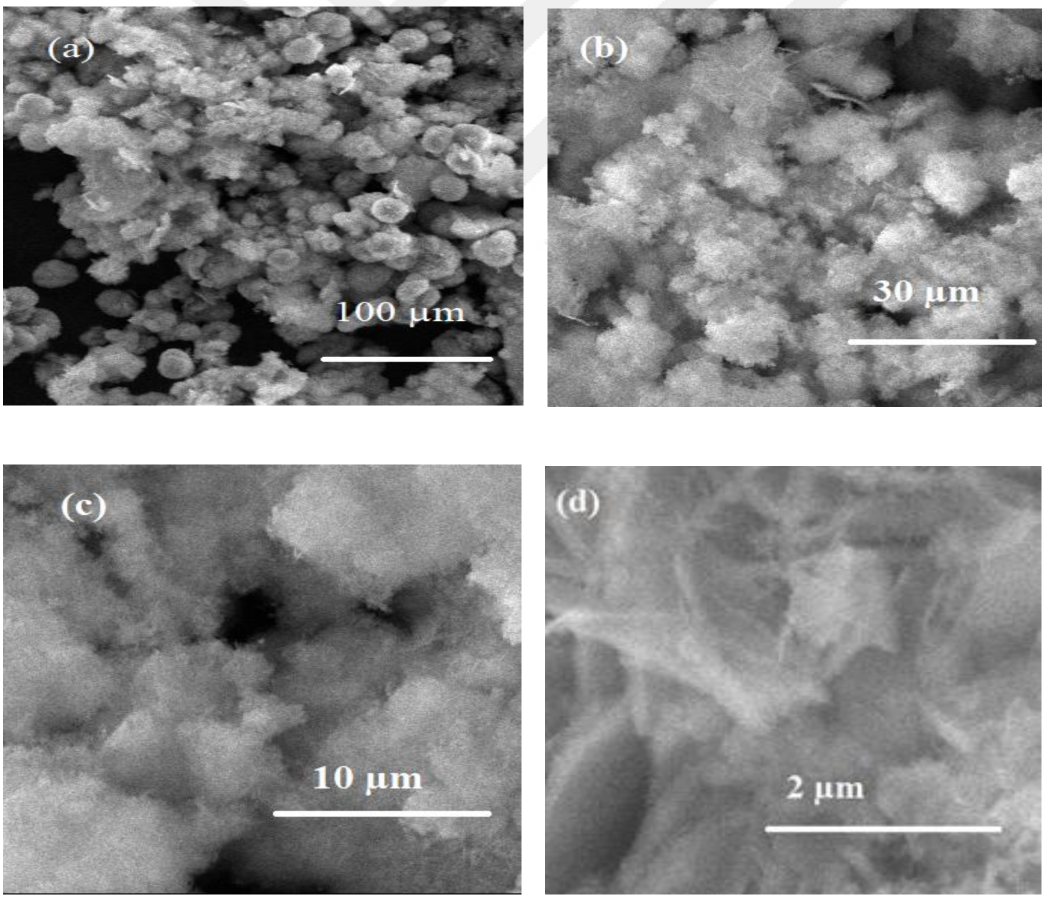

Figure 3. 19. (a-d) SEM images of ZnO-$NiFe_2O_4$ nanomaterials at different magnifications

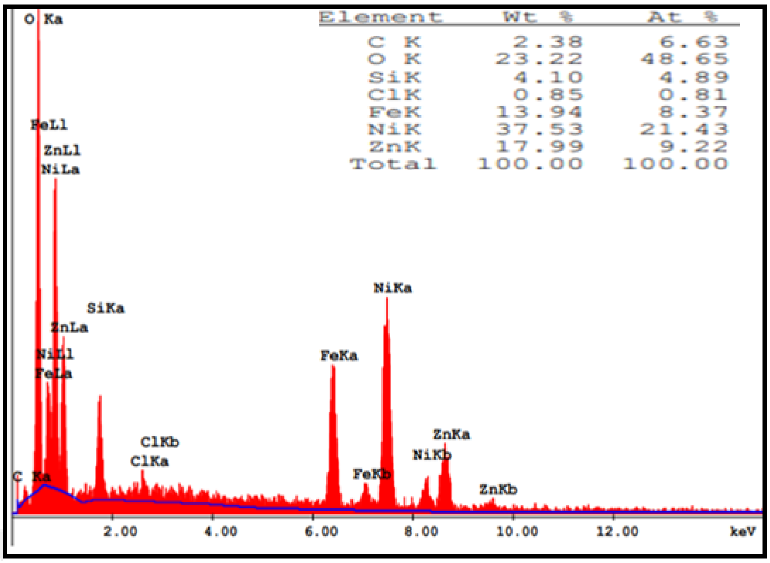

Figure 3. 20. EDX spectrum of ZnO-$NiFe_2O_4$ nanomaterials

The XRD pattern of ZnO-$NiFe_2O_4$ nanomaterials is seen in Figure 3.21. The peaks at 2θ values 31.75°, 47.57°, 56.67°, 62.85°, 67.85°, 69.04° belong to the (100), (102), (110), (103), (112), (201) hexagonal ZnO planes (JCPDS No.36-1451). However, the only peak at 62.85° has high intensity and the other peaks which are in lower intensity almost disappeared. The reason for this observation may be that the $NiFe_2O_4$ particles covered the ZnO particles forming core (ZnO)-shell ($NiFe_2O_4$) type structure. On the other hand, the peaks at 30.32°, 35.69°, 37.36°, 43.27°, 53.74°, 57.31°, 62.85°, 71.18° and 74.47° correspond to planes (220), (311), (222), (400), (422), (511), (440), (620) and (533) of the $NiFe_2O_4$ nanoparticles (JCPDS No.54-0964). Also shown at 2θ values of 37.36°, 43.27°, 62,85°, and 75.04° are peaks belonging to the (111), (200), (220), and (311) cubic planes NiO (JCPDS No. 01-071-1179). Additionally, Debye-Scherrer equation (1.1) was utilized for diffraction peak at 62.85°. The size of the ZnO-$NiFe_2O_4$ crystallites was determined through analysis to be 17.7 nm.

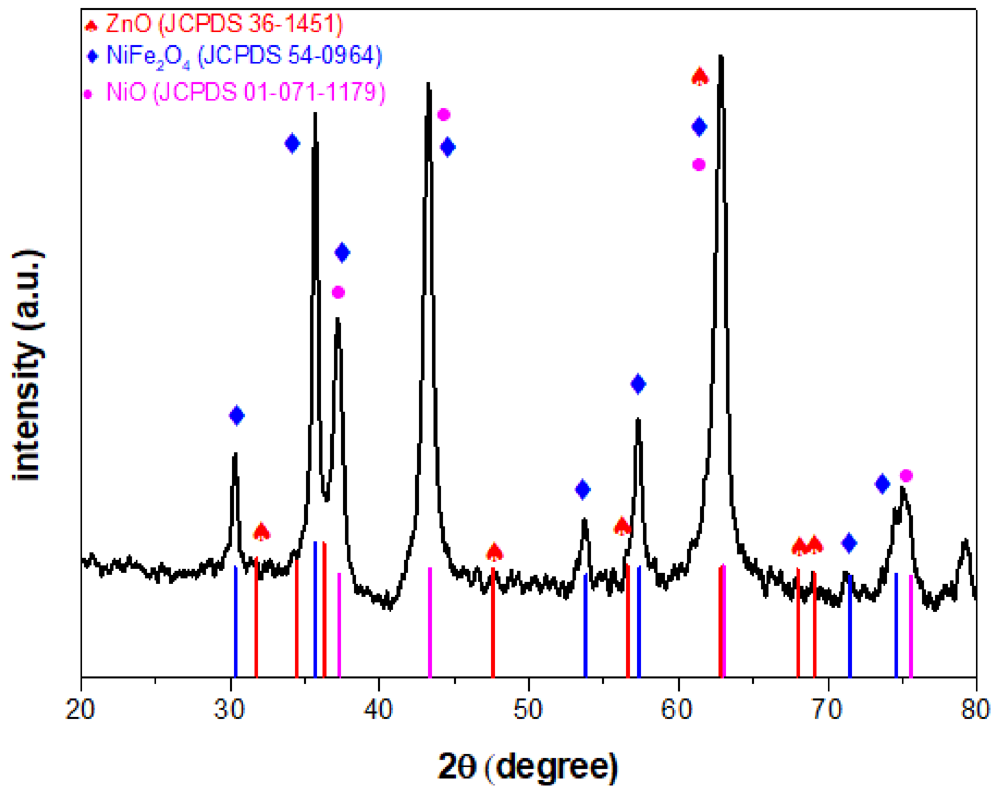

Figure 3. 21. The XRD pattern of ZnO-$NiFe_2O_4$ nanoparticles

The XPS spectra of ZnO-$NiFe_2O_4$ nanoparticles are shown in Figure 3.22. The absence of any impurities in the as-synthesised material is strongly suggested by the presence of only Ni, Fe, Zn, and O elements in the survey spectrum (Figure 3.22a), except for C1s at 282.4 eV utilised for calibration. Figure 3.22b shows the Ni 2p core level spectrum. Together with two shakeup satellite peaks, two distinct peaks at 854.5 eV and 872.1 eV, corresponding to Ni $2p_{3/2}$ and Ni $2p_{1/2}$, were observed. These peaks indicate the existence of Ni^{2+} in the materials.[45,46]

Ni^{2+} (at 871.8 eV and 852.9 eV) and Ni^{3+} (at 872.8 eV and 855.5 eV) are attributed to the two Gaussian bands that were produced by the fitting process. The positions of these observed peaks and those in earlier investigations are in good agreement.[47,48] Figure 3.22c shows two peaks, $2p_{3/2}$ and $2p_{1/2}$, at 711.3 eV and 723.8 eV, respectively, in the Fe 2p core level spectrum. The absence of satellite peaks indicates that neither Fe_2O_3 nor Fe_3O_4 are generated. The XPS spectra of Zn 2p is shown in Figure 3.22d. This spectrum shows peaks for Zn $2p_{1/2}$ at 1044.2 eV and Zn $2p_{3/2}$ at 1020.8 eV, respectively. Observed peaks indicate the existence of Zn in two different oxidation states, as expected.[49] Three peaks can be seen in the O 1s spectra at 528.8 eV (I), 530.4 eV (II) and 531.2 eV (III) (Figure 3.22e). Zinc oxide nanocrystals' surface likely contains weakly bound oxygen, which is the reason for the lower binding energy peak (I) in the O 1s spectrum.[50,51] .In regions of the ZnO matrix with low oxygen content, O^{2-} ions are linked to the middle binding energy peak (II). Finally, the higher binding energy peak (III) displays the O^{2-} ions in the wurtzite structure of the hexagonal Zn^{2+} ion array.[51]

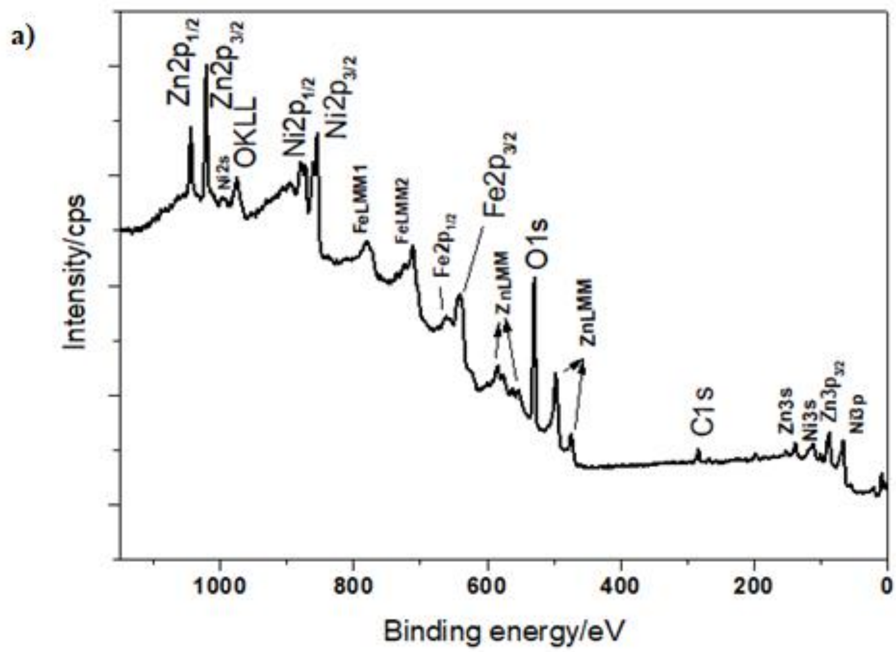

b)

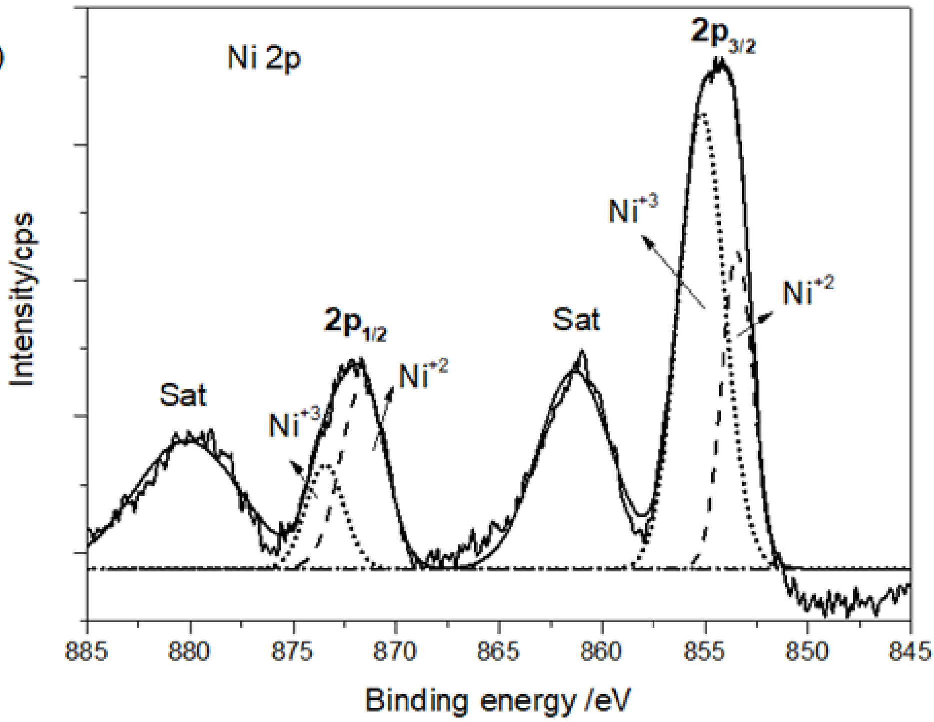

Ni 2p
$2p_{3/2}$
Ni^{+3}
Ni^{+2}
$2p_{1/2}$
Sat
Ni^{+2}
Sat
Ni^{+3}
Intensity/cps
885
880
875
870
865
860
855
850
845
Binding energy /eV

c)

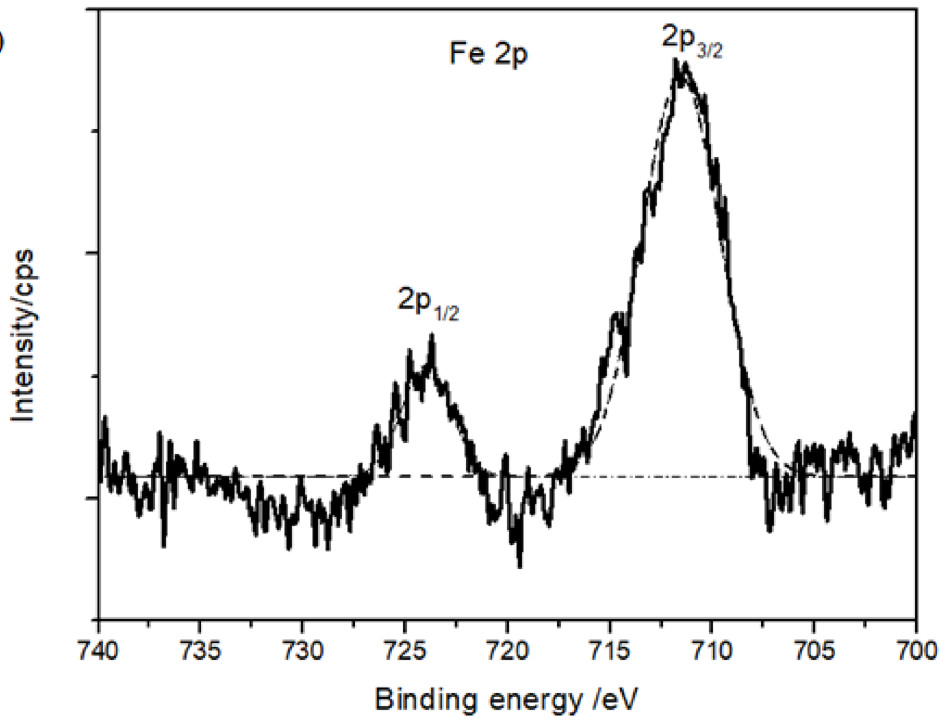

Fe 2p
$2p_{3/2}$
$2p_{1/2}$
Intensity/cps
740
735
730
725
720
715
710
705
700
Binding energy /eV

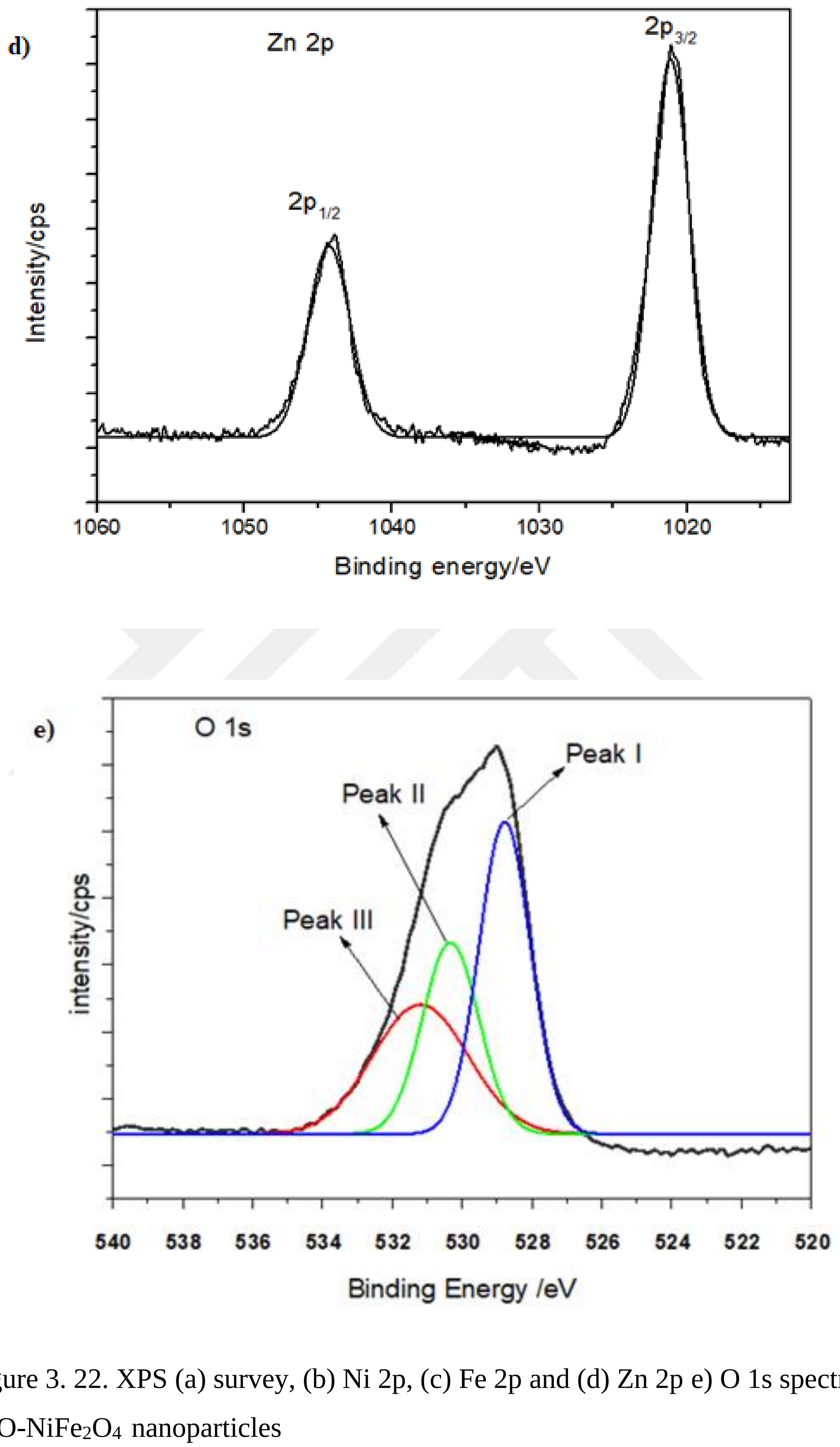

Figure 3. 22. XPS (a) survey, (b) Ni 2p, (c) Fe 2p and (d) Zn 2p e) O 1s spectra of ZnO-$NiFe_2O_4$ nanoparticles

The BET analysis was carried out to determine the pore size and surface area of nanoparticles (Figure 3.23). It was determined that the specific surface area of ZnO-$NiFe_2O_4$ was 40.0 m^2 g^{-1}. The synthesised microspheres were found to have a pore volume of 0.3 cm^3 g^{-1}. Furthermore, ZnO-$NiFe_2O_4$ nanoparticles were found to have an average pore size of 2.3 nm. Water oxidation activity is expected to be significantly affected by this material's large surface area and high porosity.

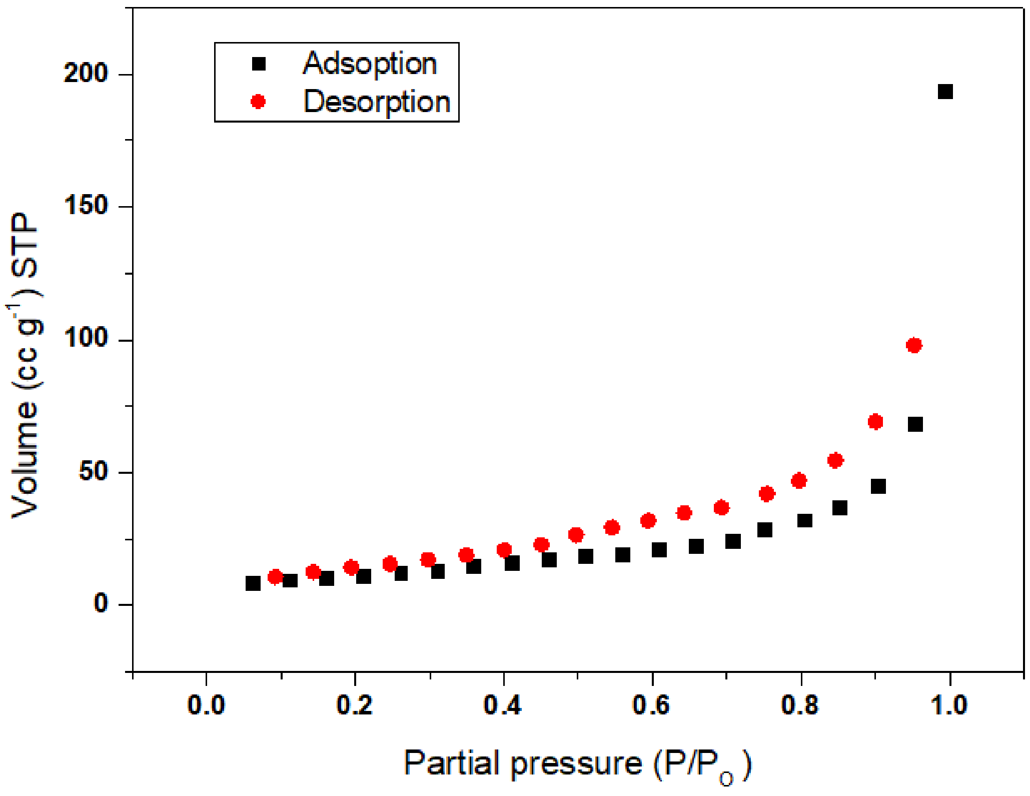

Figure 3. 23. BET isotherm of ZnO-$NiFe_2O_4$

The elemental composition and mass percentage of each component in the material were examined using ICP-OES. Fe, Ni and Zn contents were found to be 16.4± 0.2 weight percent, 35± 1 weight percent and 16.6 ± 0.4 weight percent, respectively. ICP-OES data were used to calculate the mole ratio. The calculated Zn: Ni: Fe mole ratio of 1: 2.4: 1.1 indicates that there may be more Ni present in the synthesized material most likely in the NiO form.

ZnO-$NiFe_2O_4$ nanoparticles were synthesized with two different methods. In the first method which is solvothermal method, Zn has higher weight content, and the nanoparticle shows similar property with ZnO. In contrast, in the second method which is hydrothermal, the synthesized material has higher Ni and Fe contents than Zn.

3.2 ELECTROCATALYTIC ACTIVITY OF NANOPARTICLES

3.2.1 Electrocatalytic Activity of $NiFe_2O_4$, ZnO and ZnO-$NiFe_2O_4$ Nanoparticles

3.2.1.1 $NiFe_2O_4$ Nanoparticles Synthesized with Hydrothermal Method

At room temperature, linear sweep voltammetry (LSV) was applied in alkali medium. To investigate the potential of $NiFe_2O_4$ nanoparticles to function as an electrocatalyst for the oxidation of water. Figure 3.24. (a) shows the polarization curves obtained for GCE coated with nanoparticles and those obtained for bare GCE. It was discovered that the onset potential of $NiFe_2O_4$ nanoparticles was 2.15 V (vs RHE). The obtained value shows poor activity of the catalyst. An additional critical element in evaluating the nanomaterial's electrocatalytic activity is the overpotential required to generate current densities of 10 mA cm^{-2} or higher. $NiFe_2O_4$ nanoparticles can produce current densities of 10 at an overpotential of 1.38 V. Compared to RuO_2, these values are significantly higher (1.49 V vs. RHE and overpotential at 10 mA cm^{-2} is 365 mV).

a)

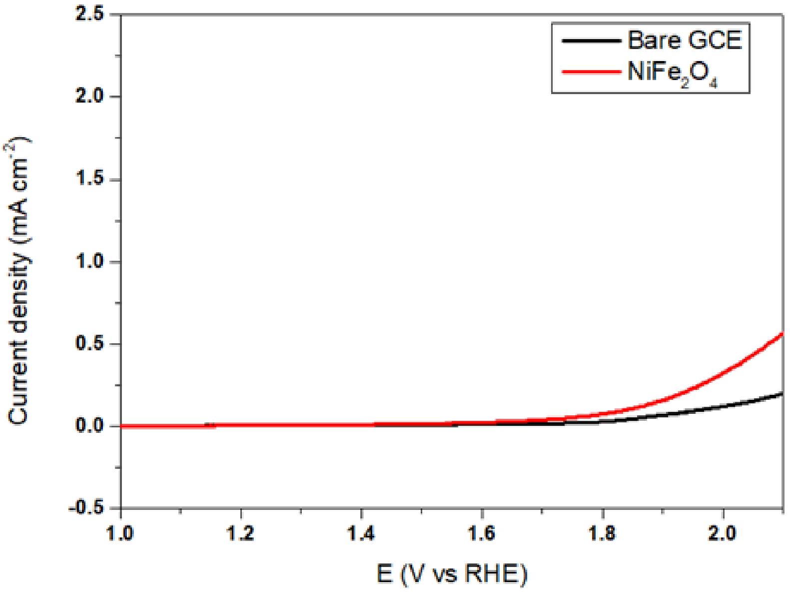

b)

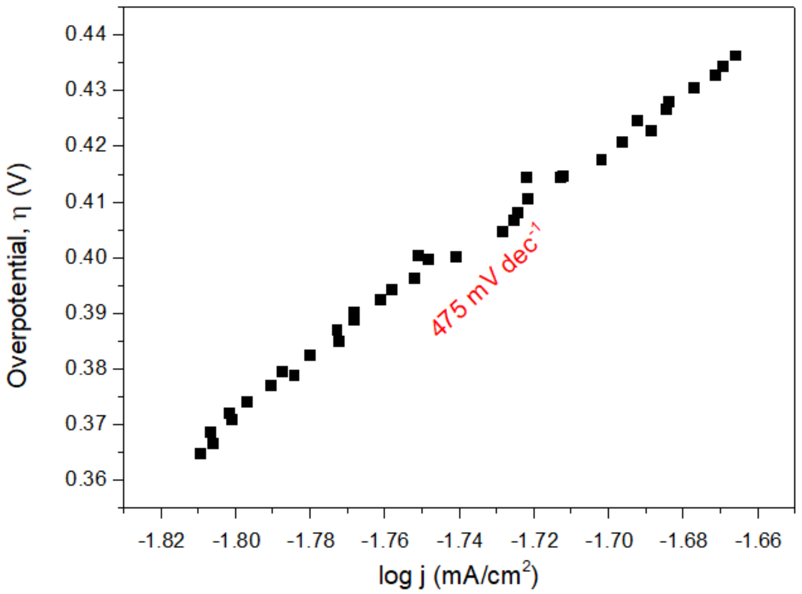

Figure 3. 24. (a) Polarization curves of $NiFe_2O_4$ nanoparticles and bare GCE at 5 mV s^{-1} scan rate in 0.1 M KOH. (b) Tafel plot of $NiFe_2O_4$ nanoparticles.

The Tafel slope, which is calculated by integrating the linear portion of the polarization curve to the Tafel formula, offers crucial details on the catalyst's electrocatalytic activity. Figure 3.24. (b) displays the $NiFe_2O_4$ nanoparticle’s Tafel plot. It was determined that the Tafel slope of $NiFe_2O_4$ nanoparticles is 475 mV dec^{-1}, and it can be considered as quite high compared to RuO_2‘s Tafel slope (117 mV dec^{-1}).

The number of active sites on the surface of nanostructures determines their catalytic activity. Thus, the electrocatalytic activity is also evaluated using ECSA and RF, which are directly connected to the number of active sites. ECSA can be estimated by operating C_{dl}. CVs in the non-Faradaic potential zone are acquired at various scan rates to compute the C_{dl} of $NiFe_2O_4$ nanoparticles (Figure 3.25). The double-layer charging current vs. scan rate plot's slope (at 1.26 V vs. RHE) yields the catalyst's C_{dl} value. $NiFe_2O_4$ nanoparticles have a C_{dl} value of 0.0101 mF and an ECSA of 0.168 cm^2, respectively. Furthermore, 2.405 was discovered to be the RF value.

a)

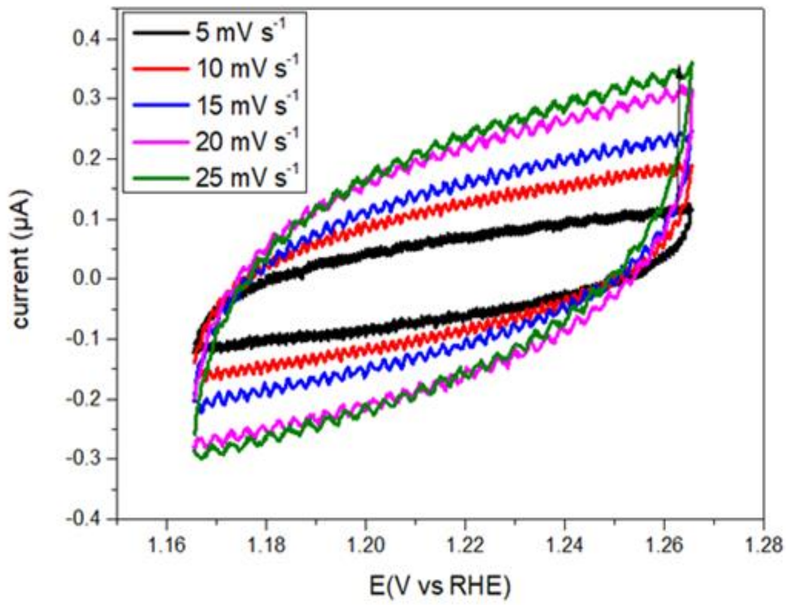

b)

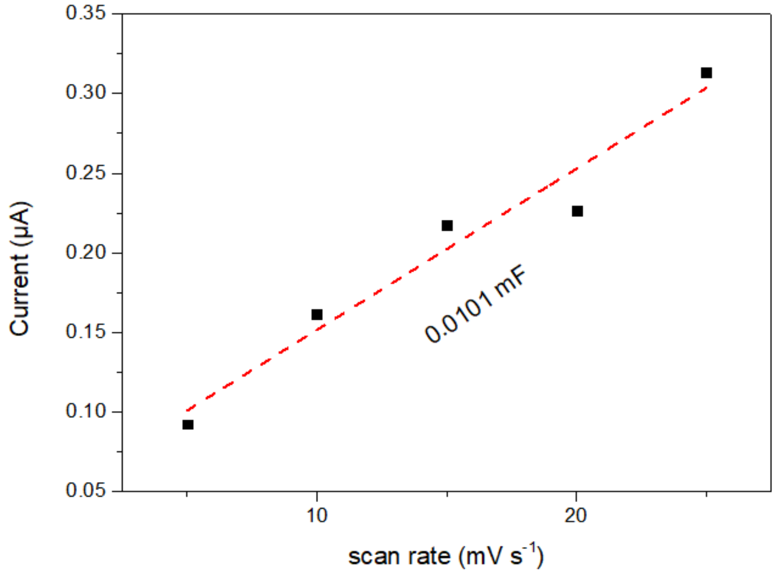

Figure 3. 25. CVs of $NiFe_2O_4$ nanoparticle were recorded at various scan rates (between 5 and 25 mV s^{-1}) in (a) and a graph of current at 1.26 V (vs RHE) vs. scan rate was shown in (b).

3.2.1.2 ZnO Nanoparticles Synthesized with Solvothermal Method

Secondly, the onset potential and overpotential of ZnO nanoparticle was also determined and found as 2.24 V and 1.37 V respectively. Polarization curves for both bare GCE and GCE modified with ZnO are shown in Figure 3.26. (a). The activity of Zn is almost same as bare GCE. The Tafel plot of ZnO nanoparticles are shown in Figure 3.26. (b). ZnO nanoparticles' Tafel slope was found to be 275 mV dec^{-1}.

a)

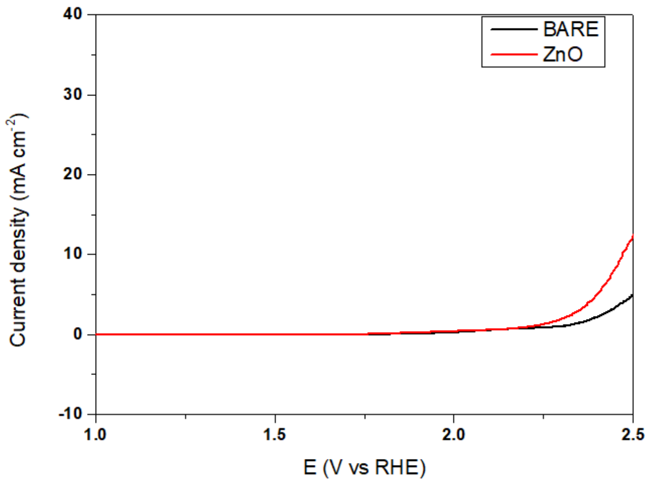

b)

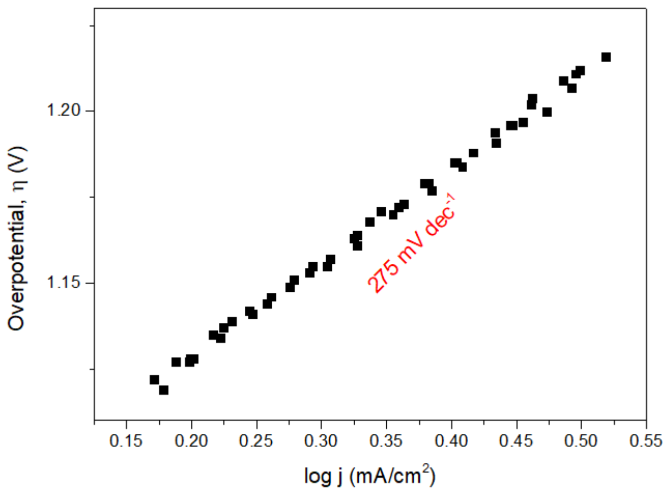

Figure 3. 26. (a) Polarization curves of bare GCE and ZnO nanoparticle and (b) ZnO nanoparticle's Tafel plot.

By calculating C_{dl} values, ECSA was also calculated for the ZnO nanoparticles (Figure 3.27). C_{dl} and ECSA for ZnO were found to be 0.00953 mF and 0.158 cm^2 respectively. Additionally, the RF value was found to be 2.269.

a)

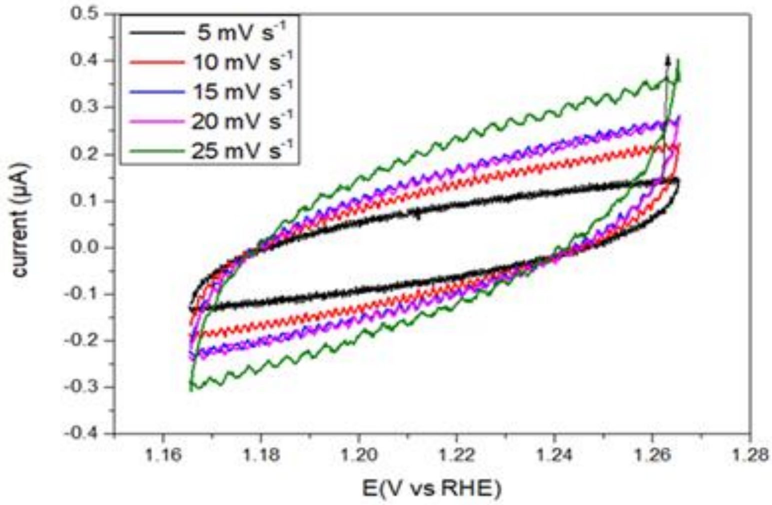

b)

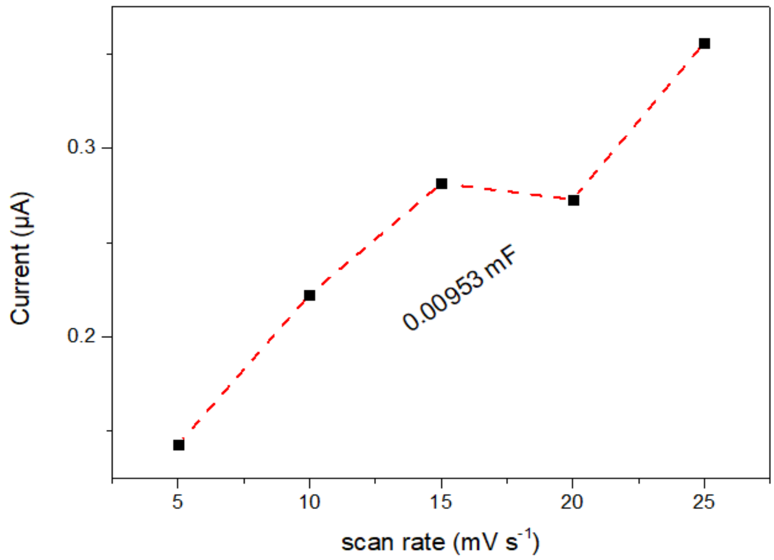

Figure 3. 27. (a) CVs of ZnO nanoparticle at various scan rates (ranging from 5 to 25 mV s^{-1}) and (b) a graph of current at 1.26 V (vs RHE) vs. scan rate.

3.2.1.3 ZnO-$NiFe_2O_4$ Nanoparticles Synthesized with Solvothermal Method

Polarization curves of GCE treated with ZnO-$NiFe_2O_4$ and bare GCE are shown in Figure 3.28. (a). ZnO-$NiFe_2O_4$ was found to have an onset potential of 1.71 V (vs RHE), which is greater than bare electrode. Overpotential is another critical parameter for the catalytic activity and overpotential of ZnO-$NiFe_2O_4$ was found as 775 mV.

a)

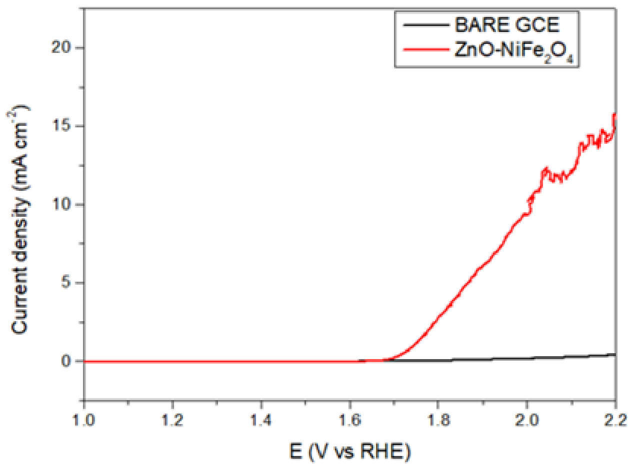

b)

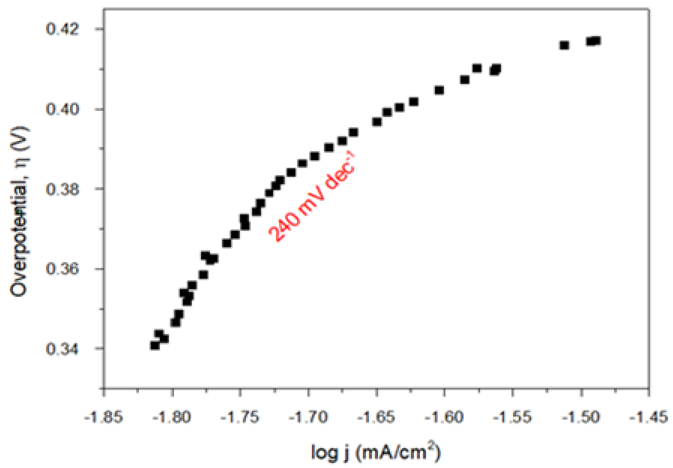

Figure 3. 28. (a) Polarization curves of bare GCE and ZnO-$NiFe_2O_4$ nanoparticles (b) Tafel plot of ZnO-$NiFe_2O_4$ nanoparticles.

The Tafel slope of ZnO-$NiFe_2O_4$ nanoparticles was reported in Figure 3.28. (b) as 240 mV dec^{-1}.

ZnO-$NiFe_2O_4$ nanoparticles' Cdl value and ECSA were found to be 0.0120 mF and 0.2 cm^2, respectively. RF was calculated to be 2.857 by using the ECSA value. In Figure 3.29, recording CVs across the non-Faradaic potential range at different scan rates can be seen.

a)

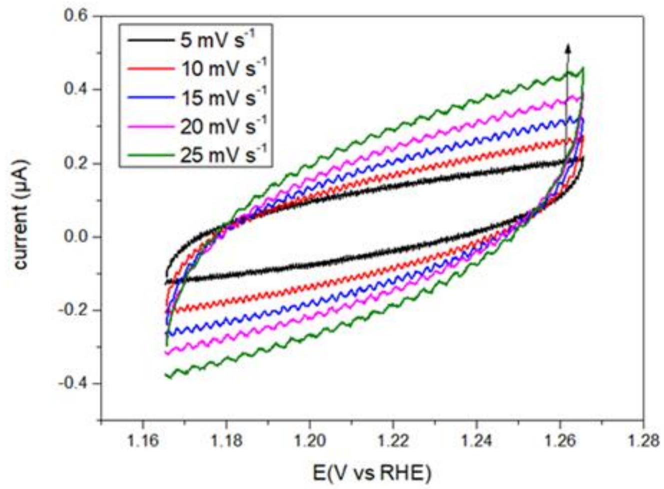

b)

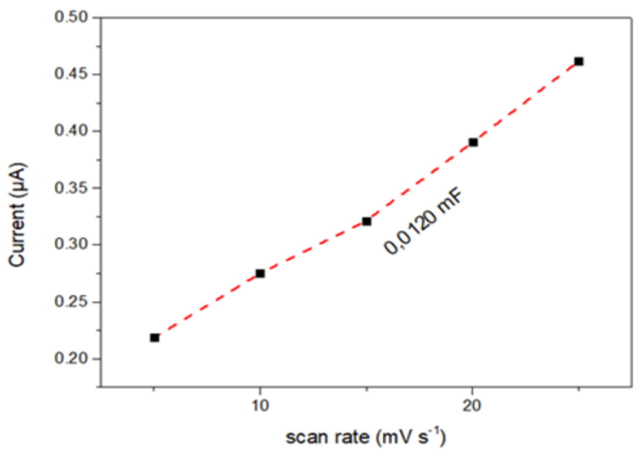

Figure 3. 29. (a) CV of ZnO-$NiFe_2O_4$ nanomaterials obtained at different scan rates (5-10 mV s^{-1}) (b) Plot showing current at 1.26 V (vs RHE) vs scan rate.

In conclusion, electrocatalytic activities of nanoparticles which were synthesized with hydrothermal method were low compared to the RuO_2 which is one of the most active catalysts. In ZnO-$NiFe_2O_4$, it can be due to the high amount of ZnO which is not used for electrocatalytic but for photocatalytic purpose. Figure 3.30. (a) and Figure 3.30. (b) shows polarization curves and Tafel plots of these nanoparticles and RuO_2 respectively.

a)

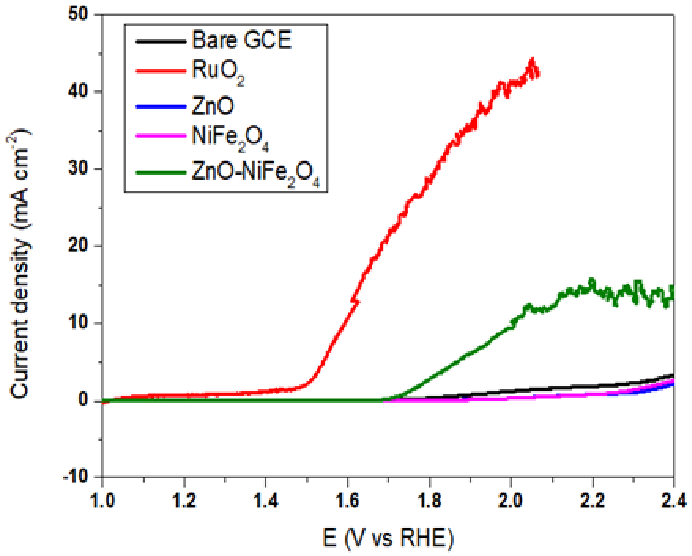

b)

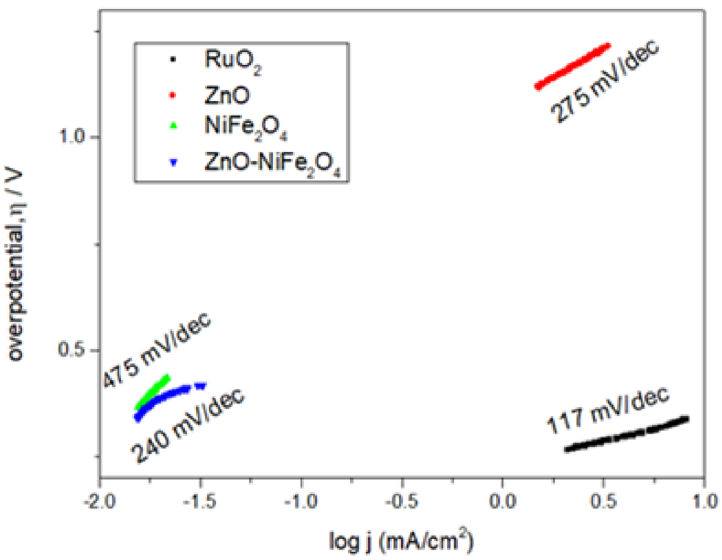

Figure 3. 30. (a) Polarization curves of RuO_2, ZnO, $NiFe_2O_4$ and ZnO-$NiFe_2O_4$ nanoparticles (b) Tafel plots RuO_2, ZnO, $NiFe_2O_4$ and ZnO-$NiFe_2O_4$ nanoparticles.

3.2.1.4 $NiFe_2O_4$ Nanoparticles Synthesized with Hydrothermal Method

LSV has been used in an alkaline media at room temperature to evaluate catalyst' performance. Figure 3.31. (a) displays GCE's polarization curves coated with $NiFe_2O_4$ nanoparticles and those obtained for bare GCE to examine the ability of $NiFe_2O_4$ nanoparticles to work electrocatalytically for the oxidation of water. $NiFe_2O_4$ nanoparticles were found to have an onset potential of 1.62 V (versus RHE). This result is close to or even lower than that of previously reported similar structures, such as NiO / $NiFe_2O_4$ (1.50 V vs RHE)[52] and $NiFe_2O_4$ nanomaterials (1.70 V vs RHE)[53]. Another crucial factor in determining the electrocatalytic activity of the nanomaterial is the overpotential needed to produce current densities of 10 mA cm^2 (or even greater values). At an overpotential of 451 mV, $NiFe_2O_4$ nanoparticles can produce current density of 10. $NiFe_2O_4$ exhibits overpotentials that are equivalent to or even superior to those of previously mentioned catalysts incorporating Ni and/or Fe, like $NiFe_2O_4$ nanoparticles (487 mV)[54], $NiFe_2O_4$ spinel nanoparticles (389 mV)[55].

a)

b)

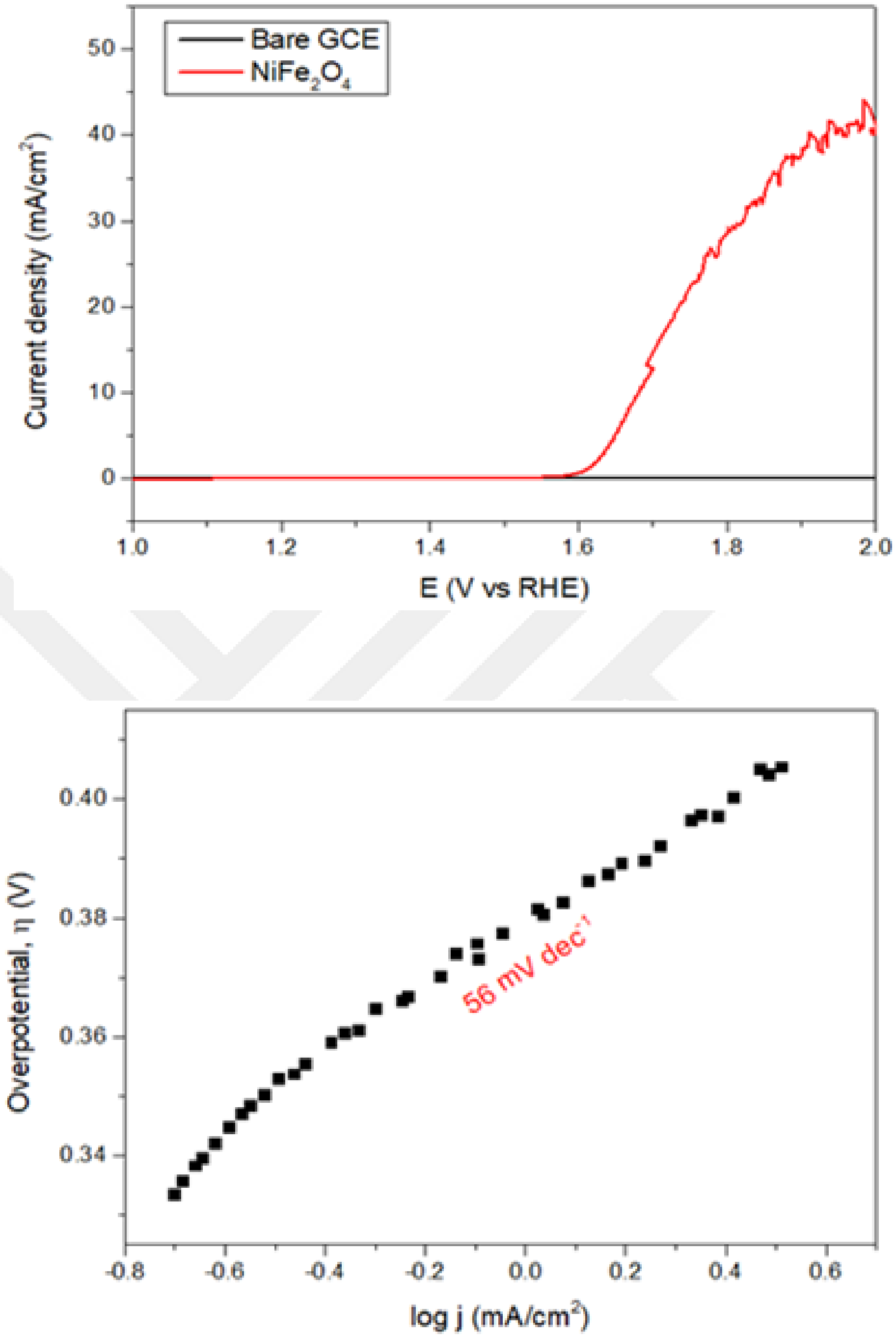

Figure 3. 31. (a) Polarization curves of $NiFe_2O_4$ nanoparticles and bare GCE at 5 mV s^{-1} scan rate in 0.1 M KOH. (b) Tafel plot of $NiFe_2O_4$ nanoparticle.

The Tafel slope, which is calculated by integrating the linear portion of the polarisation curve to the Tafel formula, offers crucial details on the catalyst's electrocatalytic activity. Figure 3.31. (b) displays the $NiFe_2O_4$ nanoparticle Tafel plot. It was determined that the Tafel slope of $NiFe_2O_4$ nanoparticle is 56 mV dec^{-1}, which is comparable to or even lower than those with similar structures, such as $NiFe_2O_4$ nanoparticles (63 mV dec^{-1})[54] , $NiFe_2O_4$ nanosheets (49 mV dec^{-1}).[56]

a)

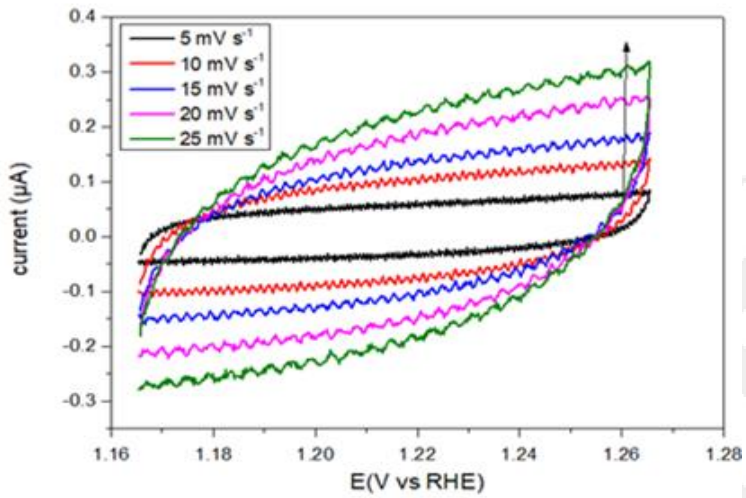

b)

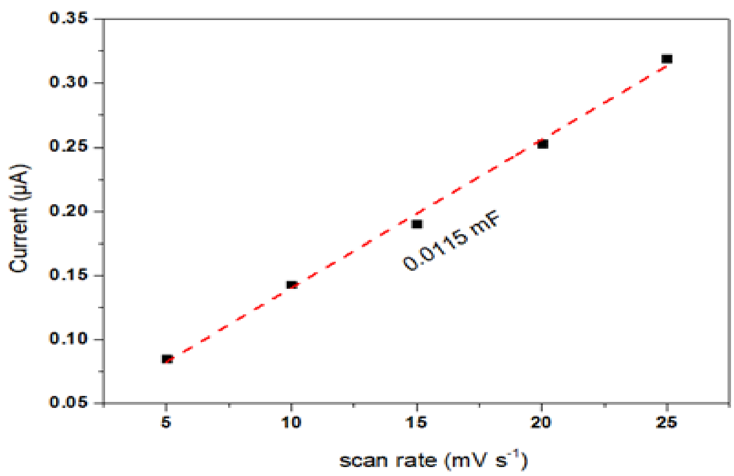

Figure 3. 32. CVs of $NiFe_2O_4$ nanoparticle were recorded at various scan rates between 5 and 25 mV s^{-1} in (a) and a graph of current at 1.26 V (vs RHE) vs. scan rate was shown in (b).

Catalytic activity depends on the quantity of active sites on the surface of nanostructures. Therefore, ECSA and RF, that are directly correlated to the number of active sites, are also used to assess the electrocatalytic activity. C_{dl} may be operated to estimate ECSA. To calculate the C_{dl} of $NiFe_2O_4$ nanoparticles, CVs in the non-Faradaic potential region are taken at different scan rates (Figure 3.32). The C_{dl} value of the catalyst is determined by the double-layer charging current vs scan rate plot's slope (at 1.26 V vs RHE). The C_{dl} value and ECSA of $NiFe_2O_4$ nanoparticles are 0.0115 mF and 0.192 cm^2, respectively. Additionally, RF value was found to be 2.743.

3.2.1.5 ZnO Nanoparticles Synthesized with Sol-gel Method

Polarization curves for both bare GCE and GCE treated with ZnO are shown in Figure 3.33. (a). For ZnO nanoparticles, an onset potential of 2.25 V (vs RHE) was observed.

The essential overpotential for producing current density of 10 mA cm^{-2} is a key component of electrochemical activity. Because of overpotential of 1.29 V, ZnO nanoparticles may achieve current densities of 10 mA cm^{-2}.

a)

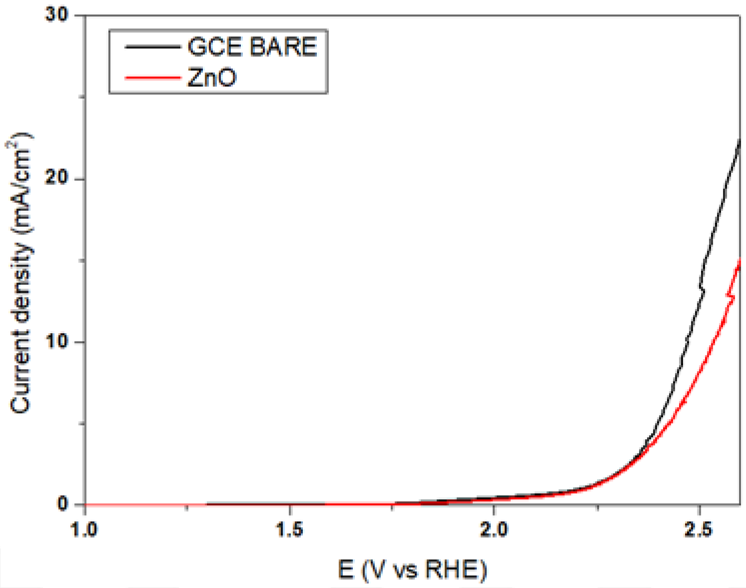

b)

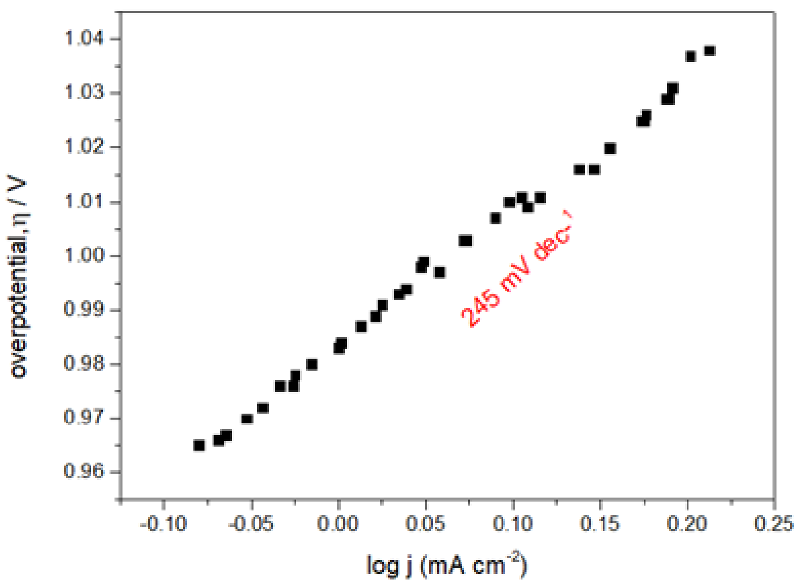

Figure 3. 33. (a) Polarization curves of bare GCE and ZnO nanoparticle and (b) ZnO nanoparticle's Tafel plot.

The Tafel plot of ZnO nanoparticles are shown in Figure 3.33. (b). ZnO nanoparticles' tafel slope was found to be 245 $mVdec^{-1}$.

To find the C_{dl} of ZnO nanoparticles, CVs in the non-Faradaic potential range are measured at scan rates from 5 to 25 mV/s (Figure 3.34). The C_{dl} value of the catalyst is determined by the slope of the double-layer charging current vs scan rate plot (at 1.26 V vs RHE). ZnO nanoparticles have an ECSA of 0.217 cm^2 and C_{dl} value of 0.0130 mF. Additionally, RF value was found to be 3.1.

a)

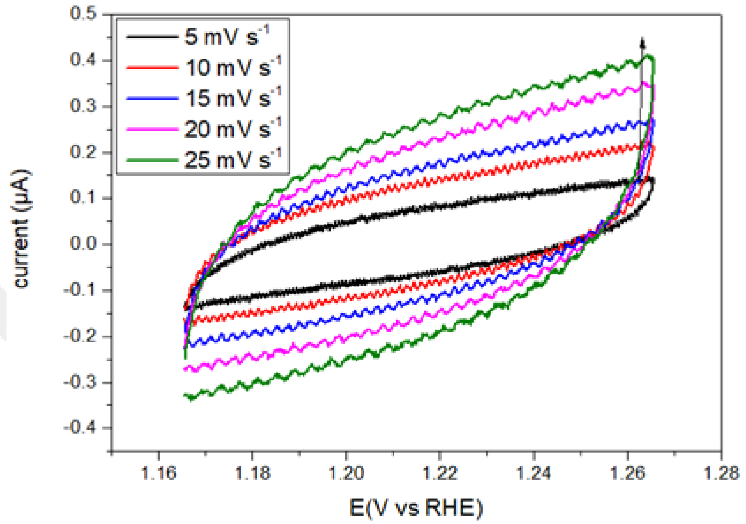

b)

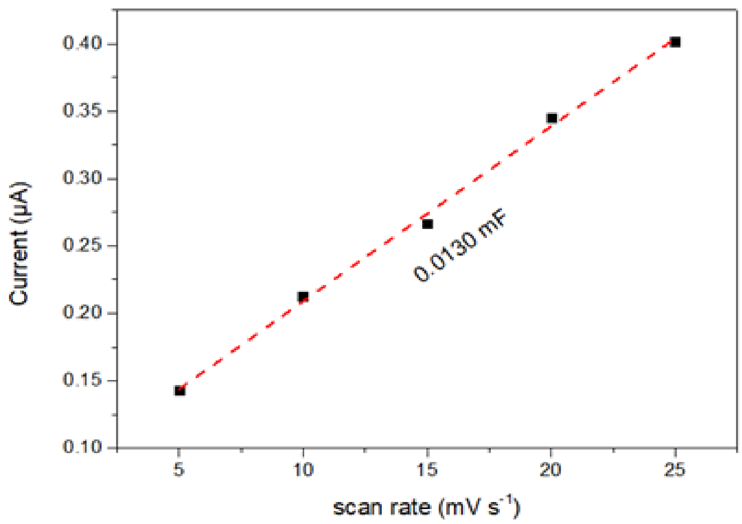

Figure 3. 34. (a) CVs of ZnO nanoparticle at various scan rates (ranging from 5 to 25 mV s^{-1}) and (b) a graph of current at 1.26 V (vs RHE) vs. scan rate.

3.2.1.6 ZnO -$NiFe_2O_4$ Nanoparticles Synthesized with Hydrothermal Method

Polarization curves of GCE treated with ZnO-$NiFe_2O_4$ and bare GCE are shown in Figure 3.35. (a). ZnO-$NiFe_2O_4$ was found to have an onset potential of 1.63 V (vs RHE), which is extensively greater than bare electrode. The overpotential required to generate current densities of 10 mA cm^{-2} or higher values is a key component in defining the electrocatalytic activity of the nanomaterial. ZnO-$NiFe_2O_4$ nanomaterials may achieve a current density of 10 mA cm^{-2} with an overpotential of 450 mV.

a)

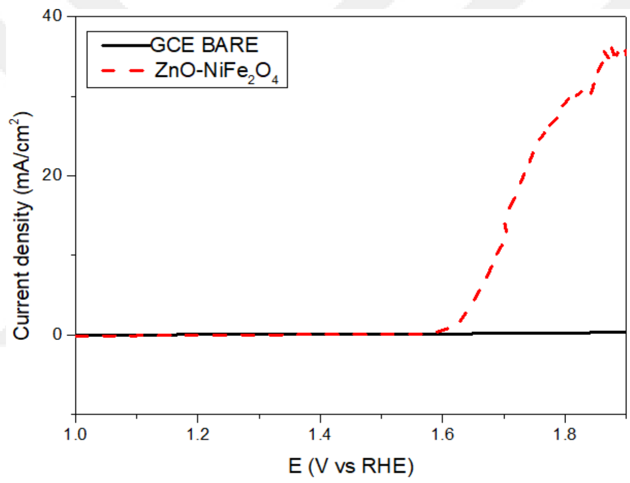

b)

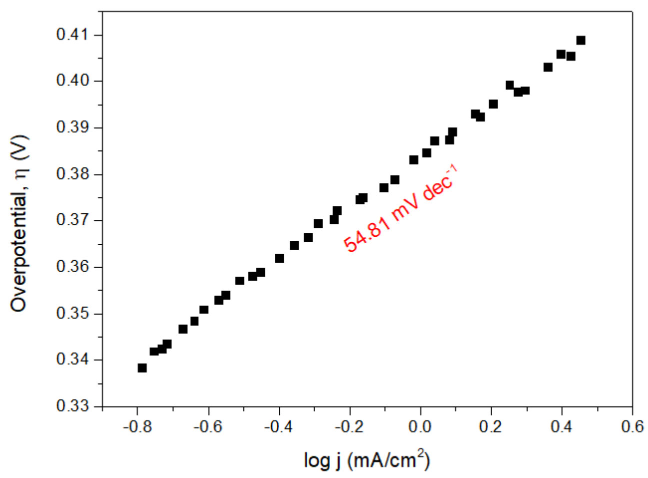

Figure 3. 35. (a) Polarization curves of bare GCE and ZnO-$NiFe_2O_4$ nanoparticles (b) Tafel plot of ZnO-$NiFe_2O_4$ nanoparticles.

Tafel slope provides crucial details regarding the catalytic activity of the product. The smaller slope denotes a catalyst's better performance. The Tafel slope of ZnO-$NiFe_2O_4$ nanoparticles was reported in Figure 3.35. (b) as 54.81 mV dec^{-1} which indicate that the synthesized material has very promising OER kinetics.

As shown in Figure 3.36, recording CVs across the non-Faradaic potential range at different scan rates can be used to calculate the C_{dl} value. The C_{dl} value of the catalyst is obtained from the slope of the double layer charging current density vs scan rate plot (at 1.26 V versus RHE). Using this method, the C_{dl} value and ECSA of ZnO-$NiFe_2O_4$ nanoparticles were determined to be 0.0427 mF and 0.712 cm^2, respectively. Using the ECSA value, RF was determined to be 10.17. Moreover, ZnO-$NiFe_2O_4$ nanoparticles were found to have a mass activity of 25 A g^{-1} and a specific activity of 0.063 mA $cm^{-2}{}_{ECSA}$ at an overpotential of 799 mV, accordingly. These values have been determined for RuO_2 as 0.237 mA $cm^{-2}{}_{ECSA}$ specific activity and 170 A g^{-1} mass activity.

The mass and specific activities of ZnO-$NiFe_2O_4$ nanoparticles are comparable to those of RuO_2, indicating the nanoparticles' outstanding potential as an electrocatalyst.

a)

b)

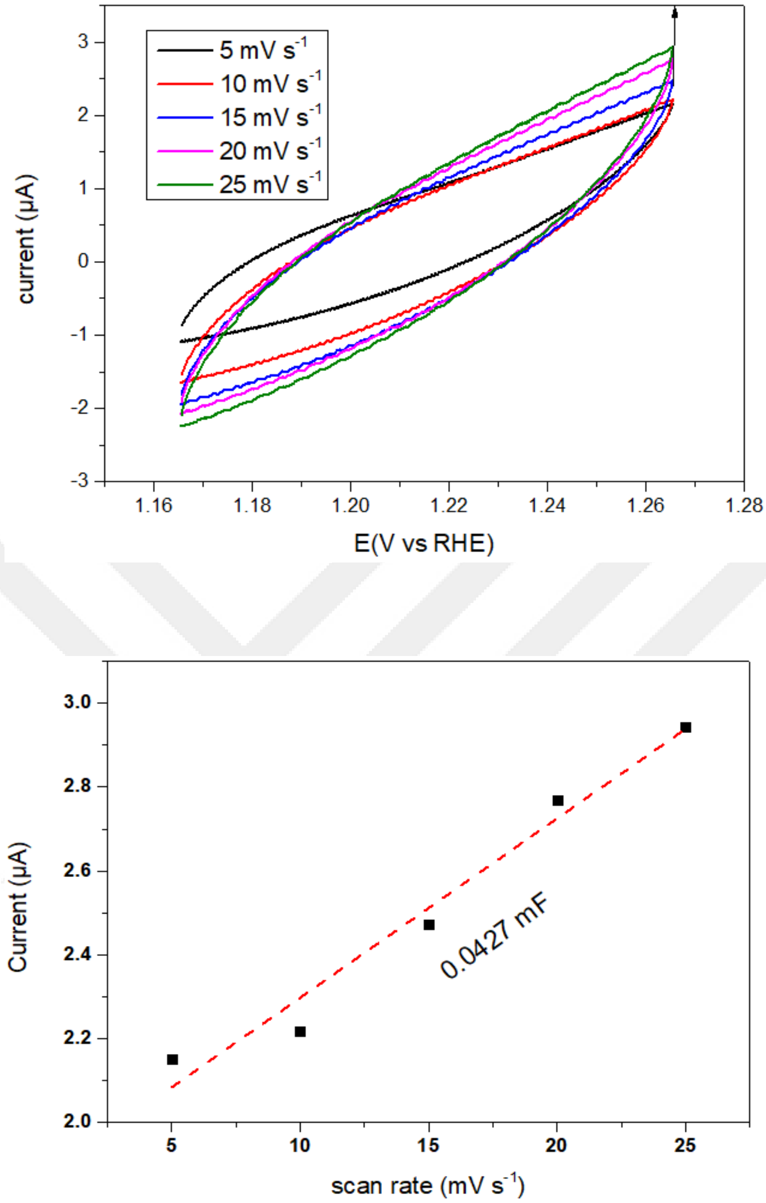

Figure 3. 36. (a) CV of ZnO-$NiFe_2O_4$ nanomaterials obtained at different scan rates (5-10 mV s^{-1}) (b) Plot showing current at 1.26 V (vs RHE) vs scan rate.

ZnO-$NiFe_2O_4$ nanoparticles which were synthesized by hydrothermal method show good electrocatalytic activity compared to previously synthesized materials. In Figure 3.37, polarization curves and Tafel slopes of synthesized nanoparticles are shown.

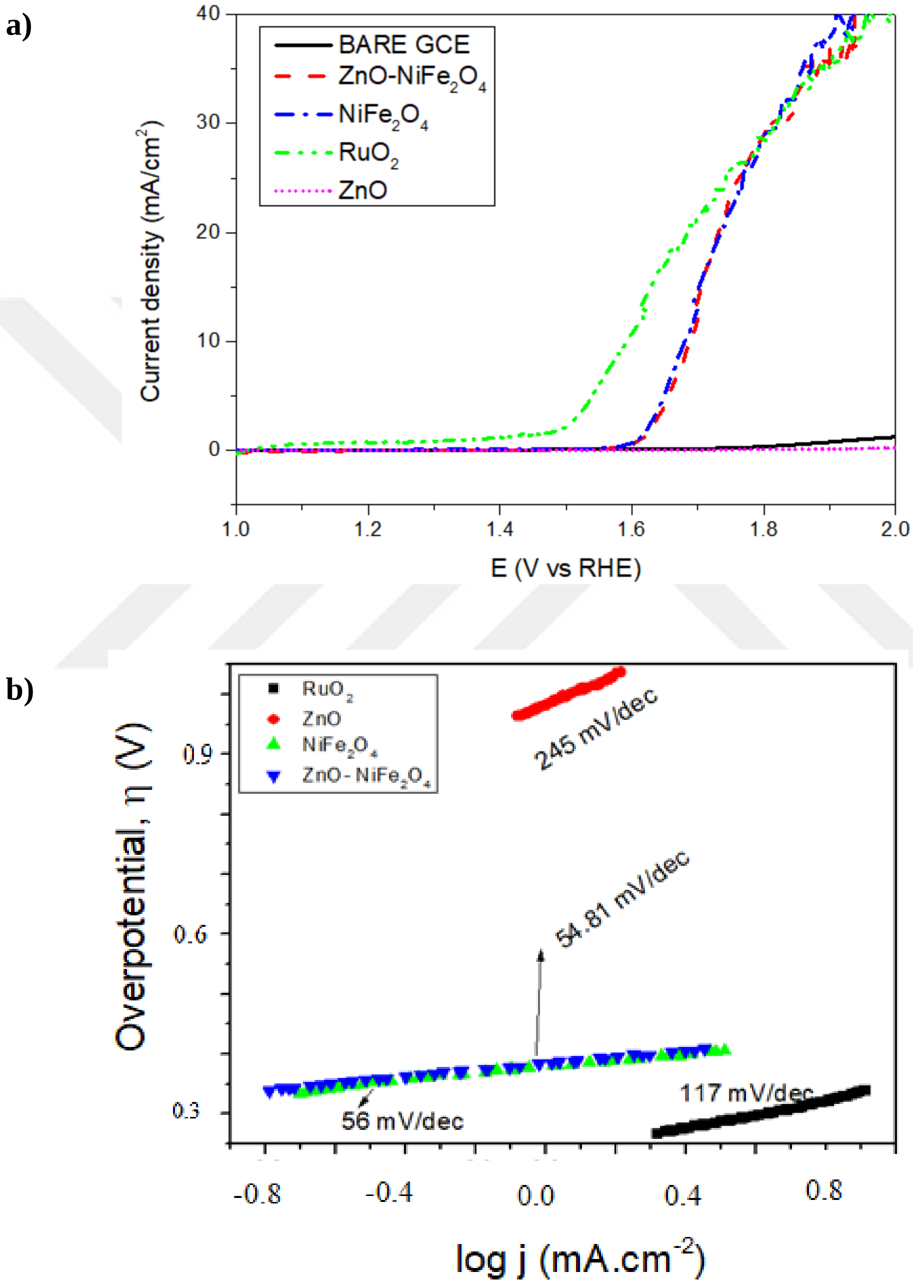

Figure 3. 37. (a) Polarization curves of RuO_2, ZnO, $NiFe_2O_4$ and ZnO-$NiFe_2O_4$ nanoparticles (b) Tafel plots of RuO_2, ZnO, $NiFe_2O_4$ and ZnO-$NiFe_2O_4$ nanoparticles

Different methods have been proposed to explain the water oxidation reaction in the presence of a catalyst. The mechanism of a reaction that occurs in a basic media is described as follows. M denotes an active metal surface where species like O_2, -OH, and -OOH adsorb.[9]

$M + OH^- \rightarrow M — OH + e^-$

$M — OH + OH^- \rightarrow M — O * + H_2O + e^-$

$M — O * + OH^- \rightarrow M — OOH + e^-$

$M — OOH + OH^- \rightarrow M — O_2 + e^- + H_2O$

$M — O_2 \rightarrow M + O_2$

Firstly, OH^- absorbs on the surface of the active metal site. In the next step, M-OH and OH^- interact with each other to release H_2O and an electron. The interaction between adsorbed atomic O* (M — O *) and OH^- results in the formation M— OOH form. Moreover, additional OH^- anions cause adsorbed O_2 and H_2O to form. The adsorbed O_2 is released at the last stage of the process.

Table 3. 1.A review of a few of the most notable and recent electrocatalysts for the OER in an alkaline media and the summary of water oxidation properties of all synthesized nanoparticles with different methods.

	Onset (RHE)	η10	Tafel (mV/dec)	Medium	Ref
ZnO (Solvothermal method)	2.24	1.37 V	275	0.1 M KOH	This work
ZnO (Sol-gel method)	2.25	1.29 V	245	0.1 M KOH	This work
$NiFe_2O_4$ (Hydrothermal method)	2.15	1.38 V	475	0.1 M KOH	This work
U-$NiFe_2O_4$ (Hydrothermal method)	1.62	451 mV	56	0.1 M KOH	This work
ZnO-$NiFe_2O_4$ (Solvothermal method)	1.71	775 mV	240	0.1 M KOH	This work
ZnO-$NiFe_2O_4$ (Hydrothermal method)	1.63	450 mV	54.81	0.1 M KOH	This work
RuO_2	1.49	365 mV	117	0.1 M KOH	This work
NiO/Ni/C	-	257 mV	-	1 M KOH	[57]
Fe_2O_3/ FeS	1.49 V	370 mV	90	1 M KOH	[58]
NiO/NiFe2O4 nanorods	-	302 mV	42	1 M KOH	[59]

U-$NiFe_2O_4$: nanoparticle which was obtained by hydrothermal method using urea as surfactant

Table 3.1. shows the electrocatalytic performances of all synthesized nanoparticles in this study. Among these substances, the highest activity after RuO_2 was obtained with $ZnO-NiFe_2O_4$ nanoparticle which was synthesized with hydrothermal method. It has lowest onset potential, overpotential and Tafel slope. These are desired for the efficient electrocatalyst. $NiFe_2O_4$ nanoparticles also show almost same results with the $ZnO-NiFe_2O_4$ nanoparticles. The most likely and expected reason for this observation is the presence of ZnO with low conductivity in the synthesized material. As previously noted, the main goal of synthesizing a hybrid material with ZnO is to integrate a component with potential photocatalytic activity. The results obtained in this study suggest that the synthesized hybrid nanomaterial has the potential to be an effective electrode material for photochemical processes in the future.

CHAPTER 4

CONCLUSIONS

The goal of this thesis was to develop and synthesize new catalyst systems by using abundant transition metals for splitting water photochemically. In the scope of this thesis study, ZnO-$NiFe_2O_4$ hybrid nanomaterial that might be employed as catalyst in both the electrochemical and photochemical water oxidation reaction was synthesized. Analytical methods such as SEM, EDX, XRD, XPS, ICP-OES, and BET were used to characterize the synthesized materials. Then, using electrochemical techniques, their activities were examined for the water oxidation reaction.

ZnO component of the hybrid material was synthesized both by sol-gel and solvothermal methods separately to compare with hybrid material and these synthesized nanoparticles participate in the formation of hybrid nanomaterials. In both methods yielded ZnO nanoparticles with high purity and crystallinity as verified by XRD analysis. Hydrothermal method was used to synthesize $NiFe_2O_4$ nanoparticles. XRD analysis of the $NiFe_2O_4$ nanomaterials suggest the formation of NiO along with the $NiFe_2O_4$. This observation agree well with the previous reports in the literature.

ZnO-$NiFe_2O_4$ hybrid materials were synthesized by following two different routes. In first one, pre-synthesized ZnO with sol-gel was allowed to react with Ni and Fe precursors in the hydrothermal medium to obtain the target material. In the second route, this time pre-synthesized $NiFe_2O_4$ nanoparticles were mixed with the Zn precursor, and solvothermal method was followed to prepare ZnO-$NiFe_2O_4$ hybrid material.

The XRD pattern of the hybrid material which was synthesized via first route was matched mostly with $NiFe_2O_4$ nanoparticles. This is most likely because of the formation of $NiFe_2O_4$ layer on ZnO nanomaterials inhibiting the presence of ZnO peaks clearly. In contrast to the first route, only ZnO peaks were observed in the XRD pattern of the hybrid material prepared by following the second route. This observation suggest that ZnO layer was formed on the $NiFe_2O_4$ nanomaterial in core-shell type structure and thus $NiFe_2O_4$ peaks are not detectable in the XRD pattern. To verify the formation of core-shell type of structure detailed TEM along with EDX analyses are needed to be performed.

The electrochemical performance of the synthesized materials was investigated for water oxidation reaction in alkaline medium (0.1 M KOH). The findings showed that both ZnO nanoparticles which were synthesized in two different methods have a very high onset (2.24 V and 2.25 V vs RHE) and overpotential values in the water oxidation reaction, exhibiting essentially negligible activity. The onset potentials of U-$NiFe_2O_4$, $NiFe_2O_4$, ZnO-$NiFe_2O_4$ (synthesized by solvothermal method (route 2)) and ZnO-$NiFe_2O_4$ (synthesized by hydrothermal method (route1)) are (1.62 V vs RHE), (2.15 V vs RHE), (1.71 V vs RHE) and (1.63 V vs RHE), respectively. Low onset potential and overpotential values indicate high electrochemical activiy. The results reveal that ZnO-$NiFe_2O_4$ synthesized by hydrothermal method (route 1) has lower overpotential, thus better electrochemical activity than the hybrid material synthesized by solvothermal method (route 2). Furthermore, ZnO-$NiFe_2O_4$ (synthesized by hydrothermal method) hybrid nanomaterial has the lowest tafel slope (54.81 mv/dec) suggesting good water oxidation kinetics for this material.

Cyclic voltammetry was also used to analyze electrochemical activities of nanoparticles. ECSA, C_{dl} and RF can be obtained by taking cyclic voltammogram within non-Faradaic potential region at different scan rates. The active site which is present on the nanomaterial's surface is directly proportional to these parameters. Increased ECSA, C_{dl} and RF shows larger active surface area of catalyst and it is the sign of the improved catalytic performance. Among the synthesized nanomaterials, ZnO-$NiFe_2O_4$ (synthesized by hydrothermal method) has the largest ECSA (0.712 cm^2), C_{dl} (0.0427 mF) and RF (10.17) values and this indicates that the synthesized hybrid nanomaterial has the highest potential for being an active catalyst.

In conclusion, this work presents synthesis of new hybrid material by following two different approaches. Based on the electrochemical findings, the nanomaterials synthesized in this study are believed to make contributions to the family of photocatalysts that can be used for splitting water.

REFERENCES

(1) He, G.; Wen, Y.; Ma, C.; Li, X.; Gao, L.; Sun, Z. Photocatalytic Hydrogen Evolution of Nanoporous CoFe2O4 and NiFe2O4 for Water Splitting. *Int J Hydrogen Energy* **2021**, *46* (7), 5369–5377. https://doi.org/10.1016/j.ijhydene.2020.11.107.

(2) Liu, X.; Cui, S.; Sun, Z.; Du, P. Copper Oxide Nanomaterials Synthesized from Simple Copper Salts as Active Catalysts for Electrocatalytic Water Oxidation. *Electrochim Acta* **2015**, *160*, 202–208. https://doi.org/10.1016/j.electacta.2015.01.123.

(3) Tahir, M.; Pan, L.; Idrees, F.; Zhang, X.; Wang, L.; Zou, J.-J.; Wang, Z. L. Electrocatalytic Oxygen Evolution Reaction for Energy Conversion and Storage: A Comprehensive Review. *Nano Energy* **2017**, *37*, 136–157. https://doi.org/10.1016/j.nanoen.2017.05.022.

(4) Shinde, P. V.; Mane, P.; Chakraborty, B.; Sekhar Rout, C. Spinel NiFe2O4 Nanoparticles Decorated 2D Ti3C2 MXene Sheets for Efficient Water Splitting: Experiments and Theories. *J Colloid Interface Sci* **2021**, *602*, 232–241. https://doi.org/10.1016/j.jcis.2021.06.007.

(5) Liu, J.; Nan, Y.; Chang, X.; Li, X.; Fang, Y.; Liu, Y.; Tang, Y.; Wang, X.; Li, R.; Ma, J. Hierarchical Nitrogen-Enriched Porous Carbon Materials Derived from Schiff-Base Networks Supported FeCo2O4 Nanoparticles for Efficient Water Oxidation. *Int J Hydrogen Energy* **2017**, *42* (16), 10802–10812. https://doi.org/10.1016/j.ijhydene.2017.03.100.

(6) Devadas, A.; Baranton, S.; Coutanceau, C. Green Synthesis and Modification of RuO2 Materials for the Oxygen Evolution Reaction. *Front Energy Res* **2020**, *8*. https://doi.org/10.3389/fenrg.2020.571704.

(7) Sharma, G.; Kumar, A.; Sharma, S.; Naushad, M.; Prakash Dwivedi, R.; ALOthman, Z. A.; Mola, G. T. Novel Development of Nanoparticles to Bimetallic Nanoparticles and Their Composites: A Review. *J King Saud Univ Sci* **2019**, *31* (2), 257–269. https://doi.org/10.1016/j.jksus.2017.06.012.

(8) Ekebas, E.; Cetin, A.; Önal, A. M.; Nalbant Esenturk, E. Magnesium Substituted Cobalt Spinel Nanostructures for Electrocatalytic Water Oxidation. *J Appl Electrochem* **2019**, *49* (3), 315–325. https://doi.org/10.1007/s10800-018-01285-9.

(9) Zhao, Q.; Yan, Z.; Chen, C.; Chen, J. Spinels: Controlled Preparation, Oxygen Reduction/Evolution Reaction Application, and Beyond. *Chem Rev* **2017**, *117* (15), 10121–10211. https://doi.org/10.1021/acs.chemrev.7b00051.

(10) Osgood, H.; Devaguptapu, S. V.; Xu, H.; Cho, J.; Wu, G. Transition Metal (Fe, Co, Ni, and Mn) Oxides for Oxygen Reduction and Evolution Bifunctional Catalysts in Alkaline Media. *Nano Today*. Elsevier B.V. October 1, **2016**, pp 601–625. https://doi.org/10.1016/j.nantod.2016.09.001.

(11) He, G.; Wen, Y.; Ma, C.; Li, X.; Gao, L.; Sun, Z. Photocatalytic Hydrogen Evolution of Nanoporous CoFe2O4 and NiFe2O4 for Water Splitting. *Int J Hydrogen Energy* **2021**, *46* (7), 5369–5377. https://doi.org/10.1016/j.ijhydene.2020.11.107.

(12) Lim, D.; Kong, H.; Kim, N.; Lim, C.; Ahn, W. S.; Baeck, S. H. Oxygen-Deficient NiFe2O4 Spinel Nanoparticles as an Enhanced Electrocatalyst for the Oxygen Evolution Reaction. *ChemNanoMat* **2019**, *5* (10), 1296–1302. https://doi.org/10.1002/cnma.201900231.

(13) Yuan, F.; Cheng, X.; Wang, M.; Ni, Y. Controlled Synthesis of Tubular Ferrite MFe2O4 (M = Fe, Co, Ni) Microstructures with Efficiently Electrocatalytic Activity for Water Splitting. *Electrochim Acta* **2019**, *324*. https://doi.org/10.1016/j.electacta.**2019**.134883.

(14) Liu, G.; Wang, K.; Gao, X.; He, D.; Li, J. Fabrication of Mesoporous NiFe2O4 Nanorods as Efficient Oxygen Evolution Catalyst for Water Splitting. *Electrochim Acta* **2016**, *211*, 871–878. https://doi.org/10.1016/j.electacta.2016.06.113.

(15) Srivastava, M.; Chaubey, S.; Ojha, A. K. Investigation on Size Dependent Structural and Magnetic Behavior of Nickel Ferrite Nanoparticles Prepared by Sol-Gel and Hydrothermal Methods. *Mater Chem Phys* **2009**, *118* (1), 174–180. https://doi.org/10.1016/j.matchemphys.2009.07.023.

(16) Liu, G.; Wang, K.; Gao, X.; He, D.; Li, J. Fabrication of Mesoporous NiFe2O4 Nanorods as Efficient Oxygen Evolution Catalyst for Water Splitting. *Electrochim Acta* **2016**, *211*, 871–878. https://doi.org/10.1016/j.electacta.2016.06.113.

(17) Zhu, H. Y.; Jiang, R.; Fu, Y. Q.; Li, R. R.; Yao, J.; Jiang, S. T. Novel Multifunctional NiFe 2 O 4 /ZnO Hybrids for Dye Removal by Adsorption, Photocatalysis and Magnetic Separation. *Appl Surf Sci* **2016**, *369*, 1–10. https://doi.org/10.1016/j.apsusc.2016.02.025.

(18) Rahmayeni; Zulhadjri; Jamarun, N.; Emriadi; Arief, S. Synthesis of ZnO-NiFe2O4 Magnetic Nanocomposites by Simple Solvothermal Method for Photocatalytic Dye Degradation under Solar Light. *Oriental Journal of Chemistry* **2016**, *32* (3), 1411–1419. https://doi.org/10.13005/ojc/320315.

(19) Ashrit, P. Introduction to Transition Metal Oxides and Thin Films. In Transition Metal Oxide Thin Film Based Chromogenics and Devices; Elsevier, **2017**; Pp 13–72. Https://Doi.Org/10.1016/B978-0-08-101747- 0.00002-7.

(20) Kung, H. H. Chapter 2 Bulk and Surface Structure of Transition Metal Oxide. In Transition Metal Oxides: Surface Chemistry and Catalysis; **1989**; Pp 6–26. https://doi.Org/10.1016/S0167-2991(08)60925-8.

(21) Mete, E. Electronic Properties of Transition Metal Oxides a Thesis Submitted to the Gradutae School of Natural and Applied Sciences of The Middle East Technical University; **2003.**

(22) Cox, P. A. *Transition Metal Oxides: An Introduction to Their Electronic Structure and Properties*.

(23) Qin, B.; Qi, J. Structure and Basic Properties of Transition Metal Oxides Designed for Application in Water Splitting. In *Metal Oxides and Related Solids for Electrocatalytic Water Splitting*; Elsevier, **2022**; pp 131–160. https://doi.org/10.1016/B978-0-323-85735-2.00007-1.

(24) Habibi, M. H.; Fakhri, F. Low Temperature Preparation, Characterization, Magnetic Measurements, Thermal, Optical, Morphological and Photo-Catalytic Properties of Nano-Size Single Phase Nickel Ferrite NiFe2O4. *Journal of Materials Science: Materials in Electronics* **2017**, *28* (18), 13455–13463. https://doi.org/10.1007/s10854-017-7184-z.

(25) Patıl, N.; Bhaskar, R.; Vyavhare, V.; Dhadge, R.; Khaıre, V.; Patıl, Y. Overview on Methods of Synhesis of Nanoparticle. *Int J Curr Pharm Res* **2021**, 11–16.

(26) Niederberger, M.; Pinna, N. *Metal Oxide Nanoparticles in Organic Solvents Synthesis, Formation, Assembly and Application ^Spri Ringer*.

(27) Guo, T.; Yao, M. S.; Lin, Y. H.; Nan, C. W. A Comprehensive Review on Synthesis Methods for Transition-Metal Oxide Nanostructures. *CrystEngComm* **2015**, *17* (19), 3551–3585. https://doi.org/10.1039/c5ce00034c.

(28) Polshettiwar, V. , A. T. *Nanocatalysis Synthesis and Applications*; John Wiley & Sons, Inc.: Hoboken, NJ, USA, **2023**.

(29) Loiha, S.; Föttinger, K.; Zorn, K.; Klysubun, W.; Rupprechter, G.; Wittayakun, J. Catalytic Enhancement of Platinum Supported on Zeolite Beta for Toluene Hydrogenation by Addition of Palladium. *Journal of Industrial and Engineering Chemistry* **2009**, *15* (6), 819–823. https://doi.org/10.1016/j.jiec.2009.09.006.

(30) Baer, D. R. Guide to Making XPS Measurements on Nanoparticles. *Journal of Vacuum Science & Technology A: Vacuum, Surfaces, and Films* **2020**, *38* (3). https://doi.org/10.1116/1.5141419.

(31) Khan, S. R.; Sharma, B.; Chawla, P. A.; Bhatia, R. Inductively Coupled Plasma Optical Emission Spectrometry (ICP-OES): A Powerful Analytical Technique for Elemental Analysis. *Food Analytical Methods*. Springer March 1, **2022**, pp 666–688. https://doi.org/10.1007/s12161-021-02148-4.

(32) Singh, A.; Spiccia, L. Water Oxidation Catalysts Based on Abundant 1st Row Transition Metals. *Coordination Chemistry Reviews*. Elsevier B.V. **2013**, p 2607. https://doi.org/10.1016/j.ccr.2013.02.027.

(33) Liu, J.; Zhu, D.; Ling, T.; Vasileff, A.; Qiao, S. Z. S-NiFe2O4 Ultra-Small Nanoparticle Built Nanosheets for Efficient Water Splitting in Alkaline and Neutral PH. *Nano Energy* **2017**, *40*, 264–273. https://doi.org/10.1016/j.nanoen.2017.08.031.

(34) Maeda, K. Photocatalytic Water Splitting Using Semiconductor Particles: History and Recent Developments. *Journal of Photochemistry and Photobiology C: Photochemistry Reviews*. December 2011, pp 237–268. https://doi.org/10.1016/j.jphotochemrev.**2011**.07.001.

(35) Ghosh, S.; Hajra, P. Metal Oxide Catalysts for Photoelectrochemical Water Splitting. In *Metal Oxide-Based Nanostructured Electrocatalysts for Fuel Cells, Electrolyzers, and Metal-Air Batteries*; Elsevier, **2021**; pp 105–138. https://doi.org/10.1016/B978-0-12-818496-7.00005-9.

(36) Sen, R.; Das, S.; Nath, A.; Maharana, P.; Kar, P.; Verpoort, F.; Liang, P.; Roy, S. Electrocatalytic Water Oxidation: An Overview With an Example of Translation From Lab to Market. *Frontiers in Chemistry*. Frontiers Media S.A. May 11, 2022. https://doi.org/10.3389/fchem.**2022**.861604.

(37) Demir, E.; Akbayrak, S.; Önal, A. M.; Özkar, S. Nanoceria-Supported Ruthenium(0) Nanoparticles: Highly Active and Stable Catalysts for Hydrogen Evolution from Water. *ACS Appl Mater Interfaces* **2018**, *10* (7), 6299–6308. https://doi.org/10.1021/acsami.7b17469.

(38) Suen, N.-T.; Hung, S.-F.; Quan, Q.; Zhang, N.; Xu, Y.-J.; Chen, H. M. Electrocatalysis for the Oxygen Evolution Reaction: Recent Development and Future Perspectives. *Chem Soc Rev* **2017**, *46* (2), 337–365. https://doi.org/10.1039/C6CS00328A.

(39) Xu, J.; Wang, L.; Zhang, J.; Qian, J.; Liu, J.; Zhang, Z.; Zhang, H.; Liu, X. Fabrication of Porous Double-Urchin-like MgCo2O4hierarchical Architectures for High-Rate Supercapacitors. *J Alloys Compd* **2016**, *688*, 933–938. https://doi.org/10.1016/j.jallcom.2016.07.250.

(40) Manikandan, B.; Endo, T.; Kaneko, S.; Murali, K. R.; John, R. Properties of Sol Gel Synthesized ZnO Nanoparticles. *Journal of Materials Science: Materials in Electronics* **2018**, *29* (11), 9474–9485. https://doi.org/10.1007/s10854-018-8981-8.

(41) Kuo, C. H.; Mosa, I. M.; Poyraz, A. S.; Biswas, S.; El-Sawy, A. M.; Song, W.; Luo, Z.; Chen, S. Y.; Rusling, J. F.; He, J.; Suib, S. L. Robust Mesoporous Manganese Oxide Catalysts for Water Oxidation. *ACS Catal* **2015**, *5* (3), 1693–1699. https://doi.org/10.1021/cs501739e.

(42) Ilango, I.; Balakrishnan, R. M. Amino Acid Functionalized Metal Oxide Nanocomposite for the Removal of Fluoroquinolones. *J Clean Prod* **2023**, *429*. https://doi.org/10.1016/j.jclepro.**2023**.139071.

(43) Sikdar, D.; Roy, K.; Chandra Debnath, S. Green and Sustainable Biosynthesis of Iron Oxide Nanoparticle (ION) from Pomegranate Seed and the Development of Highly Reinforced ION Based Natural Rubber (NR) Nanocomposite in Presence of Epoxidized Natural Rubber (ENR) as Compatibilizer. *Current Research in Green and Sustainable Chemistry* **2022**, *5*. https://doi.org/10.1016/j.crgsc.2021.100256.

(44) Vanaja, A.; Ramaraju, G. V.; Srinivasa Rao, K. Structural and Optical Investigation of Al Doped ZnO Nanoparticles Synthesized by Sol-Gel Process. *Indian J Sci Technol* **2016**, *9* (12). https://doi.org/10.17485/ijst/2016/v9i12/87013.

(45) Zhang, G.; Li, Y.; Zhou, Y.; Yang, F. NiFe Layered-Double-Hydroxide-Derived NiO-NiFe 2 O 4 /Reduced Graphene Oxide Architectures for Enhanced Electrocatalysis of Alkaline Water Splitting. *ChemElectroChem* **2016**, *3* (11), 1927–1936. https://doi.org/10.1002/celc.201600301.

(46) Liu, Q.; Jin, J.; Zhang, J. NiCo 2 S 4 @graphene as a Bifunctional Electrocatalyst for Oxygen Reduction and Evolution Reactions. *ACS Appl Mater Interfaces* **2013**, *5* (11), 5002–5008. https://doi.org/10.1021/am4007897.

(47) Liu, G.; Gao, X.; Wang, K.; He, D.; Li, J. Uniformly Mesoporous NiO/NiFe2O4 Biphasic Nanorods as Efficient Oxygen Evolving Catalyst for Water Splitting. *Int J Hydrogen Energy* **2016**, *41* (40), 17976–17986. https://doi.org/10.1016/j.ijhydene.2016.07.268.

(48) Kang, B. K.; Woo, M. H.; Lee, J.; Song, Y. H.; Wang, Z.; Guo, Y.; Yamauchi, Y.; Kim, J. H.; Lim, B.; Yoon, D. H. Mesoporous Ni–Fe Oxide Multi-Composite Hollow Nanocages for Efficient Electrocatalytic Water Oxidation Reactions. *J Mater Chem A Mater* **2017**, *5* (9), 4320–4324. https://doi.org/10.1039/C6TA10094E.

(49) Lim, D.; Oh, E.; Lim, C.; Shim, S. E.; Baeck, S.-H. Bimetallic NiFe Alloys as Highly Efficient Electrocatalysts for the Oxygen Evolution Reaction. *Catal Today* **2020**, *352*, 27–33. https://doi.org/10.1016/j.cattod.2019.09.046.

(50) Hsieh, P. T.; Chen, Y. C.; Kao, K. S.; Wang, C. M. Luminescence Mechanism of ZnO Thin Film Investigated by XPS Measurement. *Appl Phys A Mater Sci Process* **2008**, *90* (2), 317–321. https://doi.org/10.1007/s00339-007-4275-3.

(51) Chen, M.; Wang, X.; Yu, Y. H.; Pei, Z. L.; Bai, X. D.; Sun, C.; Huang, R. F.; Wen, L. S. *X-Ray Photoelectron Spectroscopy and Auger Electron Spectroscopy Studies of Al-Doped ZnO Films*. www.elsevier.nlrlocaterapsusc.

(52) Xie, Z.; Zhang, C.; He, X.; Liang, Y.; Meng, D.; Wang, J.; Liang, P.; Zhang, Z. Iron and Nickel Mixed Oxides Derived From NiIIFeII-PBA for Oxygen Evolution Electrocatalysis. *Front Chem* **2019**, *7*. https://doi.org/10.3389/fchem.2019.00539.

(53) Mian Li, Y. X. X. L. X. B. Y. Z. C. H. and L. G. Facile Synthesis of Electrospun MFe2O4 (M = Co, Ni, Cu, Mn) Spinel Nanofibers with Excellent Electrocatalytic Properties for Oxygen Evolution and Hydrogen Peroxide Reduction.

(54) Simon, C.; Zakaria, M. B.; Kurz, H.; Tetzlaff, D.; Blösser, A.; Weiss, M.; Timm, J.; Weber, B.; Apfel, U. P.; Marschall, R. Magnetic NiFe2O4 Nanoparticles Prepared via Non-Aqueous Microwave-Assisted Synthesis for Application in Electrocatalytic Water Oxidation. *Chemistry - A European Journal* **2021**, *27* (68), 16990–17001. https://doi.org/10.1002/chem.202101716.

(55) Lim, D.; Kong, H.; Kim, N.; Lim, C.; Ahn, W. S.; Baeck, S. H. Oxygen-Deficient NiFe2O4 Spinel Nanoparticles as an Enhanced Electrocatalyst for the Oxygen Evolution Reaction. *ChemNanoMat* **2019**, *5* (10), 1296–1302. https://doi.org/10.1002/cnma.201900231.

(56) Chen, Q.; Wang, R.; Lu, F.; Kuang, X.; Tong, Y.; Lu, X. Boosting the Oxygen Evolution Reaction Activity of NiFe2O4 Nanosheets by Phosphate Ion Functionalization. *ACS Omega* **2019**, *4* (2), 3493–3499. https://doi.org/10.1021/acsomega.8b03081.

(57) Zhang, R.; Wei, H.; Si, W.; Ou, G.; Zhao, C.; Song, M.; Zhang, C.; Wu, H. Enhanced Electrocatalytic Activity for Water Splitting on NiO/Ni/Carbon Fiber Paper. *Materials* **2017**, *10* (1). https://doi.org/10.3390/ma10010015.

(58) Khan, N. A.; Rashid, N.; Ahmad, I.; Zahidullah; Zairov, R.; Rehman, H. ur; Nazar, M. F.; Jabeen, U. An Efficient Fe2O3/FeS Heterostructures Water Oxidation Catalyst. *Int J Hydrogen Energy* **2022**, *47* (53), 22340–22347. https://doi.org/10.1016/j.ijhydene.2022.05.045.

(59) Liu, G.; Gao, X.; Wang, K.; He, D.; Li, J. Uniformly Mesoporous NiO/NiFe2O4 Biphasic Nanorods as Efficient Oxygen Evolving Catalyst for Water Splitting. *Int J Hydrogen Energy* **2016**, *41* (40), 17976–17986. https://doi.org/10.1016/j.ijhydene.2016.07.268.

APPENDICES

A. Synthesis of RuO_2 and characterization of RuO_2 nanoparticle

0.01 mol of $RuCl_3 \cdot 3H_2O$ was dissolve in 100 mL of water, the mixture was stirred for 10 min at 100 °C. Next, 1 mL of 1.0 M KOH solution was added to the solution, and it was stirred for 45 minutes at 100 °C. After that, the mixture was filtered and centrifuged for10 min. Precipitation washed several times with water. It was dried at 80°C for 5 hours. The dried product was calcined in air at 300 °C for 3 hours to produce RuO_2.

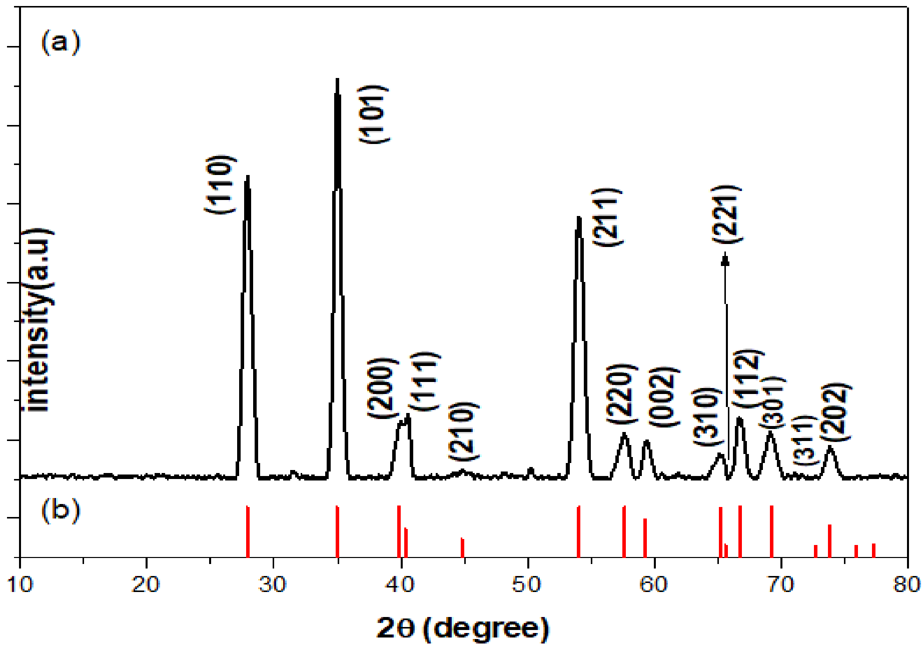

Figure A. 1 The XRD pattern of RuO_2 nanoparticles, (a) the XRD pattern of RuO_2 synthesized in this study and (b) standard XRD pattern of RuO_2 (JCPDS File No. 65-2824).

The X-ray diffraction peaks of RuO_2 are shown in Fig. A.1. The peaks located at 2ϴ values of 27.94 (110), 35.00 (101), 39.90 (200), 40.56(111), 44.86 (210), 54.06 (211), 57.57 (220), 59.39 (002), 65.17 (310), 65.60 (221), 66.60 (112), 69.24 (301),72.61 (311) and 73.75 (202).